UNIVERSITY OF CALIFORNIA
SANTA CRUZ

MAGNETISM AND GRAVITY AS CLUES TO THE THERMAL HISTORIES OF THE MOON AND MARS

A dissertation submitted in partial satisfaction
of the requirements for the degree of

DOCTOR OF PHILOSOPHY

in

EARTH SCIENCES

By

Rachel E. Maxwell

December 2022

The Dissertation of Rachel E. Maxwell is
approved:

_____
Professor Ian Garrick-Bethell, chair

_____
Professor Francis Nimmo

_____
Professor Robert Coe

_____
Dr. Mark Wieczorek

_____
Peter Biehl
Vice Provost and Dean of Graduate Studies

Copyright © by

Rachel E. Maxwell

2022

Table of Contents

List of Figures

List of Tables

Abstract

Magnetism and Gravity as Clues to the Thermal Histories of the Moon and Mars

Rachel E. Maxwell

This dissertation thesis is a combination of three projects on magnetism and gravity studies of the Moon and a magnetism study of Mars, each with a heavy focus on uncertainty estimation. The goal of each chapter is to elucidate some portion of the thermal history of the Moon and Mars. Analysis of crustal magnetic fields can explain past dynamo behavior, which is tied to the amount of heat within a planet and how long it retains that heat. Elastic thickness, determined from correlations between gravity and topography, indicates the heat flux at the time of load emplacement and we can use the elastic thickness of a region to determine its formation age. The results from this thesis place constraints on the ancient dynamo behavior of the Moon and Mars (magnetism studies) and on the formation ages of portions of the farside of the Moon (gravity studies).

Chapter 1 focuses on lunar crustal magnetic anomalies. The Moon no longer has an active global magnetic field, but evidence of an ancient field can be found in portions of the crust, which have been magnetized in the presence of intense fields thought to be generated by an extant dynamo. Quantifying the magnetization directions of these anomalies elucidates the behavior of the paleo-magnetic field by determining the magnetic paleopole (i.e., the orientation of the dipolar axis). Previously, distinguishing between paleopole locations was impossible because of

their large uncertainties. Without distinguishing between paleopole locations, determining the history of the lunar dynamo is impossible.

I propose an alternative method of estimating uncertainty using a Monte Carlo method to add synthetic noise to the best-fit modeled fields, which allows us to determine how easily perturbed the magnetization direction is in the presence of noise (i.e., uncorrelated anomalies). The new method more accurately describes the uncertainty of the inversion method and allows for better discernment of paleopole locations. I determined that the dipolar axis of the lunar dynamo must have been misaligned with the spin-axis at some point in lunar history, or that there were significant multipolar components to the magnetic field.

Chapter 2 focuses on gravity and topography studies of the Moon. I use admittance analysis to determine the lunar elastic thickness and how it varies across the Moon. Elastic thickness allows us to determine the heat flux at the time of load emplacement, which in turn elucidates the thermal history of the Moon. Regions of low elastic thickness indicate high heating at the time of loading, and we can infer these locations formed earlier in lunar history than areas with higher elastic thicknesses. However, as in Chapter 1, variations in elastic thickness are meaningless without a clear estimate of uncertainty to distinguish between values.

In this chapter, I describe how to determine elastic thickness using the spectral domain and the Markov chain Monte Carlo (MCMC) technique. Careful consideration is given to where these techniques are valid, including an analysis of the uncertainties from the MCMC technique using synthetic testing. I find that there

are several locations on the Moon with low elastic thickness, implying these regions formed very early (<200 Myr) after the lunar magma ocean solidification. I also find one region with higher elastic thickness, which may be recording loading events as late as 3.5 Ga.

Chapter 3 focuses on martian crustal magnetic anomalies. Like the Moon, Mars no longer has a global magnetic field, but there is evidence of a dynamo-generated field in the presence of widespread crustal magnetism. The issue of martian paleopole locations has plagued the magnetism community for two decades, many of the inferred paleopole locations do not correlate with each other, and several paleopole locations do not correlate with inferred paleo-spin axes calculated by other geophysical means. Additionally, there has not been a thorough paleopole analysis of crustal magnetic anomalies since the release of new magnetometer data from the NASA Mars Atmosphere and Volatile Evolution (MAVEN) mission.

I use the methods described in Chapter 1 to determine the magnetic paleopole locations and uncertainties of ten martian crustal magnetic anomalies. I then use the Maximum Angular Deviation (MAD) technique to quantify the degree of clustering of our paleopole uncertainty ellipses and find significant clustering around a low latitude (45°N), which corresponds with a paleo-spin axis found through paleo-shoreline analysis (Perron et al., 2007). I show that the wide spread of other paleopole locations cannot be explained by a multipolar field or a hemispherical dynamo.

For the little girl who wanted to go to the Moon, and for all those who have helped her along the way.

Acknowledgments

I could write an entire thesis on acknowledgements, but I'll keep it as brief as I can.

To Ian: I still have no idea what made my application stand out to you 7+ years ago, but I will be forever thankful that you chose me to be your graduate student. I applied to schools not really knowing what I wanted to do, but hearing you talk about lunar swirls flicked a switch that I will never turn off. You have been a wonderful advisor and I don't have enough room in this document to do you justice. Thank you for your patience as I fumbled through grad school. Thank you for your never-ending encouragements. Thank you for the wisdom you have passed on during our meetings. Thank you for being such a thoughtful scientist. I am truly honored to have been your graduate student!

To Francis: Thank you for finding the time to help *yet another* graduate student. I am grateful for all the lessons you have taught me. The lesson that sticks out the most is actually one I learned during my visit weekend at UCSC. During our meeting, you brought out some journal that had Europa on the cover and let me read through a few sections. I thought I'd feel rushed – come up with a question quick so he thinks you're smart! But I didn't feel rushed. I don't know how you do it, but you're very good at making students feel like they have the space to move at their own pace. As someone who constantly fidgets with needing to go, go, go, I sincerely thank you for providing that space.

To Rob and Mark: Thank you both for sticking it out on my committee! Having scientists who are not paying you salary take an interest in your work is so crucial to

any budding young scientist's journey, and I am beyond thankful the two of you took on this role.

To Mom, Dad, and Shane: Thank you for always encouraging my dreams, even when you don't understand them! You have seen me grow as a person and as a scientist, and it's always nice to be reminded of just how far I have come. It gives hope for the road ahead. I love you.

To my Friends: I love each and every one of you. Thank you for your support, your commiseration, and your friendship!

To Jack: It's a special kind of funny that I got to live with you, in the city where "it" all started for me (Huntsville, Alabama – thank you, Space Camp) as I finish up my degree. Thank you for always being there, even when you can't be there in person. I am so lucky to have you, and not just because you cook for me ~~when I'm stressed~~ all the time. Thank you for doing the grad school/graduation thing first so I have an example to follow. Thank you for loving Sarek with me. I love you 5ever.

The text of this dissertation includes reprint of the following previously published and submitted material:

Chapter 1:
Maxwell, R.E., Garrick-Bethell, I., 2020. Evidence for an Ancient Near-Equatorial Lunar Dipole From Higher Precision Inversions of Crustal Magnetization. Journal of Geophysical Research: Planets 125, e2020JE006567. https://doi.org/10.1029/2020JE006567

Chapter 2:
Maxwell, R.E., Nimmo, F., 2022. Variations in Lunar Elastic Thickness from Admittance Spectral Analysis. Icarus, *submitted*.

Chapter 1: Evidence for an ancient near-equatorial lunar dipole from higher precision inversions of crustal magnetization

Abstract

Studies of lunar paleopoles have been used to make a variety of inferences about past episodes of true polar wander and the orientation of the ancient dynamo field. However, the large and variable uncertainties commonly reported for such studies make robust conclusions difficult. To make further progress, we used synthetic magnetic anomalies to assess a common method to estimate magnetization direction uncertainty. We find that with this method, magnetic anomalies with higher inclinations have systematically higher uncertainties than lower inclination anomalies. We call this effect inclination bias. A similar effect is found for declination, but it is weaker. We also find this method often produces overly conservative uncertainty estimates. To avoid these effects, we use Monte Carlo methods to determine magnetization direction uncertainty. We apply our methods to five lunar magnetic anomalies with a wide range of reported magnetization directions and paleopole locations. We find that inclination bias partly explains the previously reported anomalously high and low direction uncertainties for two of these anomalies: Reiner Gamma and Airy. Our more robust uncertainties allow us to conclude that four paleopoles are located near the equator. Such low latitudes cannot be explained by true polar wander inferred from other independent datasets, such as the lunar gravity field and

the polar hydrogen distribution. This in turn implies that the dynamo axis was once offset from the spin axis.

1 Introduction

Rocks that cool in the presence of a planetary magnetic field can produce crustal magnetic anomalies observable from ships, aircraft, and spacecraft. Such anomalies are seen on Earth, the Moon, Mars, and Mercury, and may one day be detected on other bodies. Similarly, very high-resolution magnetic microscopy can produce two-dimensional maps of magnetization in thin sections of rocks (Glenn et al., 2017; Lima & Weiss, 2016). Magnetized materials can be analyzed for their magnetization direction, which can provide constraints on numerous geophysical processes. For example, on the Moon, the magnetization direction of crustal anomalies can control their interaction with the solar wind plasma (Deca et al., 2020; Hemingway & Garrick-Bethell, 2012; Poppe et al., 2016). The magnetization direction also places constraints on the local orientation of the paleomagnetic field at the time of anomaly formation. If one assumes a dipolar spin-aligned paleomagnetic field, the paleopole location (i.e., ancient spin axis pole) can be inferred (Irving, 1964).

Numerous studies of lunar magnetic paleopoles have been performed, starting with work by Hood (1981)and Runcorn (1983). Takahashi et al. (2014) found at least two clusters of paleopoles and interpreted them to represent true polar wander. Arkani-Hamed and Boutin (2014) also found clustered paleopoles and interpreted some of them to represent reversals. Oliveira and Wieczorek (2017) found paleopole locations similar to,

or within the range of uncertainty of, paleopoles found by Takahashi et al. (2014) and Arkani-Hamed and Boutin (2014). They interpreted these paleopoles to represent motion of the dynamo dipole axis. Additional work has found more complicated patterns of paleopole locations. For example, crustal magnetic anomalies in and around the South Pole-Aitken Basin are widely distributed (Nayak et al., 2017), and several anomalies within the Crisium Basin have different paleopole locations, despite sharing a common geologic origin (Baek et al., 2017, 2019).

Independent estimates of lunar true polar wander from the Moon's gravity field and polar hydrogen distribution limit the largest principal moment of inertia deviation to <36° of colatitude (Garrick-Bethell et al., 2014; Keane & Matsuyama, 2014; Siegler et al., 2016). This deviation is substantially less the 90° required to explain a magnetic paleopole at the equator. Therefore, assuming the gravity and hydrogen studies provide reasonable constraints, any verified near-equatorial magnetic paleopoles would suggest that the Moon's dynamo dipole axis was offset from the spin axis. This configuration could have implications for the dynamo mechanism (Takahashi et al., 2009), as well as implications for the formation of polar volatile deposits (Garrick-Bethell et al., 2019). A major goal of this study is to reassess, in the context of new uncertainty estimation methods, the locations of previously reported near-equatorial paleopoles.

One major concern of magnetic paleopole analyses is the uncertainty associated with the best-fit magnetization direction. Large uncertainties (near 90° in some cases, e.g., Oliveira et al., 2019; Oliveira & Wieczorek, 2017; Thomas et al., 2018) make it difficult to determine if paleopoles found distant from the present pole truly represent

deviation of the dipole axis from the spin axis. Unfortunately, there currently exists no consistent method of describing direction uncertainties across inversion methods (Maxwell et al., 2017).

A widely used technique for determining the magnetization direction of crustal magnetic anomalies was developed by Parker (1991), herein referred to as Parker's Method. This method calculates the best-fit strengths of a two-dimensional grid of source dipoles at the surface for an assumed magnetization direction (details in Section 2, Methods). Parker's Method was previously used to study the magnetization of Earth seamounts (Parker, 1991), and has more recently been used to study crustal magnetic anomalies on the Moon (Lee et al., 2019; Oliveira & Wieczorek, 2017; Oliveira et al., 2017), Mars (Morschhauser et al., 2014; Thomas et al., 2018), and Mercury (Oliveira et al., 2019). To determine uncertainty in the magnetization direction, Parker (1991) suggests choosing an acceptable root mean squared (RMS, in units of magnetic field) difference between the data set and best-modeled field for an assumed direction, called the “maximum misfit” (Figure 1.1). All directions with errors less than this maximum misfit are considered acceptable, and thus used to estimate direction uncertainty (described in Section 2, Methods).

How to choose the maximum misfit is an open question. Several authors have chosen a misfit equal to the RMS of the background field, using the assumption that the background field is statistically similar to the unmodeled magnetic field, that is the portion of the magnetization that is not a part of the unidirectionally magnetized anomaly (Oliveira & Wieczorek, 2017; Oliveira et al., 2019; Lee et al., 2019; Thomas et al., 2018).

The instrument noise from magnetometers on Lunar Prospector and Kaguya is less than 0.1 nT (Lin et al., 1998; Tsunakawa et al., 2010). This value is substantially smaller than the typical background crustal field strength, allowing authors to generally ignore it as major source of uncertainty (Oliveira & Wieczorek, 2017).

Using the background crustal field as the maximum acceptable misfit (Figure 1.1) poses challenges in two situations, as described by Oliveira and Wieczorek (2017). The first is when the anomaly's magnetic field is low compared to the background field, herein referred to as low signal-to-background ratio (SBR). In this case, the RMS error of the best-fit solution may be much lower than the RMS background field, possibly yielding an unrealistically high uncertainty. Indeed, all of the studies cited above show multiple instances of very large direction uncertainties, sometimes encompassing an entire hemisphere. The second challenge is when the anomaly's magnetic field is large compared to the surrounding field (high SBR). In this case, the
RMS error of the best-fit solution might be larger than the RMS background field, implying no other magnetization directions are acceptable. In other words, the uncertainty of the magnetization direction would be unrealistically zero. An example of this latter case was found for the Moon's Reiner Gamma anomaly in Oliveira and Wieczorek (2017).

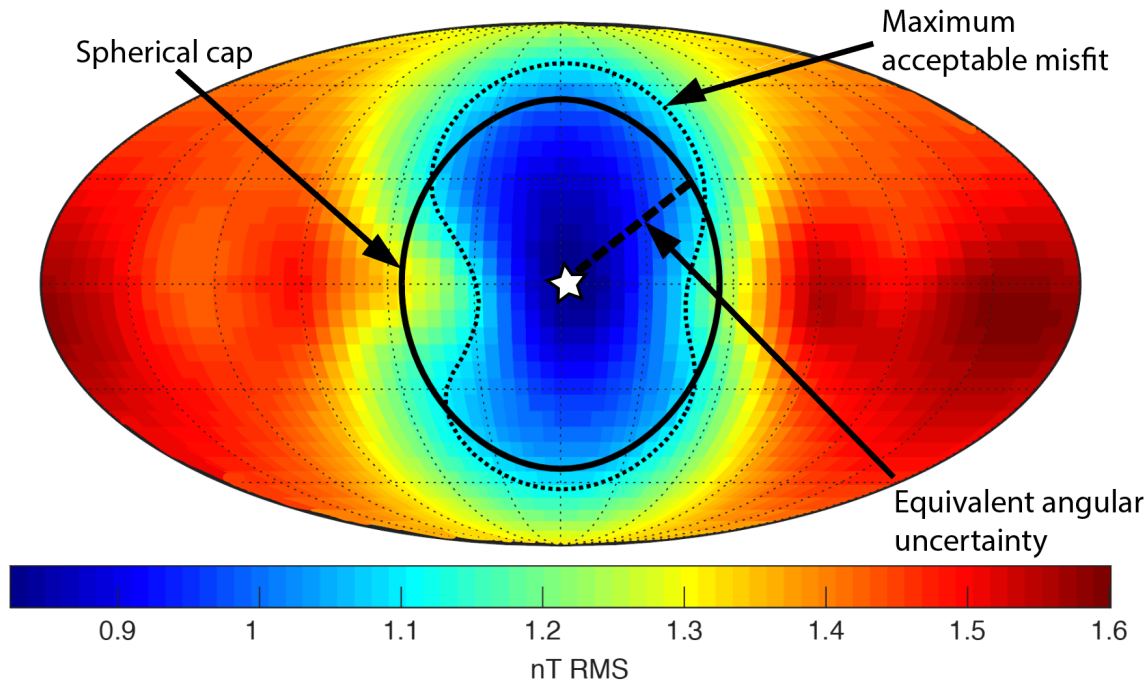

Figure 1.1: In a map of all possible magnetization directions for a magnetic anomaly inversion, the maximum acceptable misfit is a contour of root mean squared error values. The equivalent angular uncertainty (dashed line) is defined here as the radius of a spherical cap (solid line) with an area equal to the area within the contour defined by a maximum acceptable misfit (dotted line). Also shown is the best-fit location (white star). All maps of magnetization direction errors in this study are Mollweide projection with positive declinations increasing to the right and positive inclinations increasing downward. The center of the figure has an inclination of 0° and declination of 0°.

We have discovered an additional issue with estimating direction uncertainties using a maximum RMS error to define uncertainty. There is consistently a larger direction uncertainty for highly inclined magnetization directions than for horizontal magnetization directions. We call this effect “inclination bias.” This bias is also found in a simple dipole-fitting routine, indicating this effect is not restricted to just Parker's Method. It also occurs regardless of what misfit value is used, for example, a maximum acceptable misfit that is equal to the background crustal field (Parker, 1991). Inclination bias can affect analyses of paleopoles if uncertainties are so large as to make the result

unreliable. For example, Oliveira and Wieczorek (2017) analyzed the Airy magnetic anomaly and found a high inclination with a high magnetization direction uncertainty, such that they could not include the anomaly in their paleopole analysis. If anomalies like Airy cannot be used reliably in paleopole evolution analyses, it is possible that this will create a sampling bias where analyses of high-inclination anomalies are omitted and result in incorrect inferences about true polar wander or the dynamo orientation.

We propose a new method of uncertainty estimation that permits including results that were previously considered unreliable. This method involves a Monte Carlo approach, which has been used in studies of lunar crustal magnetism before (Baek et al., 2017, 2019; Nayak et al., 2017), but never with Parker's Method. We do not necessarily expect the inverted paleopole locations to change greatly, but rather we intend to make estimates of their locations more robust, and therefore usable in testing hypotheses about the lunar dynamo.

The objectives of this study are: (1) reassess the evidence for magnetic paleopoles near the present-day equator, (2) show that magnetization direction uncertainty is biased as a function of inclination, and usually unnecessarily conservative, when using a maximum acceptable misfit value to estimate uncertainty (Figure 1.1), (3) quantify how the strength of the background field (i.e., changes in SBR) affects the range of acceptable magnetization directions, and (4) suggest a new method of estimating uncertainties with Monte Carlo methods. To achieve these objectives, we first study isolated synthetic anomalies of several shapes. We then apply Parker's Method to invert for their magnetization direction and determine their uncertainty using a maximum misfit method.

We also add smaller, random synthetic magnetization sources to our analysis, to quantify how maximum misfit is affected by SBR. Finally, we apply Parker's Method and our Monte Carlo method to five lunar magnetic anomalies, whose geologic origins suggest unidirectional magnetization, in order to achieve a higher precision estimate of their paleopole locations.

2 Methods

2.1 Synthetic Anomalies

We begin by generating six different isolated synthetic patterns of magnetization to demonstrate the problems of using a maximum acceptable misfit to quantify uncertainty: A dipole, a rectangle, a square, a triangle, a circle, and a random assortment of 14 dipoles (example fields from all anomalies are shown in Appendix Figure A1). The synthetic shapes are comprised of multiple dipoles of constant magnetization strength on a regular 0.25 ° x 0.25° grid and the magnetic field is calculated at each location on a 0.25 ° x 0.25° grid at 20 km altitude above the source (see Table 1.1 for details). The total magnetic moment is fixed for all shapes, though the number of dipoles used to create each shape varies. The choice of altitude is arbitrary in this case because the field is known perfectly (noise-free) and all inversions without noise perfectly recover the magnetization direction. However, we remark that in the case of real anomalies, varying the altitude of the measurements may vary the SBR, since the background and signal source bodies may each have different source depths.

Synthetic shapes with additional random background fields are also made to test the effect of scattered nonunidirectionally magnetized background anomalies, that is changes in SBR, on inclination bias. These background anomalies are dipoles on a grid, the size of the synthetic data set with 0.25 ° x 0.25° resolution and the field is measured at the same altitude as the synthetic anomaly. These anomalies are created with a uniform random distribution of magnetization strength and direction per dipole. The maximum magnetization strength increases to meet the SBR value we wish to model. SBR values are calculated by taking the maximum value of the total field of the anomaly divided by the RMS of the total field of the synthetic background field (prior to adding it to the anomaly). The synthetic nonunidirectional background field is then added to the synthetic anomaly field (Appendix Figure A2). Different values of SBR for a given anomaly shape are created using the same background dipoles (i.e., preserving their location and magnetization direction), though the strength of each dipole is chosen randomly each time a data set with a new SBR value is generated. In addition, to ensure that our conclusions were not affected by the location and magnetization direction of the background dipoles, we repeat our entire analysis with a set of dipoles with different locations and orientations (Appendix Figure A3).

Anomaly	**Dimensions**	**Number of Dipoles**	**Moment per dipole (Am^2)**	**Maximum Total Field Strength for 0° inclination (nT)**
Dipole	Single point	1	1×10^{13}	118.1
Rectangle	0.5° x 2°	18	5.56×10^{11}	54.5
Square	2° x 2°	81	1.23×10^{11}	18.2
Circle	2° radius	61	1.64×10^{11}	22.9

Triangle	$H = 2°$, $B = 2°$	49	2.04 x 10^{11}	26.0
Random	Randomly placed	14	7.14 x10^{11}	51.4

Table 1.1: Parameters used to create each of the synthetic datasets (see also Appendix Figure A1). Total moment for each anomaly is 1 x 10^{13} Am^2 and the burial depth is 0 m. The dipole and rectangle anomalies are discussed in detail in the main text. For the Triangle case, H = height of the triangle and B = base of the triangle. Dipoles are placed on a 0.25° x 0.25° resolution grid within the dimensions listed, centered at 0° N, 0° E. Here, dimensions of 1° ≈ 30 km of distance.

2.2 Parker's Method

Parker's Method places dipoles on a regular grid, within a specified area on a surface above the source body, to obtain the best-fitting magnetization distribution for a magnetization direction tested. It makes no assumption about the geometry of the magnetic source body but does follow the unidirectional assumption that all source material has the same magnetization direction, while allowing for a variation magnetization strength across an anomaly. Formally, this method models magnetization within some volume V as a unidirectional magnetic field whose magnetization strength m is an arbitrary function of position within the body, modeled on the surface of V. The magnetization is written as

$$\boldsymbol{M}(\boldsymbol{s}) = \hat{\boldsymbol{m}}\, m(\boldsymbol{s}), m(\boldsymbol{s}) \geq 0.$$

where $\hat{\boldsymbol{m}}$ is the magnetization direction and $\boldsymbol{s}$ is the location. Observations taken outside of V are approximated as the field component along $\hat{\boldsymbol{B}}_0$, the direction of the main magnetic field in the vicinity. In this work, we follow the precedent set by (Oliveira and Wieczorek, 2017) and use radial component of the magnetic field. We have confirmed

the tests done by Oliveira and Wieczorek (2017) showing that the field component used in Parker's Method does not substantially affect the results.

From Parker et al. (1987), N_o observations d_j made at positions $\boldsymbol{r}_j$ can be calculated as the sum of contributions from N_d dipoles located at $\boldsymbol{s}_i$.

$$d_j = \sum_{i=1}^{N_d} g_j(\boldsymbol{s}_i) m(\boldsymbol{s}_i)\,, j = 1, \ldots, N_o$$

where the contribution from a single dipole at location i is given as

$$g_j(\boldsymbol{s}) = \frac{\mu_0}{4\pi}\left[\frac{3\widehat{\boldsymbol{m}}\cdot(\boldsymbol{r_j}-\boldsymbol{s})\widehat{\boldsymbol{B}}_0\cdot(\boldsymbol{r_j}-\boldsymbol{s})}{|\boldsymbol{r_j}-\boldsymbol{s}|^5} - \frac{\widehat{\boldsymbol{m}}\cdot\widehat{\boldsymbol{B}}_0}{|\boldsymbol{r_j}-\boldsymbol{s}|^3}\right]$$

From this, we can use the matrix G, which depends on the dipole locations i = 1, …, N_d and j = 1, …, N_o, to find the magnetization strength of the source dipoles by solving the non-negative least squares technique as developed by (Lawson and Hanson, 1974).

$$\min_{m\geq 0}\|\boldsymbol{d} - G\boldsymbol{m}\|^2$$

Note that the user must choose a test-dipole spacing resolution and their spatial coverage. They may have to adjust these values based on initial results. Following Oliveira and Wieczorek (2017), we use circular magnetic field datasets (Appendix Figure A4), with the radius of the data circle set larger than the circle of permissible source dipoles to avoid unwanted edge effects. We then test magnetization directions over a unit sphere equally spaced by ~4° for every iteration of Parker's Method. When synthetic datasets are used, we place test dipoles exactly where the synthetic dipoles are located.

Hence, the best-fit solution will have exactly zero RMS error at the synthetic anomaly's true magnetization direction, in the absence of added random background fields.

2.3 Single Dipole Fit

To compare Parker's Method to the simplest possible inversion method at the simplest possible anomaly, we use a single dipole fit method to recover the magnetization direction of a synthetic, isolated single dipole. No synthetic nonunidirectional background field is added. We test magnetization directions over a unit sphere equally spaced by ~4°. RMS values of the difference between the data set and model are then calculated for each direction tested, for each magnetization component. We assume perfect knowledge of the dipole magnetization strength, location, and depth and therefore do not test these parameters. Hence, the uncertainty in magnetization direction obtained from this idealized analysis is a best-case scenario.

2.4 Calculating Uncertainties for Synthetic Anomalies

Arbitrary maximum acceptable misfits (e.g., RMS error 1, 2, etc., nT) and a 1-σ maximum acceptable misfit are used to estimate uncertainties for the synthetic tests without added background fields. Here 1-σ is the standard deviation of the errors for all magnetization directions tested on a unit sphere. When a synthetic nonunidirectional background field is added, or real anomalies are analyzed, the arbitrary maximum misfit chosen is the RMS background field. Whatever the misfit used to determine the direction uncertainty, we calculate the fractional area within the unit sphere of directions that is

less than the maximum acceptable misfit: the “acceptable area.” Next, we equate this area to the area of a spherical cap, and the angular radius of this cap is taken to be the “equivalent angular uncertainty” (Figure 1.1). Converting the range of acceptable magnetization directions into to single angular radius (the equivalent angular uncertainty) in this manner simplifies the interpretation of the uncertainty and facilitates comparisons across different model parameters.

2.5 Monte Carlo Approach to Estimating Magnetization Direction Uncertainties

Because Parker's Method adequately estimates the magnetization direction in the presence of modest background random fields (eventually demonstrated in Figure 1.8b), our suggested approach to estimate uncertainty is to:

1. Compute a best-fit model of an anomaly (e.g., from spacecraft data). This model is derived from observations that are contaminated by background crustal fields. This contamination produces a “perturbation” of the best-fit result away from the true, unknowable direction.
2. Add synthetic nonunidirectional random background fields to the model in Step 1 to produce a SBR similar to that of the real-world anomaly. This step adds background fields to a model that is already contaminated by background fields (step 1). Hence, our addition of background fields is a second perturbation of the system away from the true direction. However, if the background fields are sufficiently low (high SBR), on average, this second perturbation will be of the same magnitude as the first (see cartoon of this assumption in Figure S6).

3. Perform a Parker's Method inversion for the background-field-added data set from step 2.
4. Repeat steps 2 and 3 with a new background-field. Each repetition of this step represents one iteration of the Monte Carlo approach. In other words, each repetition is a new random perturbation of the solution away from the step 1 model. On average, we expect these perturbations to have a scatter, quantified as angular standard deviation, that comes close to encompassing the actual true direction, based on the reasoning in step 2.
5. Compute the angular distance between the best-fit model (step 1, "best-fit" direction) and each best-fit direction of the synthetic cases generated in step 4 ("perturbed directions"). We take each of these angles to be θ_Δ. The angular standard deviation, *s*, of all of the θ_Δ angles is be taken as a measure of the uncertainty (calculated using Fisher statistics).

Using this method in practice at lunar magnetic anomalies, we first obtain a best-fit model from the Tsunakawa et al. (2015) lunar magnetic field model (surface vector mapping [SVM] method). Other magnetic field maps have been published (e.g., Purucker and Nicholas 2010; Ravat et al., 2020), but we expect the SBR values for each of these datasets to be similar, such that our uncertainty estimates will also be similar. We then create synthetic random background-field-added datasets (such that the SBR is similar to the real- world SBR, within ±1 SBR units) in the manner described in Section 2.1. In practice, one could also add other random background fields that represent instrument noise, though we ignore these herein as they are less than ~0.1 nT (above). We perform

20 background-field-added inversions for each anomaly (step 4) and calculate the anomaly's direction uncertainty via the precision parameter k and angular standard deviations (Bulter, 1992; Nayak et al., 2017, Appendix Text A1). We assume that the 20 best-fit directions are Fisher distributed. The original best-fit value (step 1) is reported as the final direction, with uncertainty s, the angular standard deviation (Table 1.2).

2.6 Lunar Magnetic Anomalies and Selection Criteria

A crustal magnetic anomaly must be isolated from other anomalies and unidirectionally magnetized (defined as all magnetization in the same direction, but not necessarily with uniform intensity) to ensure the best-fit solution is well constrained. Thomas et al. (2018) found that anomalies should be a distance of at least twice their radius away from other anomalies to avoid unrelated sources that could increase the maximum acceptable misfit value. Gerhards (2016) showed that magnetizations cannot be determined uniquely when the magnetization is nonzero outside a finite region (i.e., the anomaly must be isolated). Vervelidou et al. (2017) reached similar conclusions and discussed the problems with nonunidirectionally magnetized sources.

We analyze five lunar magnetic anomalies (Appendix Figure A4) that have been previously analyzed (e.g., Oliveira & Wieczorek, 2017). All anomalies are isolated, such that they likely formed in a discrete, relatively short-lived event and therefore acquired unidirectional magnetization. Three of these anomalies (Reiner Gamma, Airy, and Abel) are associated with lunar swirls, which likely indicates a shallow source (Hemingway & Tikoo 2018). In particular, the magnetic source material for Reiner Gamma has been

proposed to be a melt sheet or floor deposits from an oblique impact crater (Garrick-Bethell & Kelley, 2019). A shallow source would cool quickly and therefore be more likely to record a unidirectional field.

The other anomalies we test, Hartwig and Sylvester, do not exhibit swirls, but could still be reasonably assumed to have formed in a discrete, short-lived event and therefore record a unidirectional field. Specifically, both anomalies are located in the lunar highlands, where a major hypothesis for their origin is the deposition of impact ejecta (Hood et al., 2001; Wakita et al., 2020; Wieczorek et al., 2012).

Four of these anomalies may have near-equatorial paleopoles: Abel, Airy, Hartwig, and Sylvester (Table 1.2), based on prior work. A fifth anomaly with a polar paleopole, Reiner Gamma, was also included, for comparison. All five anomalies have a diverse range of real-world SBR values and inclinations.

To test the robustness of our results (and to ensure the magnitude of the calculated background fields are not significantly interfering with our inversions) we repeat analyses for each anomaly with a different sized data extent. We use the radial distances from the center of the anomalies chosen by Oliveira and Wieczorek (2017) as well as smaller radii (except Sylvester for which we chose a larger radius to capture all of the anomaly). The data in the 30 km altitude Tsunakawa SVM map have a spacing 0.5° and we choose a spacing of 0.4° for our inversions, following Oliveira and Wieczorek (2017).

Table 1.2: Summary of crustal magnetic anomalies analyzed. Location of the anomaly in latitude (λ_s) and longitude (φ_s), radii of observations (r_o) and test dipoles (r_d), the SBR value associated with each observational extent, the inclination (Inc) and declination (Dec) resulting from Parker's Method, paleopole latitude (λ_p) and longitude (φ_p), the precision parameter (*k),* and angular standard deviation (*s*) from the 20 Monte Carlo simulations to estimate uncertainty, and the paleopole ellipse semi-axes, *dm* and *dp,* derived from *s*. All are in units of degrees, except for SBR and *k* which are unitless. Note that all center latitudes and longitudes are the same except for Abel which has a different central latitude.

Anomaly	Abel		Airy		Hartwig		Reiner		Sylvester	
λ_s (°N)	-31.0	-32.5	-18.2	-18.2	-9.0	-9.0	7.6	7.6	80.0	80.0
φ_s (°E)	87.5	87.5	3.1	3.1	280.0	280.0	-57.3	-57.3	288.0	288.0
r_o (°)	7	6	5	4	9	6	8	6	6	5
r_d (°)	6	5	4	3	8	5	7	5	5	4
SBR	9.7	6.2	7.7	8.5	11.0	6.0	22.9	14.3	5.2	4.0
Inc (°)	-34	-42	50	54	-42	-26	0	-3	0	4.
Dec (°)	-163	-144	-126	-128	-51	-57	-5	-7	9	2
λ_p (°N)	-38.2	-23.9	-39.6	-41.1	39.1	34.3	82.0	79.0	10.9	13.0
φ_p (°E)	288.8	303.5	-61.1	-55.8	166.3	180.3	157.1	161.5	98.8	105.6
k	212.5	85.4	29.5	22.9	195.7	77.4	687.4	219.5	109.1	42.8
s (°)	5.6	8.8	15.0	17.1	5.8	9.2	3.1	5.5	7.8	12.5
dm (°)	6.3	10.7	20.1	24.1	7.1	9.9	3.1	5.5	7.8	12.5
dp (°)	3.6	6.6	13.5	17.0	4.3	5.3	1.5	2.7	3.9	6.3

To calculate the paleopole locations from our magnetization directions, we use the equations from Irving (1964) (see Appendix Text A1), and also the description in Takahashi et al. [2014]). We derive the paleopole error ellipse from the angular standard deviation s (above), which is characterized by the semi-axes dp and dm, such that dp is along the great circle that connects the anomaly location with the paleopole location and dm is perpendicular to that great circle. We note that confidence intervals cannot be yet be calculated with present methods, as a confidence interval is based on the number of samples. Here, we do not have a variety of samples but rather a group of similar non-independent datasets with added random background fields.

3. Results

3.1. Inclination Bias in Both Parker's Method and the Single Dipole Fit Method Applied to Single-Dipole Sources

We find that the equivalent angular uncertainty (Figure 1.1) of a single dipole is a function of inclination. For both the single dipole fit method (Figure 1.2) and Parker's Method (Figure 1.3), a dipole that is north-pointing (0° inclination) has lower uncertainties than a dipole that is radially pointing (90° inclination, Figure 1.4), when using a maximum acceptable misfit value to compute the uncertainty. The effect is present in all cases of chosen misfit value (RMS error of 1, 2, 3, 5, and 7 nT). Histograms depicting the frequency of RMS error values help demonstrate the origin of the inclination bias (Figures 1.2 and 1.3). More acceptable magnetization directions are found for the same maximum acceptable misfit for higher inclinations versus lower

inclinations, for both inversion methods. Inclination bias also holds for a maximum acceptable misfit value chosen to be 1-σ of the RMS error of all directions tested (not shown in Figure 1.4). Finally, we note that in this example there is no noise or additional background field in these tests.

Given the fact that our analysis will now deal with shapes more complex than a single dipole, we stop our study of the single-dipole single dipole fit method.

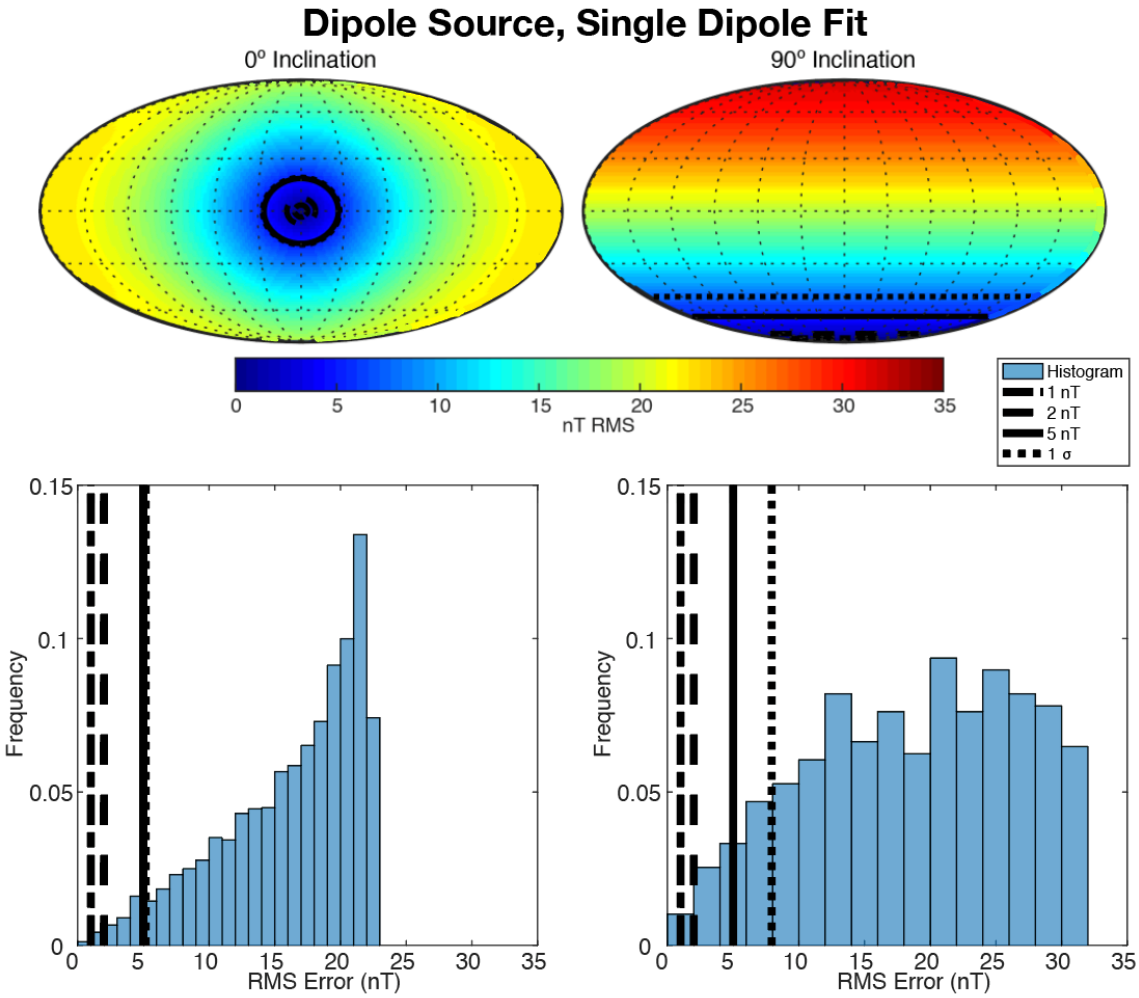

Figure 1.2: Maps and histograms of root mean squared (RMS) errors of tested magnetization directions for inversions for a single dipole's direction using the single

dipole fit method. The area of the error map is greater for higher inclinations, for a given maximum misfit (i.e., RMS error 1, 2, 5 nT). Shown are results using the radial magnetic field component only, for brevity. The results are similar for the north and east components. These maps are a Mollweide projection of magnetization directions tested, with declination on the y-axis and inclination on the x-axis, similar to Figure 1.1.

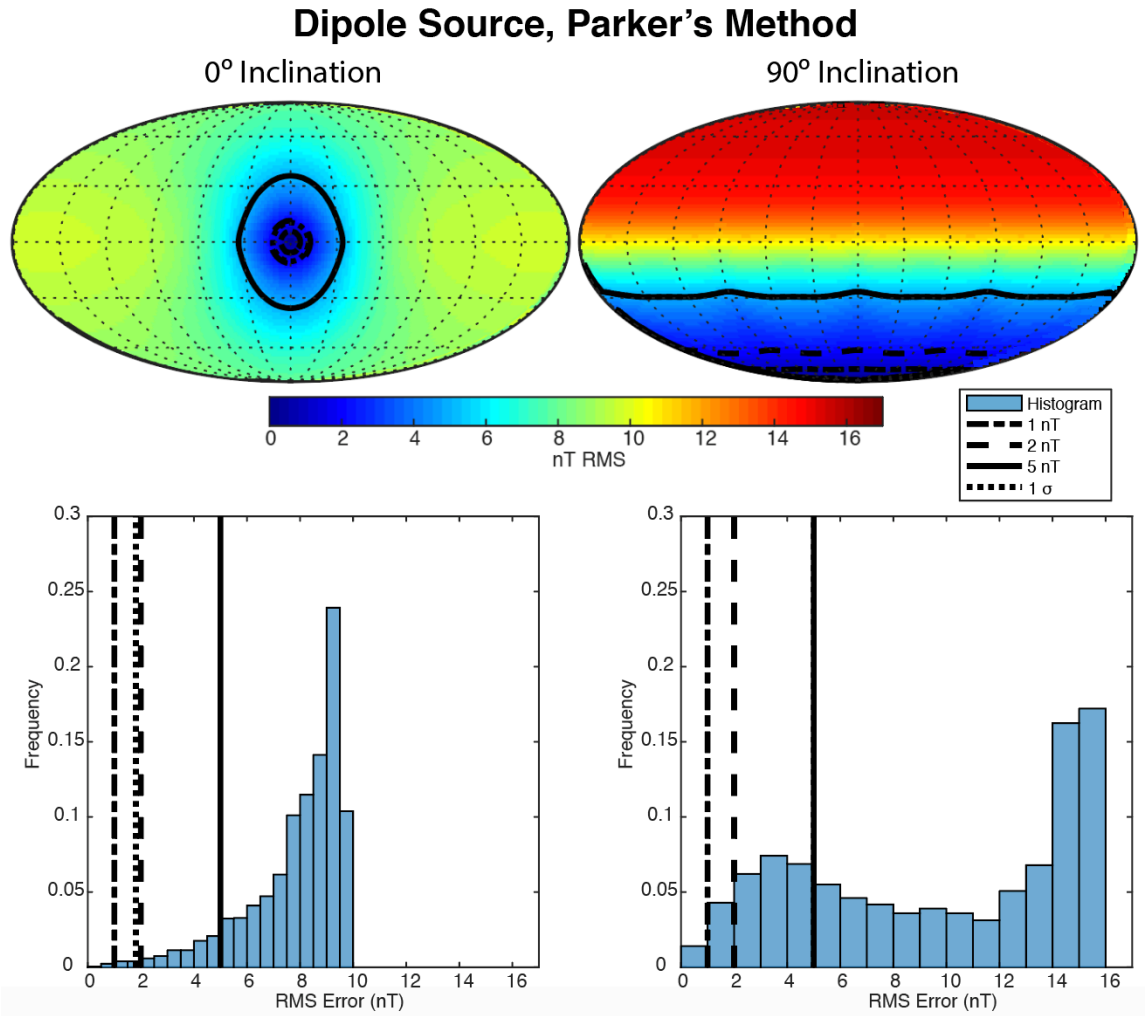

Figure 1.3: Maps and histograms of root mean squared (RMS) errors of tested magnetization directions for inversions for a single dipole's direction using Parker's Method. The area of the error map is greater for higher inclinations, for a given maximum misfit (i.e., RMS error 1, 2, 5 nT). The 1-σ maximum misfit is coincident with the 5 nT value for the 90° inclination case and is therefore not visible. Shown are results using the radial magnetic field component only, for brevity. The results are similar for the north and east components. These maps are a Mollweide projection of magnetization directions tested, with declination on the y-axis and inclination on the x-axis, similar to Figure 1.1.

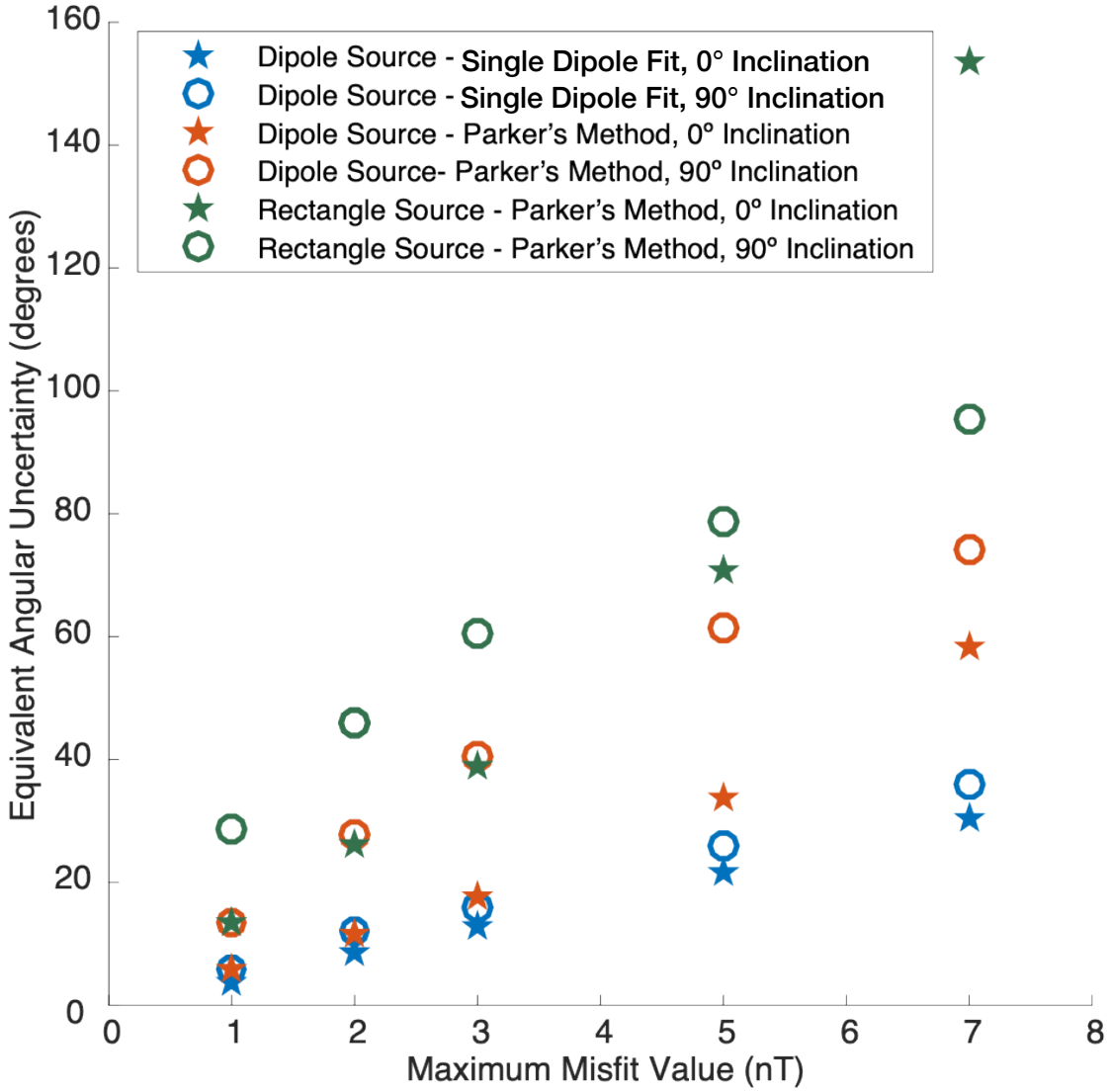

Figure 1.4: Equivalent angular uncertainty associated with inversions for the magnetization direction of a single dipole source, using the single dipole fit method (Figure 1.2), Parker's Method (Figure 1.3), and Parker's Method applied to a rectangle source (Figure 1.5). The uncertainty is always higher for 90° inclinations (i.e., the circles are always above the stars), except for a maximum misfit of 7 nT for the rectangular anomaly for the 0° inclination case (see text). Not shown are the equivalent angular uncertainties for a 1-σ maximum misfit, where in all cases the uncertainty is higher for 90° inclination.

3.2 Inclination Bias in Parker's Method Applied to Different Source Shapes

Inclination bias persists regardless of the shape of the magnetic source. We apply Parker's Method to each shape (Appendix Figure A1) and repeat the inversion for 19 different source inclinations (−90° to +90° inclination in 10° increments, all with 0° declination). The equivalent angular uncertainties for all shapes are larger for higher magnetization inclinations for nearly all of the maximum acceptable misfits chosen (RMS error 1, 2, 3, 5, and 7 nT, Figure 1.4). The only exception is a 7 nT maximum acceptable misfit for the rectangular source, which is 97.5% of the maximum RMS error for all test directions for the synthetic anomaly with 0° inclination. Hence, it is possible that at very large maximum acceptable misfit values, inclination bias may not appear. However, in practice one would never apply a maximum acceptable misfit so close to the maximum error in the inversion.

The origin of the inclination bias can be seen in the error histograms for the 90° inclination, which are flatter than the 0° inclination case, yielding a wider range of acceptable magnetization directions (Figure 1.5). Inclination bias also holds for a maximum acceptable misfit equal to 1-σ of the RMS error of all directions tested. Again, note that in this example, there is no noise or random background fields.

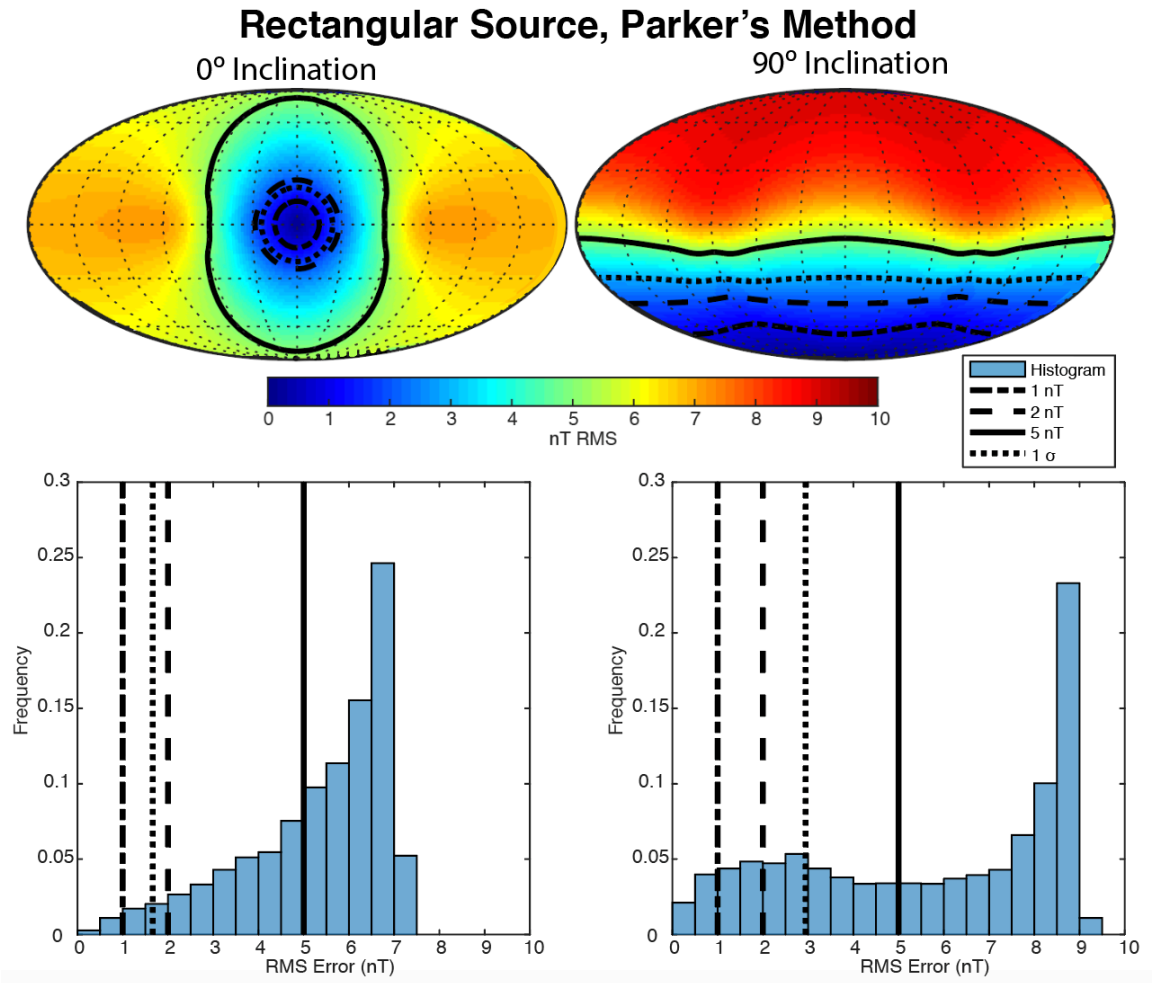

Figure 1.5: Maps and histograms of root mean squared (RMS) errors of tested magnetization directions for inversions for a rectangular source using Parker's Method (sources shown in supporting information). The area of the error map is greater for higher inclinations, for a given maximum acceptable misfit (i.e., RMS error 1, 2, 5 nT). Shown are results from Parker's Method using the radial magnetic field component only, for brevity. The results are similar for the north
and east components. These maps are a Mollweide projection of magnetization directions tested, with declination on the y-axis and inclination on the x-axis, similar to Figure 1.1.

The bias in recovering the magnetization direction remains regardless of what magnetic field component is used in Parker's Method. To demonstrate this, we used a 2 nT and 1-σ maximum acceptable misfit and calculated the equivalent angular uncertainty of the best-fit magnetization direction of a dipole and rectangular shape, using all three

magnetic components separately (Figure 1.6 and Appendix Figure A7). In all cases the uncertainty increased as the source body inclination increased. Finally, this finding also holds regardless of shape of the magnetic source (Appendix Figure A8).

Declination also has an effect on uncertainty, but is much smaller in magnitude. For example, a maximum of 15° uncertainty is produced from a dipole source and 30° for our rectangle source, compared to maximum of 75° inclination for both, using similar model parameters as for the inclination analysis (Appendix Figure A9). Furthermore, the uncertainty does not monotonically increase between 0° and 180°, unlike the monotonic increase with inclination from 0° to 90°, so we will not emphasize the effect of declination in the remainder of the paper.

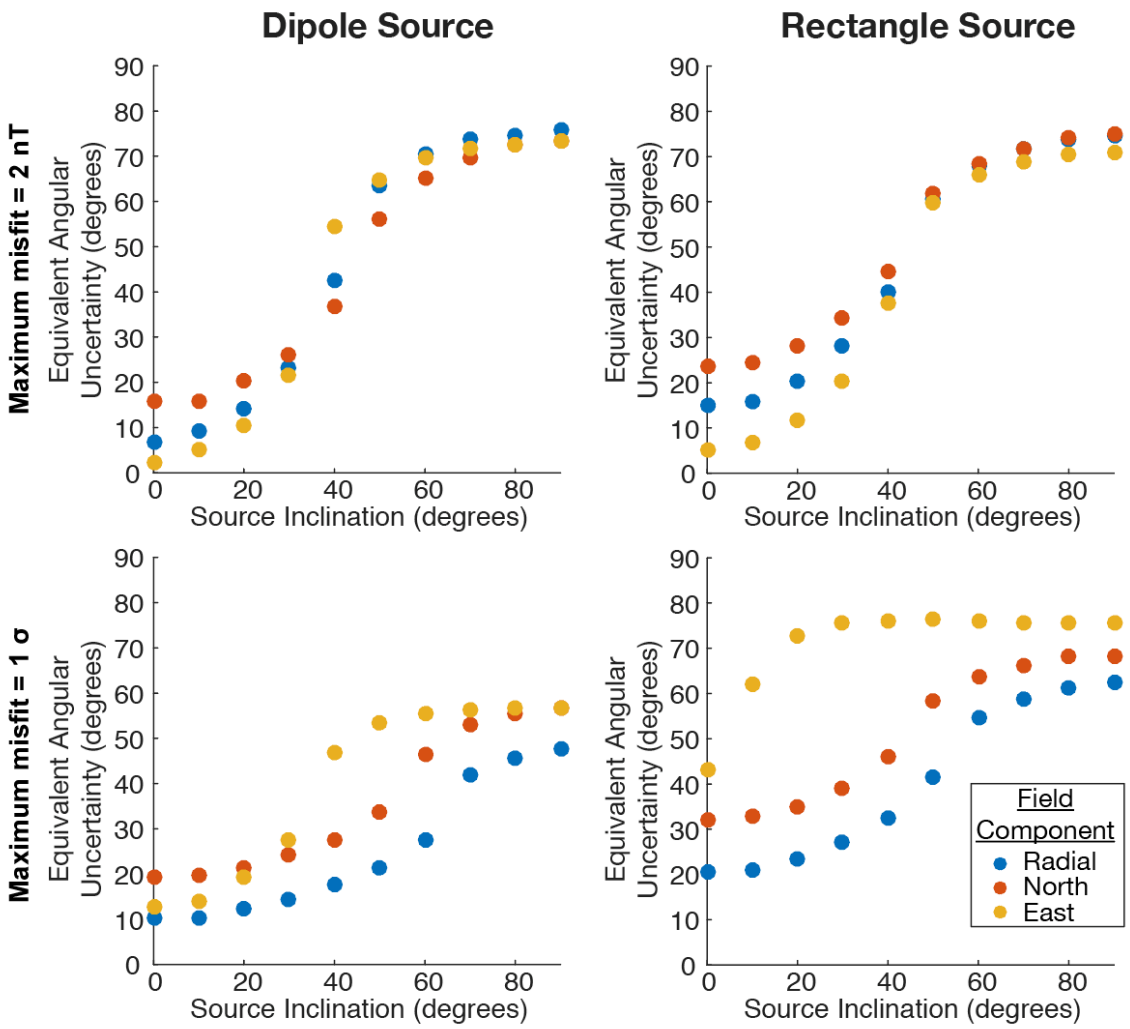

Figure 1.6: Higher inclinations give systematically higher uncertainties, referred to herein as inclination bias. Results shown here are for Parker's Method applied to the dipole and rectangle anomalies (with a constant 0° declination for all tests) using a maximum misfit of 2 nT (top rows) and 1σ (bottom rows). Negative inclinations are not shown, as the results are identical to those for positive inclinations. Note that some blue or red dots are occasionally obscured by yellow ones.

3.3. Inclination Bias in the Presence of Noise With Parker's Method

We find that inclination bias remains when a random background field is added to the source. To demonstrate this, we add a variety of background fields to the synthetic rectangular case for a series of datasets with SBR values up to ~35 (examples shown in

Figure 1.7), for 0 and 90° inclination magnetizations, and invert for the magnetization direction with Parker's Method (Figure 1.8 and Appendix Figure A3). The equivalent angular uncertainties for anomalies with 90° inclination (Figures 1.8c and 1.8d, unfilled circles) are greater than those with 0° inclination (Figures 1.8c and 1.8d, filled circles) at each SBR. Additionally, inversions show that using a maximum acceptable misfit value equal to the RMS background field (Figure 1.8c) have a greater variability in equivalent angular uncertainty than using 1-σ (Figure 1.8d) to define the maximum misfit. However, it is important to note that both choices of misfit value give larger uncertainties as the background field strength increases (SBR decreases). Examples of these differences can be seen in Figure 1.9.

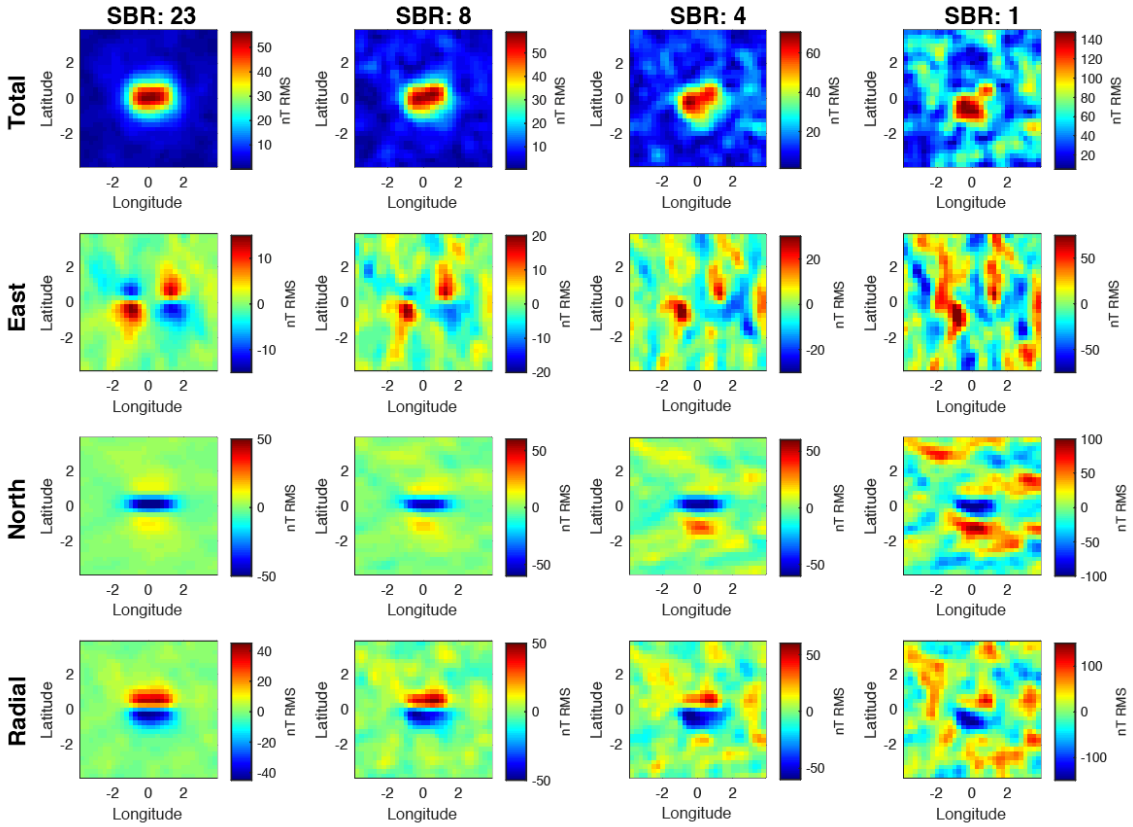

Figure 1.7: Synthetic background field oscillations added to the synthetic rectangular anomaly. Examples are for signal-to-background ratio (SBR) values of ~23 (like at the Reiner Gamma anomaly), ~8 (like at the Airy anomaly), 4, and 1. These cases were created by adding dipoles of random strength and direction to the synthetic rectangle anomaly data set (see Figure 1.4). The synthetic anomaly modeled here is at 0° inclination, 0° declination. These fields are calculated at 20 km altitude. Points within the data set are on a 0.25° x 0.25° grid.

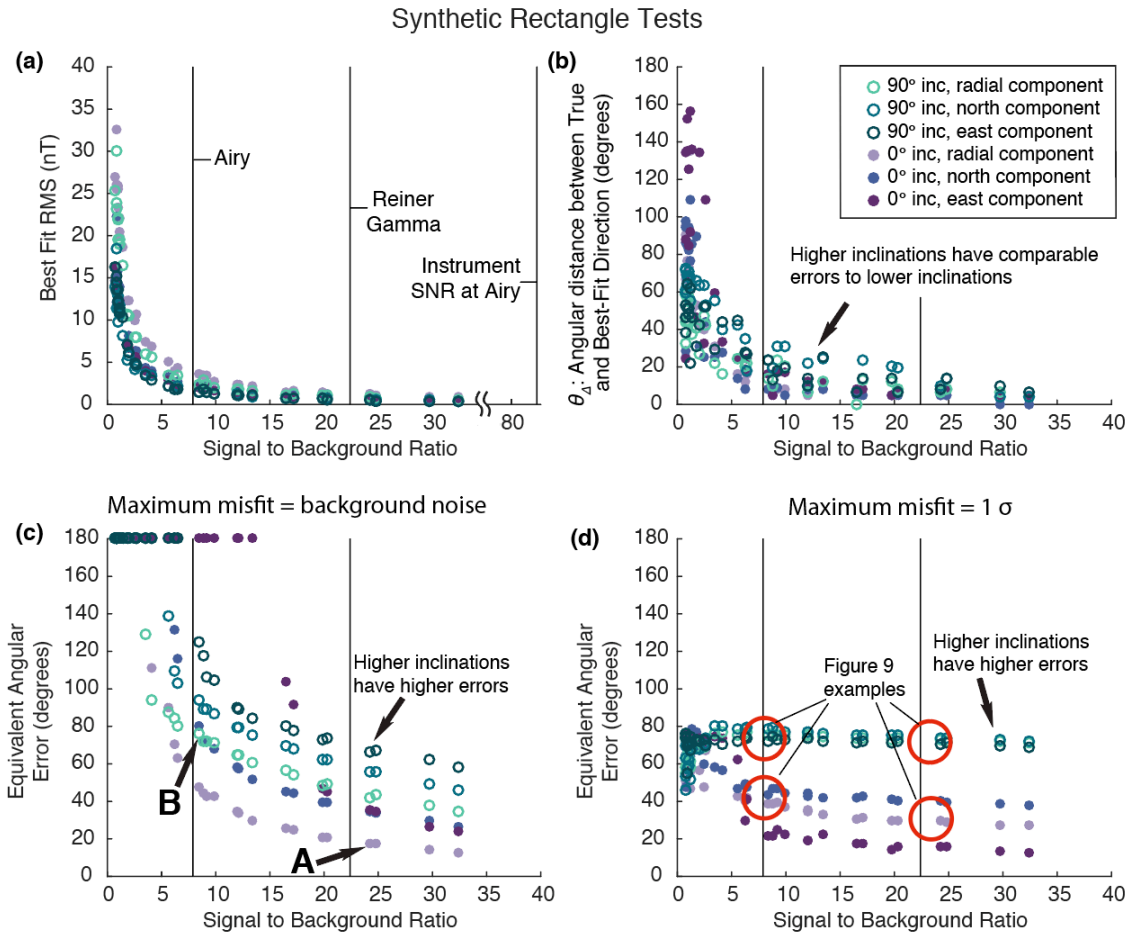

Figure 1.8: Inclination bias across different SBR values for a rectangular source with 0 and 90° magnetization inclination. (a) The best-fit root mean squared (RMS) value for differing signal-to-background ratio (SBR) values. The instrument SNR (Signal-to-Noise Ratio) at Airy is 8.3. (b) The angular difference between the true and best-fit directions θ_Δ. (c) The equivalent angular error for a maximum misfit equal to the RMS background field. (d) The equivalent angular error for a maximum misfit equal to 1 σ. The SBR values associated with the actual Reiner Gamma and Airy magnetic anomalies are denoted by vertical black lines at 23 and 8, respectively. All test cases have a declination of 0°. Label "A" on panel (c) indicates the test case most like the Reiner Gamma anomaly and label "B" indicates the test case most like the Airy anomaly.

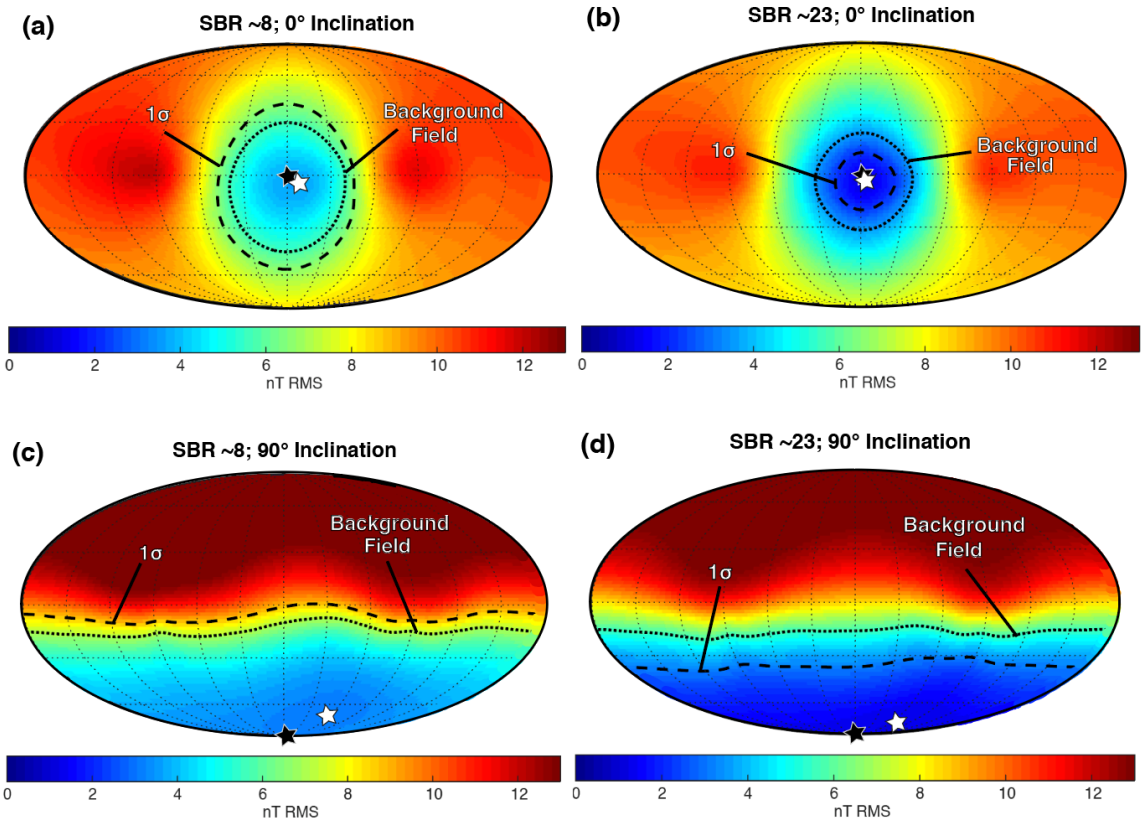

Figure 1.9: Error maps for selected cases indicated in Figure 1.8d (synthetic rectangular anomaly). The best-fit direction is close to the true direction, while the acceptable area within the maximum misfit (here equal to the background noise and 1-σ) grows as signal-to-background ratio (SBR) decreases. The black stars are the true directions, the white stars are best-fit directions; the angular difference between them is θ_Δ (Figure 1.8). Here, only the radial component is used in Parker's Method.

Our most essential finding is that regardless of the maximum acceptable misfit value chosen, the equivalent angular uncertainty (i.e., the uncertainty obtained from using a maximum misfit value) is always higher than the angle between the true and best-fit directions, θ_Δ, indicating that the maximum misfit method is overly conservative. For example, SBR values of 10–30 have equivalent angular uncertainties of ~10°–100° when using a maximum acceptable misfit (Figure 1.8c, depending on the field component used and anomaly inclination), while the true capability of Parker's Method has θ_Δ values of

only ∼10°–30° over the same SBR range for all components (Figure 1.8b and Appendix Figure A3). There is no strong dependence on field component or inclination value, but there is a slight suggestion of a ∼10° magnitude increase in θ_Δ with higher inclination for one field component (Figure 1.8b and Appendix Figure A3b). Ultimately, determining if θ_Δ depends slightly on inclination will require many more simulations with Parker's Method and will be the subject of future work. Regardless, we can summarize the preceding observations as follows: The uncertainties estimated using a maximum acceptable misfit are not only biased by inclination but are also unnecessarily conservative compared with the values of θ_Δ.

We show this effect visually in the error maps shown in Figure 1.9. Synthetic anomalies with 90° inclination have much larger uncertainties, as defined by maximum misfit, than the anomalies with 0° inclination. While θ_Δ from the 90° inclination anomalies are slightly larger compared to the 0° inclination cases (at least in this example of background-added data), the uncertainty from using a maximum misfit is much greater. In addition to our tests of precision, we assessed the accuracy of Parker's Method. That is, we checked that there was no directional bias in the deviation of the best-fit direction from the true direction. We started with a synthetic rectangle and produced 40 background-field-added test cases, for four SBR and magnetization direction conditions (0° and 90° inclination magnetizations each with 8 and 23 SBR, Appendix Figure A5). We found no evidence for obviously high levels of inaccuracy, at least for the cases explored, and hence we continue to focus on precision in the rest of the paper.

3.4 Lunar Magnetic Anomalies

We present in Figures 1.10, 1.11, Appendix Figure A4, and Table 1.2 the inversion results and Monte Carlo trials at Airy and Reiner Gamma, respectively, while relegating the others (Abel, Hartwig, and Sylvester) to the Supporting Information (Appendix Figures A10–A12). One interesting result is that Airy has an inclination higher than all of the other anomalies, and an uncertainty (standard deviation, s) ~5–10° higher than the other anomalies. This may reflect the slight increase in uncertainty with inclination, as suggested by our studies of a synthetic anomaly (Figures 1.8 and 1.9, above). Overall, we find substantially smaller uncertainties for all anomalies compared to Oliveira and Wieczorek (2017), with the exception of Reiner Gamma.

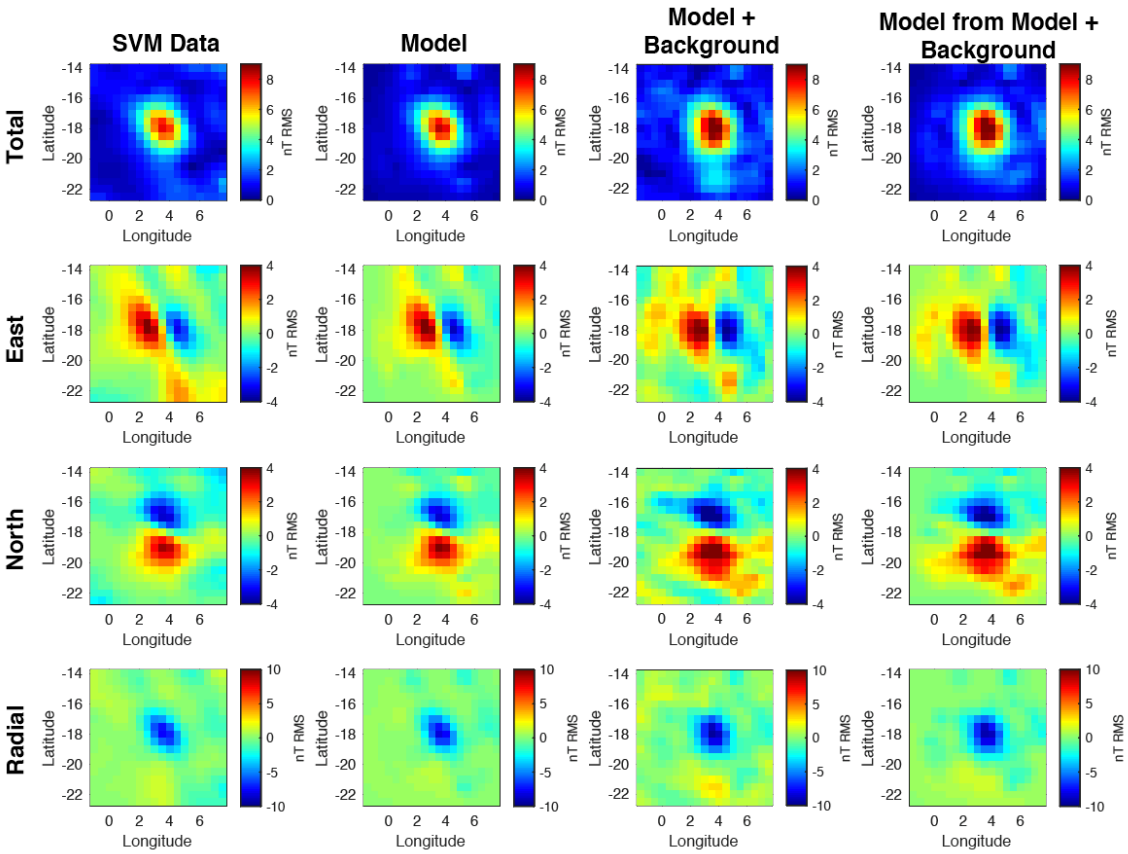

Figure 1.10: Magnetic field map of the Airy magnetic anomaly at 30 km altitude using the surface vector mapping (SVM) data set (Tsunakawa et al., 2015), the best-fit model of Airy from Parker's Method, the best-fit model plus background field appropriate for Airy (signal-to-background ratio [SBR] ≈ 8), and the bestfit model from Parker's Method applied to the model plus a background field. All datasets are at a 0.5° x 0.5° grid resolution.

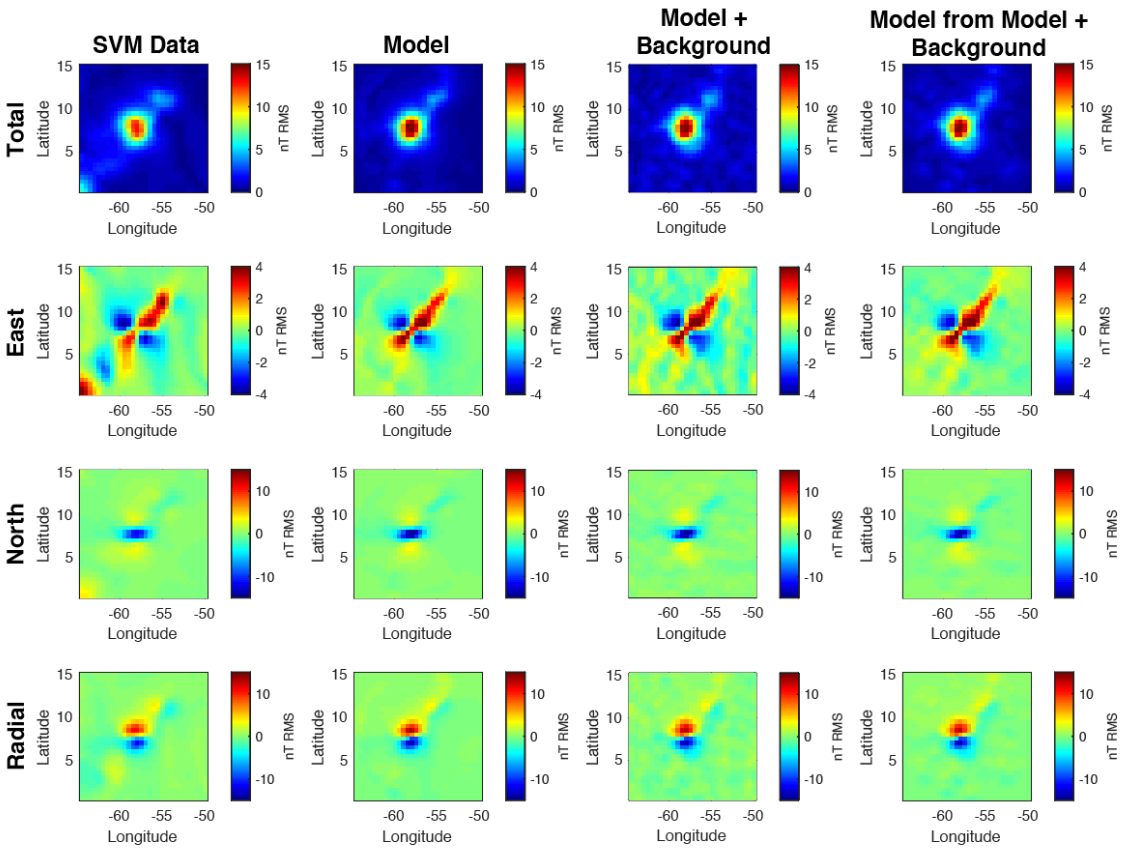

Figure 1.11: Magnetic field map of the Reiner Gamma magnetic anomaly at 30 km altitude using the surface vector mapping (SVM) data set (Tsunakawa et al., 2015), the best-fit model of Reiner Gamma from Parker's Method, the best-fit model plus background field appropriate for Reiner Gamma (signal-to-background ratio [SBR] ≈ 23), and the best-fit model from Parker's Method applied to the model plus a background field. All datasets are at a 0.5° x 0.5° grid resolution.

Paleopoles and their estimated uncertainties are shown in Figure 1.12. We also plot the paleo-spin axis locations from Garrick-Bethell et al. (2014); Keane and Matsuyama (2014); and Siegler et al. (2016) (Figure 1.12). Only Reiner Gamma overlaps with the range of estimated paleopoles, in particular, with the hydrogen paleopole extent discussed by Siegler et al. (2016). All four of the other magnetic paleopoles, Abel, Airy, Hartwig, and Sylvester, are closer to the equator.

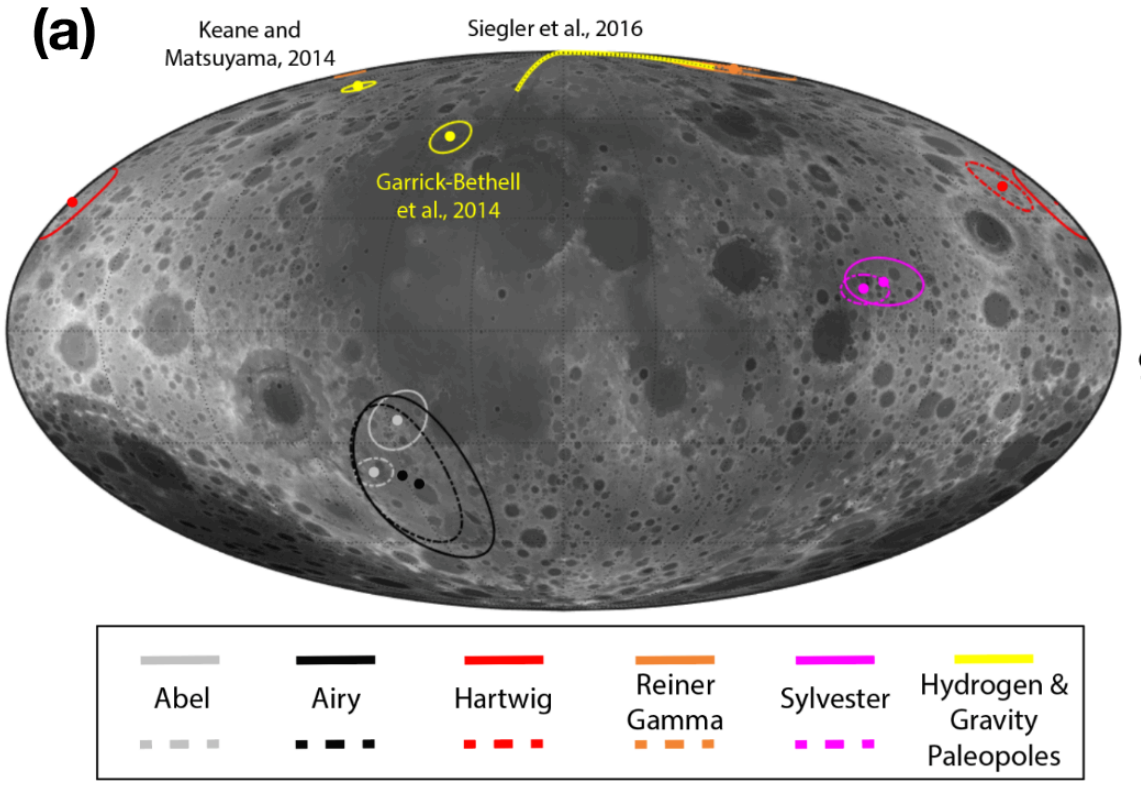
(a)
Keane and
Matsuyama, 2014
Siegler et al., 2016
Garrick-Bethell
et al., 2014
Abel
Airy
Hartwig
Reiner
Gamma
Sylvester
Hydrogen &
Gravity
Paleopoles

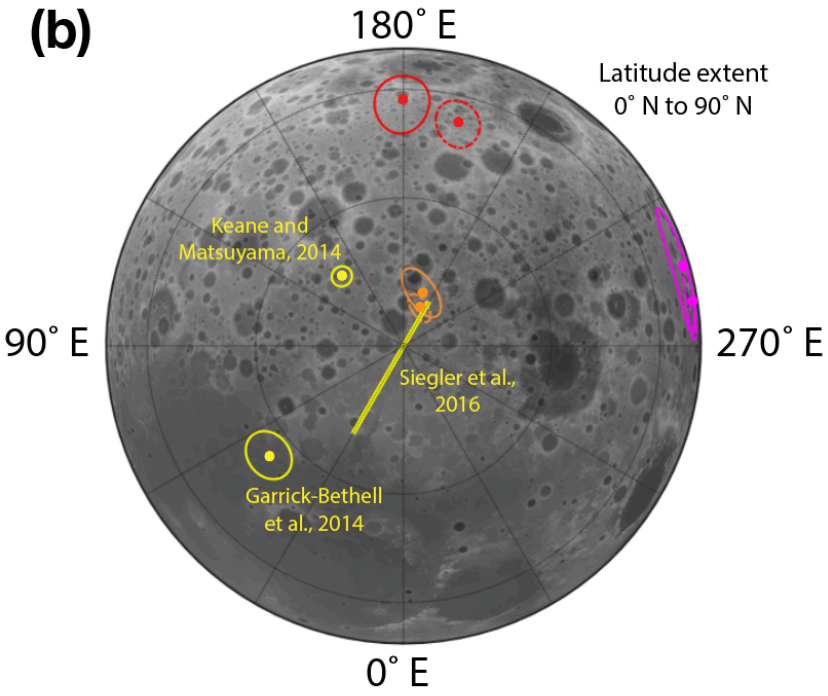
(b)
180° E
Latitude extent
0° N to 90° N
Keane and
Matsuyama, 2014
90° E
270° E
Siegler et al.,
2016
Garrick-Bethell
et al., 2014
0° E

Figure 1.12: Paleopole plot showing our results for Abel, Airy, Hartwig, Reiner Gamma, and Sylvester over Lunar orbiter laser altimeter topography data (Smith et al., 2010). Solid lines represent the larger of the two data extents tested for each anomaly while dashed lines represent the smaller (see Table 1.2 for details). The dm and dp values for the uncertainty ellipses are obtained from the 1-σ angular uncertainties, s, in Table 1.2. Paleopole location reported by Garrick-Bethell et al. (2014), Keane and Matsuyama (2014), and Siegler et al. (2016) are also shown. (a) Is a Mollweide projection centered on 0°N, 0°E. (b) Is a polar projection centered on the north pole with a latitudinal extent from 0°N to 90°N.

4 Discussion

4.1 Uncertainty Estimation

4.1.1 Maximum Acceptable Misfit versus Monte Carlo Methods

A combination of inclination bias and different SBR values helps explain particularly large differences in direction uncertainty at two lunar magnetic anomalies studied by Oliveira and Wieczorek (2017). They found a much lower uncertainty for the magnetization direction of the low-inclination Reiner Gamma magnetic anomaly (similar to the synthetic example in Figure 1.9b) compared to the high-inclination Airy anomaly (similar to the synthetic example in Figure 1.9c) when they used the RMS background field to define the maximum acceptable misfit. The synthetic tests in Figure 8c suggest that one would expect a magnetization direction error (θ_Δ) of ~20° at Reiner Gamma (SBR ≈ 23, filled circle for radial component, label A) using such a method. However, Oliveira and Wieczorek (2017) reported an uncertainty of zero. Their zero uncertainty comes from the fact that the RMS error of their best-fit solution at Reiner Gamma (0.61 nT) was larger than the RMS background field (0.56 nT, using the radial component). This is a general problem in using the background field to define the maximum misfit when the SBR or Signal-to-Noise Ratio values are high and the anomaly is well-modeled

as unidirectional. In contrast, our synthetic tests (Figure 8b) suggest that we would expect an uncertainty of <10° using θ_Δ, and indeed we find an s value of 3°–5.5° with our Monte Carlo simulations (Table 1.2).

As for the high-inclination Airy magnetic anomaly, Figure 1.8c suggests one would find an uncertainty of ~75° using the RMS background field using a maximum misfit (SBR ≈ 8, unfilled radial component circle, label B). This is consistent with the large uncertainties Oliveira and Wieczorek (2017) reported for the high-inclination Airy anomaly (their Figure 3c). In fact, the uncertainty they found was so high that Airy had to be excluded from their paleopole analysis for statistical reasons. In contrast, our synthetic tests predict an uncertainty of ~10°–20° using θ_Δ, and indeed we find an s value of 15°–17° with our Monte Carlo simulations (Table 1.2).

Overall, we can compare our results with what typically qualifies as "good," "fair," and "poor" results from the paleomagnetism community. Butler (1992) uses s values of roughly, 7°, 12°, and 25° for each of these adjectival ratings, and states that s > 15° (or k < 30, where k is the precision parameter) is typically viewed as unacceptable. Our results range from s = 3° at Reiner Gamma to s = 17° at Airy, and hence would typically be viewed as good to almost poor. However, for our purposes, even uncertainties that border on poor still enable us to assess the hypothesis that the lunar dipole was misaligned from the lunar spin axis (Section 4.2).

4.1.2 Additional Sources of Uncertainty

When testing how the radius of data used in Parker's Method (Methods Section 2.6) affects our results, we find that two anomalies, Abel and Hartwig, do not produce the same magnetization direction within their uncertainties. Abel, for example, has an angular difference of 19° between the two data radii used, while their uncertainties (s) are 8.8° and 5.6° (for radii 6° vs. 8°, Table 1.2). The chosen data radius also affects the properties of the background field (SBR), which in turn is used in the Monte Carlo simulations. Interestingly, Abel and Hartwig have both large differences in SBR values for their data radii (the SBR value for Abel with 8° is 1.5 times the SBR for 6°, while the SBR value for Hartwig with 9° is 1.8 times the SBR for 6°), and low SBR values. In contrast, Reiner Gamma whose SBR values are high for both radii (SBR = 14.3 and 22.9), shows much lower variability in its best-fit paleopole, despite SBR values with a factor of 1.6 difference between the two data radii chosen. Developing a formal framework to deal with these effects of data radius is a goal for future work.

4.2 Evidence for Near-Equatorial Lunar Paleopoles and a Nonaxial Lunar Dipole

The relatively small (dm < 25°) paleopole uncertainties (Figure 1.12) strengthen the argument that some magnetic paleopoles are indeed near the present-day equator as found by Oliveira and Wieczorek (2017). Using the degree-2 gravity and topography of the Moon, Garrick-Bethell et al. (2014) and Keane and Matsuyama (2014) independently estimated the extent of true polar wander on the Moon since as early as crust formation and found co-latitude changes of <36°. Siegler et al. (2016) also estimated the extent of true polar wander back to the Moon's later differentiation phase and found a maximum

co-latitude change of ~30° (Figure 1.12). Given that four of the paleopoles we report are far from the gravity and polar-hydrogen derived paleopoles, and almost all are closer to the equator within their uncertainties, we suggest that these four magnetic anomalies do not represent the ancient spin-axis, and therefore do not trace true polar wander. This implies that the dynamo dipole axis was decoupled from the spin axis, which could have implications for the dynamo mechanism. For example, Takahashi et al. (2009) suggested that the magnetic pole could reach low latitudes if the core-mantle boundary heat flux was heterogenous. Interestingly, Abel and Airy both have paleopoles overlapping, suggesting that this was possibly not a short-lived event, or that these anomalies formed contemporaneously. Based on a comparison with similar low-latitude magnetic paleopoles on Earth, Baek et al. (2019) also argued that it is not likely that lunar near-equatorial paleopoles are formed during transient dynamo axis motion, such as during reversals. On Earth, transition periods are much shorter than required cooling timescales (Meert et al., 1994; Mitchell et al., 2011; Symons & Chiasson, 1991). These transition periods are therefore less likely to be observed in the paleomagnetic field record (Halls et al., 2015).

The ages of lunar magnetic anomalies are not well determined. Reiner Gamma's age has been bounded between ~3.5 and −3.9 Ga (Kelley & Garrick-Bethell, 2020). However, the other four anomalies we analyzed have no published ages. Until such ages are obtained, it will be difficult to test for evidence of sustained epochs of equatorial magnetic poles. Finally, we note that it is unlikely that the field arises due to a quadrupolar component of the dynamo field, since such a component would decay to

~17% of the dipole term at the surface due to the small size of the lunar core (assuming a ~300 km radius).

There may also be other geophysical implications of low latitude magnetic poles. Garrick-Bethell et al. (2019) studied how the ancient dynamo field would have interacted with the early solar wind. They showed that an equatorial dipole would channel solar wind hydrogen over a substantial fraction of the surface as the Moon spins, in contrast to a spin-aligned dipole, which would block solar wind access from most of the Moon. If the Moon's polar hydrogen deposits are related to a global-scale "water cycle" related to solar wind hydroxylation of the entire lunar surface (Li and Garrick-Bethell, 2019; Li & Milliken, 2017; Pieters et al., 2009), then a near-equatorial dipole could have facilitated their accumulation.

5 Conclusions

1. Estimating uncertainty in magnetization direction using an a priori measure of maximum acceptable misfit (Figure 1.1, e.g., based on background crustal magnetic field oscillations or instrument noise) introduces bias depending on the anomaly magnetization direction: Higher inclination magnetizations have systematically higher uncertainties.
2. Estimating uncertainty in magnetization direction using an a priori measure of maximum acceptable misfit is also conservative: Parker's Method can recover nearly the correct magnetization direction for any inclination, in the presence of Gaussian background fields, for reasonable SBR values (Figure 1.8b). In contrast,

using the RMS background field as the maximum acceptable misfit value artificially increases uncertainty estimates substantially (Figure 8c vs. Figure 1.8d). A slightly higher uncertainty for high inclination anomalies may persist within Parker's method (Figures 1.8b and Appendix Figure A4b), which merits further study.

3. Manifestations of both conclusions 1 and 2 are believed to be responsible for the large direction uncertainty at the Airy anomaly (high inclination and lower SBR) and zero direction uncertainty at the Reiner Gamma anomaly (low inclination and higher SBR) in Oliveira and Wieczorek (2017). Hence, maximum acceptable misfit is not the appropriate means of quantifying uncertainty. Instead, the uncertainty should be estimated based on an estimate of the typical strength of the background non-unidirectionally magnetized sources in the region, as discussed in this study, and other sources of noise (e.g., instrument, not included in this study), if applicable. These estimates should then be used in Monte Carlo simulations that propagate each source of error through many instances of Parker's Method applied to a best-fit model of the anomaly in question. If the anomaly background contains smaller, discrete sources magnetized in a different direction (Thomas et al., 2018), then the user must avoid such sources in their data selection or somehow incorporate estimates of their properties into their Monte Carlo simulations (not considered here).
4. We find four paleopoles near the lunar equator when including uncertainties. Two paleopoles, Abel and Airy, overlap with each other, within their uncertainties.

Based on prior studies that estimated the extent of true polar wander from the lunar gravity field and polar hydrogen distribution, we conclude that these paleopole locations are not likely to be the result of true polar wander. Rather we interpret them to be due to a nonaxial dipole, as proposed by Takahashi et al. (2009) and Oliveira and Wieczorek (2017).

Chapter 2: Variations in Lunar Elastic Thickness from Admittance Spectral Analysis

Abstract

We infer the elastic thickness of regions of the Moon by performing an admittance analysis on GRAIL gravity and LOLA topography data. Reliable results are generally confined to the lunar farside, away from larger mare deposits. We find that elastic thickness varies between 9 km and 60 km, with a mean elastic thickness of 30 km. The highest reliable elastic thicknesses are found north of 60°N latitude while the lowest elastic thicknesses are found in the equatorial farside and within the South Pole-Aitken basin. Our findings suggest that much of the loading on the Moon must have taken place within the first 200 Myr of after lunar magma ocean solidification, though some areas (T_e>40 km) may be recording events as late at 3.5 Ga. We find no correlation between elastic thickness and crater density, crustal density, or crustal thickness in areas where reliable estimates of elastic thickness can be made. We also demonstrate that smaller localization windows can lead to systematically lower elastic thickness estimates.

1 Introduction

Characterizing how the surface of a planet supports loads reveals the physical mechanisms controlling its surficial responses and can provide insight into a body's thermal history. For example, Sori et al. (2018) have shown that the lunar highlands

could be supported via Airy isostasy and that the highlands likely formed early in lunar history, before the development of a thick elastic lithosphere. One way to validate the results of that study is to determine the effective lunar elastic thickness (T_e) and how it varies across the Moon.

The effective elastic thickness (T_e) is the minimum elastic thickness since the time of load emplacement. Determining the elastic thickness at a particular time in the Moon's history can elucidate its thermal history. If the time of loading can be estimated, then values of effective elastic thickness can be used to estimate the thermal gradient at that time (e.g., McGovern et al., 2002). For example, if the effective elastic thickness is high, that implies there was a low heat flux. This makes effective elastic thickness a useful way to place constraints on the thermal evolution of the Moon.

Effective elastic thickness can be measured using spatial features, i.e., the flexural wavelength of tectonic features, or spectral features, i.e., the transition from long-wavelength isostatic support to short-wavelength flexural support. In this paper, we focus on the spectral domain. Spectral analyses are common throughout planetary science, with examples on the Moon (discussed below), Mars (e.g., Ding et al., 2019), and Venus (e.g., Maia and Wieczorek, 2022).

Early analyses of the lunar elastic thickness include Arkani-Hamed (1998), Sugano and Heki (2004), and Crosby and McKenzie (2005), which all generally agree that the lunar elastic thickness required to support large impact basins at the time of their emplacement is between 20 km and 60 km. These studies used Clementine gravity data (Arkani-Hamed, 1998) and line of sight accelerations from Lunar Prospector (Sugano and

Heki, 2004; Crosby and McKenzie, 2005). More recent work has been done to analyze the elastic thickness in areas other than large impact basins, focusing mainly on small, localized areas. Huang and Wieczorek (2012) used Kaguya gravity model SGM100i (Goossens et al., 2011) and LOLA topography data (Smith et al., 2010) to analyze several locations where topography and gravity are correlated and find elastic thickness values between 5 km and 63 km, though these results are subject to large uncertainties. Zhong et al. (2014) analyzed gravity model CEGM02 (which uses measurements from Chang'E-1, Kaguya, and historical tracking data; Yan et al., 2012) and LOLA topography data to find elastic thickness values between 8 km and 97 km for various locations on the Moon, though they do not provide uncertainty estimates. Satya Kumar et al. (2018) use GRAIL (Gravity Recovery and Interior Laboratory) gravity model GL0990D (Konopliv et al., 2014) and LOLA topography data to analyze the farside highlands using the Maximum Entropy Method and find an elastic thickness of 19 km (uncertainty not provided). Zhong et al. (2019a) used GRAIL gravity model GL0990D and LOLA topography data to analyze the elastic thickness of Clavius crater (also analyzed by Crosby and McKenzie, 2005) and found an elastic thickness of 7 km (uncertainty not provided). Zhong et al. (2019b) used a GRAIL gravity model GL1500E (Park et al., 2015) and LOLA topography data to analyze the elastic thickness of Moscoviense and found a value of 18 km (uncertainty not provided). A majority of the analyses listed above fit a narrow range of spherical harmonic degrees in order to isolate particular spatial features. As we will argue below, such a restricted range has the potential to miss the most distinguishing features of an admittance spectrum.

The only prior effort to globally map elastic thickness was produced by Audet (2014) using the SGM100h gravity model (Matsumoto et al., 2010) and topography model LALT360 (Araki et al., 2009), both from the Kaguya-SELENE mission. Audet (2014) uses a wavelet analysis approach to find elastic thickness values between 10 km and 50 km with typical standard deviations of less than 5 km. He finds that elastic thickness varies globally with lower elastic thicknesses for the farside and higher elastic thicknesses under the Procellarum KREEP Terrane (PKT).

Few authors have explicitly calculated the uncertainties associated with their results, which poses two risks. The first is that, in the absence of uncertainties, one cannot determine whether apparent variations in parameter values are real or not. The second risk is that values which are unreliable (i.e., have large error bars) may be taken as reliable if the uncertainties are not stated. Error bars can also potentially flag cases when the underlying assumptions made are simply inappropriate. For example, a two-layer admittance analysis would be inappropriate in areas with mare volcanism, given that mare is effectively a third, denser layer than the underlying crust. In this work, we expend considerable effort on uncertainty estimation.

To our knowledge, no mapping of effective elastic thickness has been performed globally using updated GRAIL gravity models. Here, we make use of the spectral domain using the GRAIL gravity model GRGM1200A (Lemoine et al., 2014[1]) and LOLA topography data to map effective elastic thickness values across the globe. We also

[1] Lemoine et al., 2014 describes gravity model GRGM900C. Gravity model GRGM1200A was released in 2016, and at the time of release, the best citation for this data product was Lemoine et al., 2014.

discuss the uncertainties associated with our results and whether the resulting variations in elastic thickness are real.

2 Methods

2.1 Admittance and coherence observations

The admittance is the ratio of gravity to topography at a specific spherical harmonic degree *l*:

$$Z(l) = \frac{D_l^{gh}}{D_l^{hh}} \qquad (1)$$

where $Z(l)$ is admittance at a particular degree l, D^{gh} is the cross-correlation (equation 2) between free-air gravity (g) and topography (h), and D^{hh} is the autocorrelation of topography. Auto- and cross-correlations are defined as

$$D^{xy} = \sum_{m=0}^{l} C_{lm}^x C_{lm}^y + S_{lm}^x S_{lm}^y \quad (2)$$

where C_{lm} and S_{lm} are spherical harmonic coefficients of degree l and order m. Traditionally, admittance has units of mGal km^{-1}. However, lunar topography is sufficiently rugged such that lunar gravity is not well approximated by the thin sheet model, and thus a series approach that considers the finite amplitude of the topography is used instead (Wieczorek and Phillips, 1998). It is therefore useful to consider a dimensionless version of admittance. Dimensionless admittance can be obtained by using gravity calculated from topography (units of mGal, and assuming a given crustal density) in the place of topography. Now that admittance is dimensionless, the theoretical maximum admittance value becomes one (Figure 2.1). Equation 1 then becomes

$$Z'(l) = \frac{D_l^{gb}}{D_l^{bb}} \qquad (3)$$

where *b* is gravity-from-topography. The gravity-from-topography is found by using a 9th-order finite-amplitude correction (Wieczorek & Phillips 1998) where the topography is from LOLA (Smith et al. 2010) and the density assumed is 2500 kg m^{-3} (Lemoine et al. 2014[2]). We use an updated GRAIL (Zuber et al., 2013) gravity model from Lemoine et al. (2014) for free-air gravity. It is important to note, however, that the gravity-from-topography model assumes a constant crustal density of 2500 kg m^{-3} (Lemoine et al., 2014). Crustal density is not constant across the globe (Wieczorek et al., 2013), and thus equation 3 will produce admittance values greater than one in areas where the crustal density has been underestimated. We will need to account for this when modeling admittance (see next section).

It is also useful to describe how well gravity and topography (or gravity-from-topography) are correlated. Here we use coherence (γ^2), which is the square of correlation. This can be written as

$$\gamma^2(l) = \frac{D_l^{gb} D_l^{gb}}{D_l^{bb} D_l^{gg}} \quad (4)$$

To calculate the standard errors associated with admittance and coherence, we follow Bendat and Piersol (2010) and use the following equations:

$$\sigma_Z(l) = \left|\frac{Z(l)}{\gamma(l)}\right| \sqrt{\frac{1-\gamma(l)^2}{2l}} \quad (5)$$

$$\sigma_\gamma(l) = \frac{1-\gamma(l)^2}{\sqrt{2l}} \quad (6)$$

[2] Lemoine et al., 2014 uses a crustal density of 2560 kg m^{-3} to calculate their Bouguer Gravity Model. The .lbl file for GRGM1200A cites a crustal density of 2500 kg m^{-3}. We use the value cited in the .lbl file.

where γ is correlation. However, we are using coherence instead of correlation, so we use the chain rule to calculate the standard error of coherence as

$$\sigma_{\gamma^2}(l) = 2\frac{\gamma^2}{\gamma}\frac{1-\gamma(l)^2}{\sqrt{2l}} \qquad (7)$$

In order to map the variations in elastic thickness, we must perform localized analyses. However, there is a tradeoff between spatial and spectral resolutions (Wieczorek and Simons, 2005). Smaller localization windows lose the information held in wavelengths that are larger than the window, but larger windows decrease the spatial resolution of the observation. We choose a localization window in the form of a spherical cap with a radius θ= 25° and perform localized analyses every 15° on a grid of latitude and longitude. We discuss the effect of varying the window size in Section 4.1.

In addition to choosing the size of the localization window, we also apply the use of multitapers. Multitapers gradually filter out data from outside the region. We choose to use a single, well-concentrated (e.g., $\lambda \geq$ 99%, where λ the concentration factor) taper and thus we choose the lowest spectral bandwidth that produces only one such taper. For our window size of radius θ= 25°, this requires that our spectral bandwidth (L_{win}) be 10. For this work, we use the spatiospectral localization technique of Wieczorek and Simons (2005). This is done using the SHTOOLS package (Wieczorek and Meschede, 2018).

Given our choice of L_{win}, we fit the observed admittance and coherence starting at $l_{min} = L_{win} = 10$ and ending at $l_{max} = 60$, where admittance and coherence generally begin to asymptote at unity. We also ignore gravity coefficients at $l = 2$ in order to exclude the effects of the rotational and tidal contributions to degree 2 from our analysis.

2.2 Admittance and coherence modelling

The dimensionless version of admittance, assuming only surface loading and a Cartesian geometry, can be modeled as

$$Z'(l) = 1 - \left[e^{-kt_c} \frac{\Delta\rho}{\frac{Dk^4}{g} + \Delta\rho} \right] \qquad (8)$$

$$k = \sqrt{\frac{l(l+1)}{R^2}} \qquad (9)$$

where k is the wavenumber (units of m^{-1}), t_c is the crustal thickness (units of m), $\Delta\rho$ is the difference in crustal and mantle densities (units of kg m^{-3}), D is the flexural rigidity (units of N m), and g is gravity (units of m s^{-2}) (e.g., McKenzie, 2003). D is defined as

$$D = \frac{ET_e^3}{12(1-\nu^2)} \qquad (10)$$

where E is Young's Modulus (units of Pa), T_e is the elastic thickness (units of m), and ν is Poisson's ratio (dimensionless). In our modeling, we use crustal thickness and crustal density values from Wieczorek et al. (2013). We keep the following variables constant: mantle density (3220 kg m^{-3}, [Wieczorek et al., 2013]); Young's Modulus (100 GPa); Poisson's ratio (0.25); and lunar gravity (1.62 m s^{-2} at the lunar surface where R is 1737.4 km).

Examples of admittance and coherence spectra resulting from surface loading only are shown in Figure 2.1a. As elastic thickness increases, the admittance increases at lower spherical harmonic degrees (longer wavelengths). For instances with only surface loading, the coherence is one at all degrees, given that gravity is necessarily correlated with topography when all the loads are at the surface.

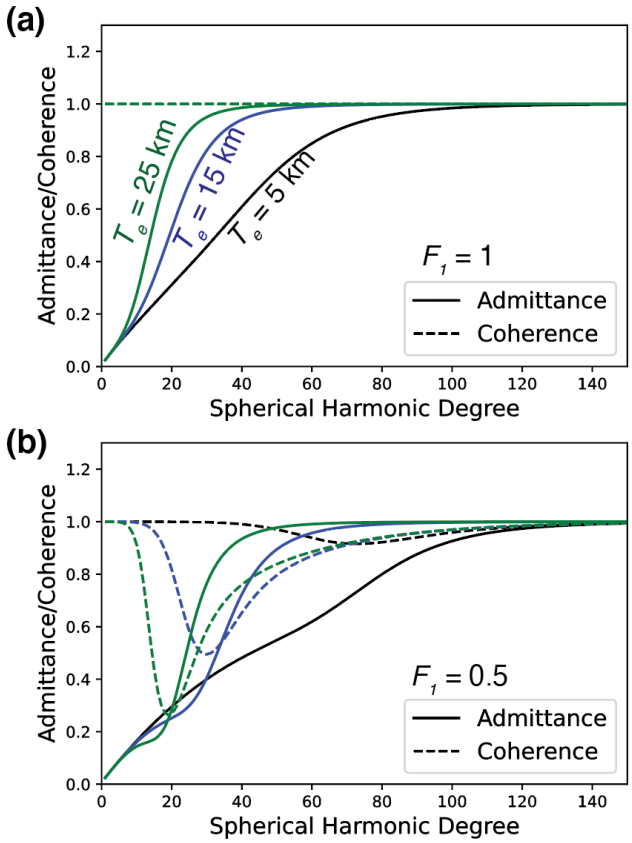

Figure 2.1: a) Dimensionless model admittance (thick lines) and coherence (dashed lines) at T_e = 5 km (black), 15 km (blue), and 25 km (green) for top loading (F_1 = 1). Model spectra shown were calculated using a Young's modulus of 100 GPa, a crustal thickness of 30 km and mantle and crustal densities of 3300 and 2550 kg m^{-3}, respectively. b) same as in (a) but for equal parts top and bottom loading (F_1 = 0.5).

It is also possible to have subsurface loading, either instead of or in combination with surface loading. If extra material is added to the base of the crust, the crust will flex upward by some amount depending on its rigidity. This causes admittance to be negative (while surface loading produces positive admittance). We adopt a relatively simple model of subsurface loading, based on McKenzie (2003), in which the surface and subsurface loads are assumed to be uncorrelated, and the geometry is Cartesian. The admittance from subsurface loading is given by

$$Z_2{}'(l) = 1 - \left[e^{-kt_c} \frac{\frac{Dk^4}{g} + \rho_c}{\rho_c} \right] \qquad (11)$$

where ρ_c is the crustal density. We define a loading fraction where F_1 is the fraction of surface loading and F_2 is the fraction of subsurface loading. Adding F_1 and F_2 together will always equal one. We now label the admittance from equation 8 as Z_1' and the total admittance becomes

$$Z' = \frac{\sum F_i^2 Y_i^2 Z_i}{\sum F_i^2 Y_i^2} \qquad (12)$$

where Y_i are parameters dependent on the rigidity and defined in McKenzie (2003) as

$$Y_1 = \frac{1}{\rho_c - \rho_w} \left(\frac{\frac{Dk^4}{g} + \rho_m - \rho_c}{\frac{Dk^4}{g} + \rho_m - \rho_w} \right) \qquad (13)$$

$$Y_2 = -1 \left(\frac{Dk^4/g + \rho_m - \rho_c}{Dk^4/g + \rho_m - \rho_w} \right)^{-1} \qquad (14)$$

where ρ_c is the density of the crust, ρ_m is the density of the mantle, and ρ_w is the density of the overlying crust (which in this case is zero because we are assuming a model with only two-layers). Total coherence becomes

$$\gamma^2 = \left(1 + \frac{\sum F_i^2 Y_i^2 \left[\left(Z'i/Z' \right)^2 - 1 \right]}{\sum F_i^2 Y_i^2} \right)^{-1} \qquad (15)$$

Examples of admittance and coherence spectra resulting from a mix of surface and subsurface loading are shown in Figure 2.1b. As before, when the elastic thickness increases, the admittance increases at lower degrees. However, the coherence is not one at all degrees, and the dip in coherence shifts to lower degrees as elastic thickness

increases. As the loading fraction decreases (i.e., subsurface loading increases), the dip in coherence increases.

It is possible that there are additional loads in the subsurface that generate gravity anomalies without producing any corresponding topography (McKenzie, 2003). The existence of these loads is debated (Kirby and Swain, 2009; Audet, 2014), but if they do exist, then coherence will necessarily decrease further (Figure 2.1b).

We note here that we choose to use coherence over correlation for this analysis for two reasons. The first is that, because we have assumed *a priori* that surface and subsurface loads are uncorrelated, the sign of the correlation is not so relevant. The second is that, as the square of correlation, coherence is more sensitive to deviations from unity. This sensitivity is particularly desirable in determining the ratio of surface and subsurface loading.

Missing from this analysis is a careful consideration of the phase of surface and subsurface loading. In principle, we could solve for this phase lag as an additional free parameter (e.g., Wieczorek, 2006). However, this approach has not in general been attempted, and we do not do so here. Locations where surface and subsurface loads would be correlated are areas where there is a combination of subsurface loading in the form of moho uplift (such as in craters) and surface loading in the form of mare infill. As we show below, such areas do not produce reliable elastic thickness estimates using our approach.

Recall from our discussion of dimensionless admittance that some observed admittance spectra will have values greater than one in areas where the crustal density

assumed (2500 kg m^{-3}) underestimates the actual local density. We use an amended admittance model in order to account for the density differences. We multiply equation 12 by a ratio of local crustal density (derived from the short-wavelength admittance in Wieczorek et al., 2013) to the model crustal density used in Lemoine et al. (2014), so admittance becomes:

$$Z^* = \frac{\rho_c}{\rho_b} Z' \qquad (16)$$

where ρ_b is 2500 kg m^{-3} (Lemoine et al., 2014). This allows our model to fit admittance values while taking observed variations in crustal density into account.

2.3 Markov Chain Monte Carlo Approach

To determine the elastic thickness (T_e) and loading fraction (F_l) that best fit the observed admittance and coherence spectra with models, we use a Markov chain Monte Carlo (MCMC) approach, using the *emcee* package from Foreman-Mackey et al. (2013). We use a posterior distribution to estimate the posterior probability:

$$P\left(X|Z^{obs}(l), \gamma^{2,obs}(l)\right) \propto P(X)P(Z^{obs}(l), \gamma^{2,obs}(l)|X) \qquad (17)$$

where *P(X)* is a uniform distribution such that T_e is allowed to vary between 0 km and 200 km and F_l is allowed to vary between 0 and 1 with no bias toward a particular value. We use an exponential form of the chi-squared function $\chi^2(X)$ for the posterior likelihood $P(Z^{obs}(l), \gamma^{o2,bs}(l)|X)$, assuming that observational errors are independent Gaussian distributions with standard deviations of $\sigma_Z^{obs}(l)$ and $\sigma_{\gamma 2}^{obs}(l)$ (from equations 5 and 7).

$$P(Z^{obs}(l), \gamma^{2,obs}(l)|X) \propto \exp\left(-\frac{\chi^2(X)}{2}\right) \quad (18)$$

$$\chi^2(X) = \sum_{l=l_{min}}^{l=l_{max}} \left(\frac{Z^{model}(l,X) - Z^{obs}(l)}{\sigma_Z^{obs}(l)}\right)^2 + \left(\frac{\gamma^{2,model}(l,X) - \gamma^{2,obs}(l)}{\sigma_{\gamma^2}^{obs}(l)}\right)^2 \quad (19)$$

In our MCMC inversions, we fit both the admittance and coherence spectra (equation 19) from degree 10 to degree 60. The lower bound of l_{min} = 10 is so we avoid fitting degrees that do not fit within the localized window, as described in Section 2.1. The upper bound of l_{max} = 60 is chosen somewhat arbitrarily, as admittance and coherence spectra tend to asymptote well before degree 60. Note that equation (19) gives equal weight to the admittance and coherence in terms of goodness-of-fit. We also use a combined root mean square (RMS) of admittance and coherence to measure the reliability of our results, which we define as:

$$RMS_{combined} = \sqrt{\frac{1}{N}\sum_l^N \left(Z_{obs,l} - Z_{model,l}\right)^2} + \sqrt{\frac{1}{N}\sum_l^N \left(\gamma^2{}_{obs,l} - \gamma^2{}_{model,;}\right)^2} \quad (20)$$

where N is the total number of degrees l modeled.

Examples of results from an MCMC inversion at two different locations can be seen in Figure 2.2. The standard deviations in elastic thickness and loading fraction are quite low, regardless of the goodness of fit for each inversion. The standard deviation in elastic thickness at -15°N, 180°E (Fig. 2.2a), 0.38 km, is larger than the standard deviation at 45°N, 45°E (Fig. 2.2b), 0.05 km, despite the former having lower chi-squared and combined RMS values than the latter. This implies that, in some instances, the standard deviations provided by the MCMC inversions are unreliable indicators of uncertainty, most likely because the uncertainties are neither Gaussian nor independent.

Note that here the uncertainties are not due to uncertainties in the gravity or topography coefficients themselves; rather, they arise from "geologic noise": the lumping together of different terranes into a single region, the existence of lateral variations in density, elastic thickness or loading fraction, variations in phase between surface and subsurface loading, and so on. We therefore perform tests on synthetic datasets in order to determine which values from our MCMC inversions are realistic and whether the standard deviations obtained from an MCMC inversion can be used as reliable indicators of the true uncertainty.

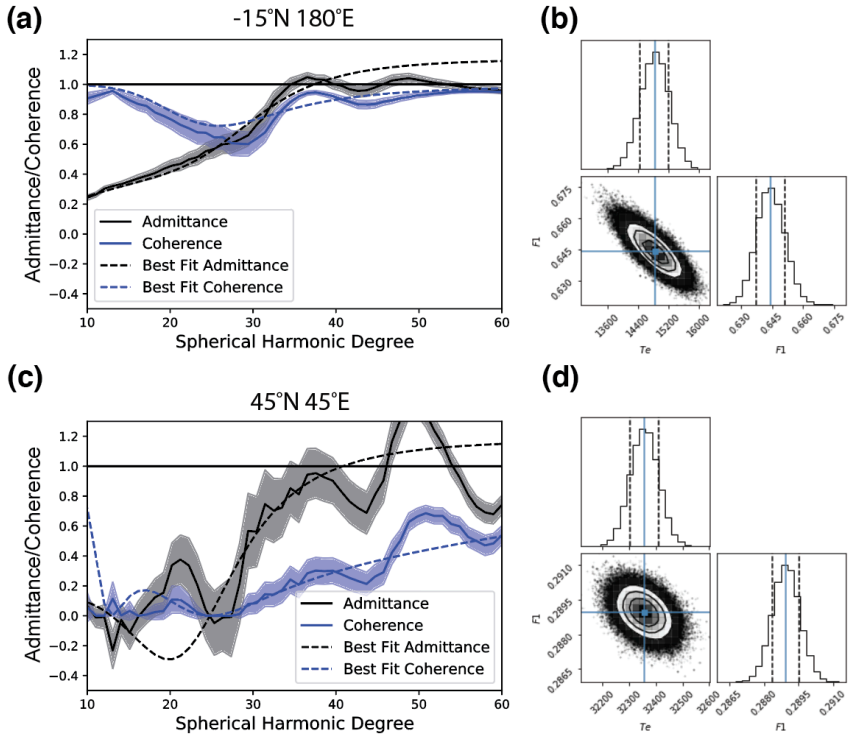

Figure 2.2: a) Observed admittance and coherence spectra (thick black and blue lines, respectively) with the best-fit model admittance and coherence (dashed lines) for a region centered on -15°N and 180°E. The combined RMS value is 0.152, so we would accept the derived parameter values as reliable (see text). b) Corner plot showing the distribution of combinations of elastic thickness (in meters) and loading fraction tried by the MCMC inversion. The blue target indicates the best-fit combination, which is modeled in (a). Black lines indicate the 1-, 2-, and 3-σ levels. c) Same as in (a) but at 45°N and 45°E. The combined RMS value is 0.443, beyond the threshold at which the derived parameter

values become unreliable. d) same as for (b) but for a region centered on 45°N and 45°E. Note that in both cases, the best-fit model admittance asymptotes to values greater than 1 because we use the local crustal density based on Wieczorek et al. (2013), which is greater than 2500 kg m^{-3}, the density assumed in the gravity models (Lemoine et al., 2014).

2.4 Synthetic Noise Tests

Though the MCMC approach provides a measure of uncertainty, we tested the robustness of this uncertainty measurement by creating synthetic admittance and coherence spectra. To do this, we multiply a model admittance spectrum (e.g., equation 12) by the gravity-from-topography to generate synthetic gravity data. We then add noise iteratively to the synthetic gravity coefficients in increments until the synthetic coherence spectrum matches the observed coherence spectrum within the standard error of coherence. The amount of noise added in each iteration is chosen from a gaussian distribution with a standard deviation equal to the error estimated for each coefficient from the equation

$$\Delta C_{lm} = 1.96\, C_{lm} \left(\frac{\gamma_l^{-2} - 1}{2l+1} \right)^{1/2} \qquad (21)$$

where 1.96 is from Munk and Cartwright (1966). Noise for the *S* coefficients is calculated similarly. In some cases, the synthetic coherence is lower than the observed coherence for a particular degree before any noise is added. Adding more noise to coefficients at these degrees would only decrease the coherence more, so in these cases, we do not add noise and use the synthetic coherence value, regardless of how well the synthetic matched the observed value.

We test 13 locations with varying fits (as described by the combined RMS of the difference between the observed and modeled spectra from l=10 to l=60). We create 20 such noise-added synthetic spectra for each location we test and use the MCMC approach to determine how much variability in the derived best-fit elastic thickness and loading fraction values arises due to the stochastic noise added. The variability in the derived best-fit values indicate how uncertain these values are, while any offset from the known (input) parameter values is an indication of systematic bias.

Figure 2.3 shows two examples of these noise-added spectra. In the first case (Fig. 2.3a), the mean best-fit elastic thickness is 15.3 km with a standard deviation across our 20 realizations of 0.21 km, while the actual (input) elastic thickness is 14.8 km, with an MCMC-derived standard deviation of 0.38 km. The mean best-fit loading fraction is 0.62 with a standard deviation of 0.001, as compared with the actual fraction of 0.644, with an MCMC-derived standard deviation of 0.007. Note that here, the standard deviations derived from the 20 synthetic spectra are smaller than the MCMC-derived standard deviations. In the case of elastic thickness, the best-fit value from the observed data agrees with the mean best-fit value from the synthetic spectra within 2.5 standard deviations from either method. The best-fit (from observations) and mean (from synthetic spectra) loading fractions, however, only agree within 3 standard deviations if we use the MCMC-derived standard deviation.

In the second case (Fig. 2.3b), the mean best-fit elastic thickness is 30.8 km with a standard deviation of 2.7 km, while the actual (input) elastic thickness is 32.3 km, with an MCMC-derived standard deviation of 0.05 km. The mean best-fit loading fraction is

0.289 with a standard deviation of 0.021, as compared with the actual fraction of 0.289, with an MCMC-derived standard deviation of 0.001. Here, the MCMC-derived standard deviations for elastic thickness (0.05 km) and loading fraction (0.001) are unreasonably small, while the standard deviations from the synthetic values appear reasonable (σ_{T_e} = 2.7 km and σ_{F1} = 0.021). The combined RMS value for this result is 0.443, which is high compared to the combined RMS of the other location (0.152) and suggests that these results may simply be unreliable. Therefore, it is important to determine what combined RMS values we would consider acceptable in order to distinguish whether a result is reliable.

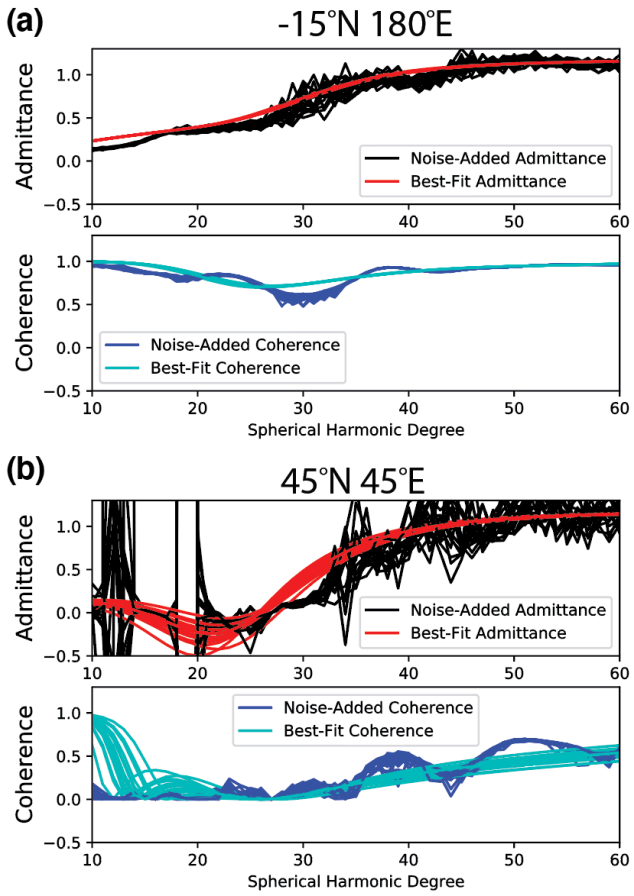

Figure 2.3: Synthetic admittance (black) and synthetic coherence (dark blue) with corresponding MCMC-derived best-fit admittance (red) and best-fit coherence (cyan). Twenty iterations of synthetic and corresponding best-fit spectra are plotted together for an indication of how variable the synthetic cases can be when perturbed by noise. a) Synthetic spectra based on an elastic thickness of 14.8 km and loading fraction of 0.644 (the best-fit solutions for real-world data at -15°N and 180°E). The mean best-fit elastic thickness is 15.3 km with a standard deviation of 0.21km. The mean best-fit loading fraction is 0.620 with a standard deviation of 0.001. b) Synthetic spectra based on an elastic thickness of 32.3 km and loading fraction of 0.289 (the best-fit solutions for real-world data at 45°N and 45°E). The mean best-fit elastic thickness is 30.8 km with a standard deviation of 2.7 km. The mean best-fit loading fraction is 0.289 with a standard deviation of 0.021.

For the 13 synthetic tests we performed, the standard deviation in best-fit elastic thickness and loading fraction values increases as the combined RMS value (from the inversion of the real data) increases (Figure 2.4). This is unsurprising, given that examples with higher RMS values tend to have lower coherence spectra, which necessarily increases the noise (equation 21). In both elastic thickness and loading fraction, a clear jump can be seen in the standard deviations from these noise-added tests at a combined RMS value of approximately 0.4. Below this value, the standard deviations in elastic thickness from the noise-added tests are generally within a factor of two of the standard deviation provided by the MCMC inversion (Appendix Figure B1). This result suggests that the MCMC uncertainties can in fact provide a reasonable assessment of the actual uncertainties, given that the fits to the spectra are reasonable. We therefore use the standard deviations from the MCMC inversions as a measure of uncertainty, but only in locations where the sum of admittance RMS and coherence RMS has a value of 0.4 or lower. Areas with combined RMS values above this cutoff are deemed unreliable, and we do not consider the results at these locations further.

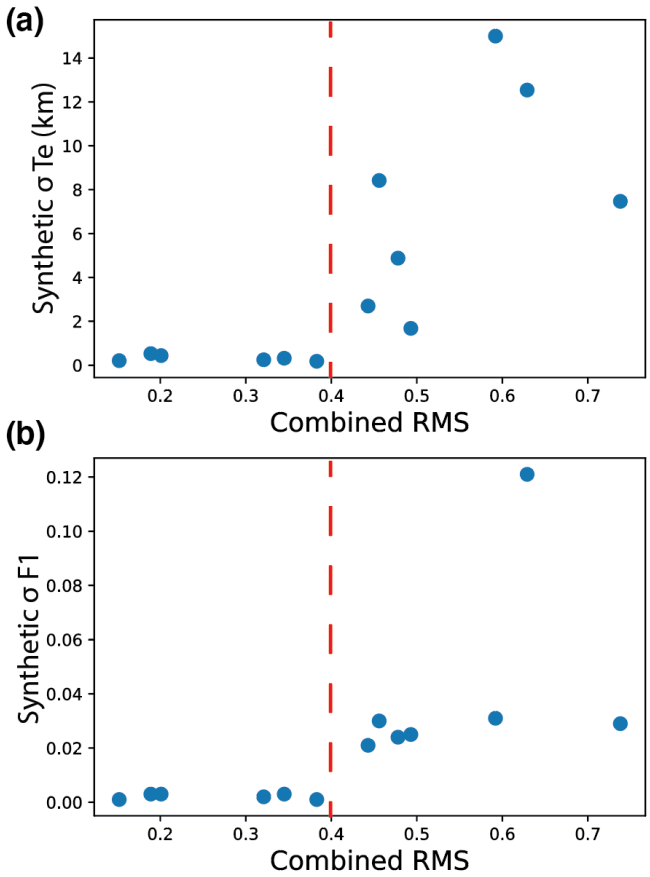

Figure 2.4: a) One standard deviation in the best-fit elastic thickness values from synthetic noise-added spectra compared with the combined root mean square (RMS) values for admittance and coherence fits (from fits to observations). b) Same as in (a) but for loading fraction. The red dashed line denotes a sharp increase in the synthetic-derived standard deviations at a combined RMS value of 0.4.

3 Results

We map the variations in elastic thickness and loading fraction across the globe (Figure 2.5a and 2.5b, respectively) and report only the results that produced a combined RMS of less than 0.4 (Figure 2.5d). Notably, areas that have combined RMS values >0.4 are in the same regions where the mean correlation (between $l = 20$ and $l = 30$; Figure 5c) is less than ~0. Such areas imply the presence of extensive mare volcanism. However,

there are some results below the cutoff value that are in mare regions, which we discuss in the next section.

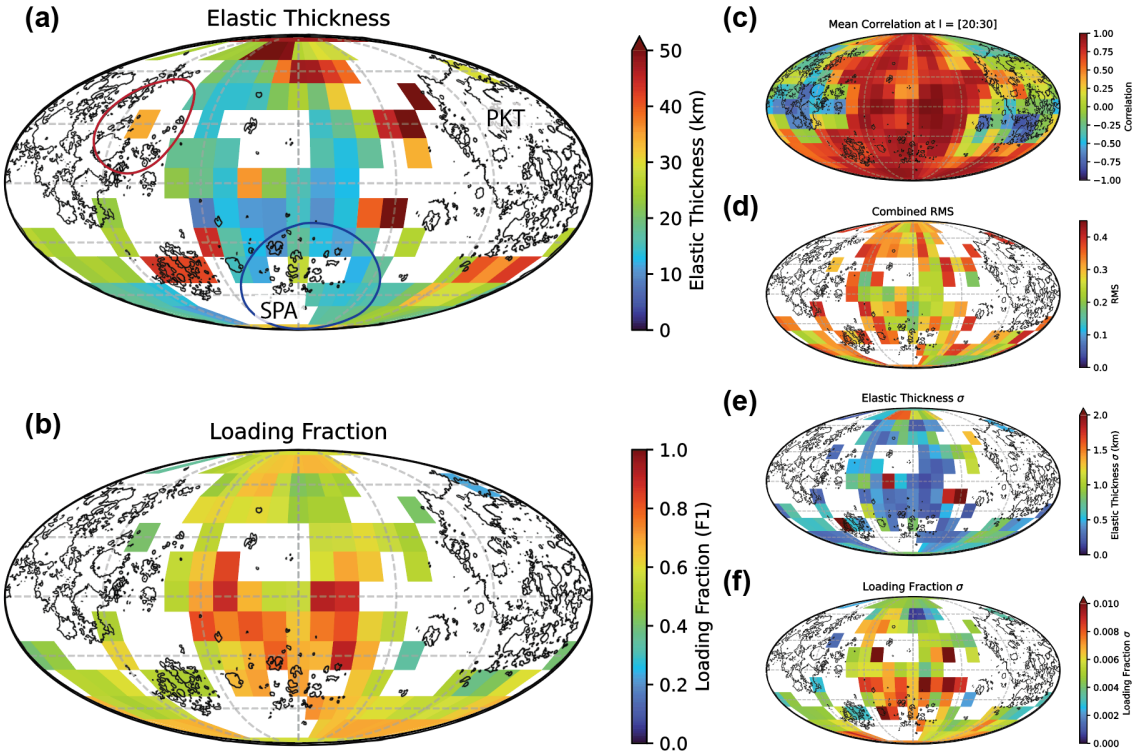

Figure 2.5: Best-fit results from MCMC inversions of admittance and coherence spectra. Values are on a grid of 15° spacing. Shown here are a) best-fit elastic thickness values, b) best-fit loading fraction values, c) mean correlation from l = 20 to 30, d) combined RMS values (RMS of the admittance fit plus RMS of the coherence fit), e) standard deviations in elastic thickness, and f) standard deviations in loading fraction. All except panel c) are masked to show results only with RMS values <0.4 (see text). The red outline in (a) represents the extent of the spherical cap used for localized analyses (25° radius). The blue outline in (a) shows the extent of the South Pole-Aitken (SPA) basin. SPA and the Procellarum KREEP Terrane (PKT) are labeled.

Best-fit elastic thickness values range from 9 km to 60 km. The mean elastic thickness value across all regions is 28.4 km, and the standard deviation is 12.9 km. Standard deviations in elastic thickness from the MCMC approach for an individual region are typically on the order of a kilometer, though a few locations have standard

deviations up to 2.4 km. The highest loading fraction values are centered on the farside, around the northern edge of South Pole-Aitken (SPA) basin, where elastic thickness tends to be low. A summary of our results with a combined RMS below the cutoff value of 0.4 can be found in Table B1 in Appendix B.

Examples of best-fit results from two MCMC inversions can be seen in Figure 2.2. The first result (Figure 2.2a) is the best-fit modeled admittance and coherence for the observations at -15°N, 180°E. The best-fit T_e is 14.8 ± 0.38 km, the best-fit F_1 is 0.644 ± 0.007, and the combined RMS value is 0.152. This location is in the lunar highlands on the farside of the Moon, which is an ideal location for a localized admittance analysis. The observed admittance and coherence are well-modeled by the best-fit parameters with low standard deviations (Figure 2.2b). Also shown is the best-fit modeled admittance and coherence for the observations at 45°N, 45°E (Figure 2c), which has a best-fit T_e of 32.4 ± 0.05 km, F_1 of 0.289 ± 0.001. This location contains mare infill, which violates the two-layer model we used to calculate the best-fit elastic thickness. Its combined RMS is 0.443, which is above the acceptable bound and thus, we do not consider this result to be reliable (despite the apparently small error bars).

4 Discussion

Based on our error analysis, the variations in elastic thickness we find (Fig 2.5a) are real, and may be compared with other observed spatial patterns, as discussed in more detail below (Section 4.3). We focus on the farside because the abundance of nearside

mascons renders the admittance approach ineffective there. Example admittance profiles are shown in Figure 2.6.

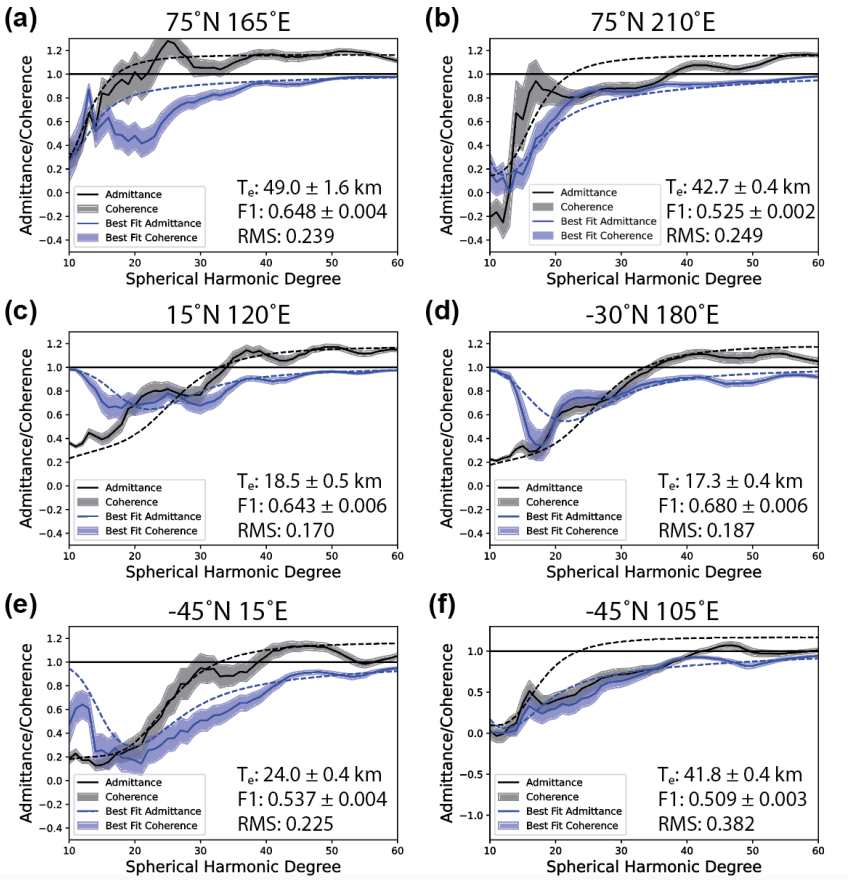

Figure 2.6: Select examples of observed admittance and coherence (thick black and blue lines, respectively) with the best-fit model admittance and coherence (dashed lines). a) Example fit for the northern high T_e values, centered on 75°N and 165°E. b) Example fit for the northern high T_e values, centered on 60°N and 210°E. c) Example fit for the equatorial low T_e values, centered on 15°N and 120°E. d) Example fit for the SPA low T_e values, centered on -30°N and 180°E. e) Example fit for the moderate T_e values, centered on -45°N and 15°E. f) Example fit for the high T_e values affected by mare volcanism, centered on -45°N and 105°E.

The northern hemisphere has relatively higher elastic thickness values (>20 km) with a few regions with even higher elastic thicknesses. The high (>40km) values to the west of the Procellarum KREEP Terrane (PKT) have a combined RMS close to the cutoff

(Fig 2.5d) and are likely spurious, the result of inclusion of regions of mare volcanism. However, the high values between 90°N and 60°N cannot be explained by mare volcanism and thus indicate a real increase in elastic thickness (Fig 2.6a and 2.6b). The mean elastic thickness value for the regions at 60°N or higher is 40.9 km, with a standard deviation of 11.3 km.

In general, the equatorial region of the farside (north of SPA) has relatively low elastic thickness values (<20 km, Fig 2.6c). One location, 0°N, 150°E, has an anomalously high elastic thickness (35.7 ± 1.9 km) despite the apparent lack of nearby maria; other areas (e.g., -15°N, 240°E) are likely contaminated by mare deposits (in this case, Orientale).

The SPA region is similar, with low elastic thicknesses (<20km) both inside and outside of SPA (Figure 2.6d). One location within SPA, -45°N, 180°E, has an anomalously high elastic thickness (27.4 ± 0.8 km). This area is in the center of the mare within SPA, suggesting that the admittance estimates may have been affected by mare volcanism.

The areas to the east and west of SPA are characterized by moderate elastic thickness values (15 km < T_e < 30 km, Fig 2.6e). Notably, the lower elastic thickness values are found close to SPA, and elastic thickness generally increases with distance from the basin. There are a few areas of high elastic thickness (> 40 km, Fig 2.6f) in the southern hemisphere, but these are characterized by RMS values near the cutoff and are all in areas that include mare volcanism (e.g., Mare Australe, Mare Humorum, Mare

Nubium, and Orientale). We conclude that admittance estimates in these areas have likewise been contaminated by mare volcanism.

Figures 2.5a and 2.5b show that there is an inverse correlation between loading fraction and elastic thickness. Thus, for instance, the region of low elastic thickness within SPA is also characterized by high loading fractions (F_1~0.8).

4.1 Comparisons with Previous Work

Our lower elastic thickness results are slightly lower than obtained by Arkani-Hamed (1998) and Sugano and Heki (2004), but otherwise the majority of our results agree well with their ranges of 20 km < T_e < 50 km (Arkani-Hamed, 1998) and 20 < T_e < 60 km (Sugano and Heki, 2004).

Crosby and McKenzie (2005) evaluated the elastic thicknesses of rectangular regions in the southern highlands (centered on Clavius crater) and north of Mare Imbrium. For Clavius crater, Crosby and McKenzie found a range of best-fit elastic thickness values depending on whether the area was modeled as an elastic plate or thin shell. Our results for the region surrounding Clavius crater suggest a broad area of variable elastic thickness, with some areas having high elastic thickness values (>40 km, which may be due to contributions from Mare Nubium). However, our results at -60°N, 330°E, approximately the center of the region analyzed by Crosby and McKenzie (2005), indicate an elastic thickness of 24.9 ± 0.8 km and a loading fraction of 0.636 ± 0.005, which agrees with their results when modeling the area as an elastic plate: T_e = 20 ± 8 km and $F1$ = 0.5 ± 0.1. However, it does not agree with the results of Zhong et al. (2019a),

who found a best-fit elastic thickness of 7 km (uncertainties not provided) and a loading fraction of -0.194 (uncertainties not provided), which in their notation indicates primarily surface loading. Zhong et al. (2019a) use a much smaller area when calculating the admittance and coherence spectra (θ= 5°), focusing on the crater itself, and thus are more limited in the range of spherical harmonic degrees they can model (l = 56 to 149). Based on our analysis, it appears that the small window size used causes the elastic thickness to be underestimated (see Appendix Figure B2).

For the region north of Imbrium, Crosby and McKenzie again find variable elastic thicknesses, depending on the method of modeling. For an elastic plate, they find that elastic thickness must be >80 km. Our closest result with an acceptable RMS cutoff value is at 60°N, 345°E, where we find a best-fit elastic thickness of 29.3 ± 0.8 km and a loading fraction of 0.636 ± 0.005. However, our fit is rather poor (combined RMS of 0.394), so the apparent disagreement may simply be indicating that the admittance technique is not reliable here.

Satya Kumar et al. (2018) use the Maximum Entropy Method to investigate the elastic thickness around the farside basins Hertzsprung, Dirichlet-Jackson, and Korolev. Their region spans a rectangular area from -15°N to 45°N and 180°E to 255°E. They find a best-fit elastic thickness of 19 km (uncertainties not provided). This region is also analyzed by Huang and Wieczorek (2012), who found an elastic thickness of 19 km (lower bound of 0 km and an upper bound of infinity) with subsurface loading at 20°N, 230°E (and 63 km if all surface loading, with a lower bound of 16 km and an upper bound of infinity), and Zhong et al. (2014), who found an elastic thickness of 14.53 km at

19°N, 240°E (uncertainties not provided). Our results are in approximate agreement with all of these papers, with elastic thicknesses of 15.3 ± 0.4 km at 15°N, 240°E and 17.6 ± 0.3 km at 15°N, 225°E.

Huang and Wieczorek (2012) determine best-fit bulk density, elastic thickness, and porosity in areas only where gravity and topography are very well correlated. This allows them to analyze nine locations if they include subsurface loads or 26 locations if they assume surface loading only. They find a range of elastic thickness values between 5 km and 63 km, though their uncertainties are sometimes unconstrained – occasionally the upper bound is infinity and the lower bound is 0 km. Because their localized areas are rather small (θ= 12° or 20°, compared with our 25°) and the spectral bandwidth they use is quite large (L_{win} = 21 or 13, compared with our 10) their admittance spectra lack information at large wavelengths. Additionally, they model only the degrees where correlation is close to one and thus the range of spherical harmonic degrees they evaluate is limited to high degrees (e.g., l = 32 to 60 for region 7 in their Table 1) where differences in admittance at higher elastic thicknesses are minimal (Figure 2.1). This may lead to underestimated best-fit elastic thickness values (Appendix Figure B2), and indeed, many of the locations they test (18 of 26) have lower best-fit elastic thicknesses than our closest analog. Another possible explanation for the differences in our results is that our wider localized areas occasionally necessarily overlap multiple geologic terranes (e.g., -30°N, 120°E, which includes mare volcanism, SPA ejecta, and a portion of the SPA basin).

Zhong et al. (2014) also investigate lunar elastic thickness in certain regions under the assumption that the lithosphere can be modeled as a thin elastic spherical shell. They use admittance and coherence to estimate elastic thickness and loading fraction, as well as crustal thickness, load depth, and crustal density. As with Huang and Wieczorek (2012), the localized areas they use to calculate admittance and coherence spectra are smaller than the regions we use (θ= 10°, compared with our 25°), and as a result they exclude the long-wavelength admittance data ($L_{win} = l_{min} = 26$), which may lead to underestimated elastic thickness values (Appendix Figure B2). Though they provide information about the misfit of their best-fit values in figures (e.g., their Figure 2), they do not report a range of acceptable misfit, and thus do not provide uncertainties for their results. There is little correlation between their elastic thickness estimates and ours. The areas where our results do agree tend to have low to moderate elastic thickness values (10 km < T_e < 24 km).

Finally, we compare our results with those from Audet (2014). Areas where our results indicate high elastic thickness (>40 km) have higher values than those from Audet (2014), though these are the frequently areas we noted above, where the RMS values are close to the cutoff and mare deposits influence the admittance and coherence spectra. Our best-fit loading fraction results generally agree with those from Audet (2014) (though here we note that we use a different notation and thus our loading fraction is inversely proportional to his), with the region north of SPA having the highest amounts of surface loading, and the surrounding areas having higher amounts of subsurface loading. Our

uncertainties in elastic thickness and loading fraction are systematically lower than those in Audet (2014), which we discuss in the next section.

4.2 Magnitude of Uncertainties

On the basis of our synthetic testing (Section 2.4) we argued that the MCMC-derived uncertainties are a realistic representation of the true uncertainties only for cases when the combined RMS<0.4. However, the actual uncertainties we find (of order 1 km for elastic thickness) are small compared with previously published estimates.

We think that there are several possible reasons for this discrepancy. First, in some cases the uncertainties are estimated in fundamentally different ways. For instance, Crosby and McKenzie use a cutoff of 0.3 from their misfit function (inferred from their Figure 2) but do not justify this cutoff in statistical terms. Second, we are fitting only two parameters (T_e and F_l), which will automatically result in lower uncertainties than for other works where more parameters are fitted (e.g., Huang and Wieczorek, 2012). Third, we require our best-fit models to fit both admittance and coherence, while many other papers require their models to fit admittance only (e.g., Crosby and McKenzie, 2005; Huang and Wieczorek, 2012; Zhong et al., 2014). Fourth, our localized areas are larger than those in Huang and Wieczorek (2012), Zhong et al. (2014; 2019a; 2019b), and Audet (2014), and thus we fit a different (and often wider range) of spherical harmonic degrees. Fitting both admittance and coherence – and fitting them to a wider range of degrees – will tend to decrease the uncertainties.

4.3 Correlation with Geologic Trends

In general, our results do not correlate with many geologic trends, such as crustal density, crustal thickness, or mean elevation. Figure 2.7a shows moderate correlations between elastic thickness and loading fraction (as expected, given their tradeoff relationship). Figures 2.7b and 2.7c show that the lowest crater densities tend to be associated with high elastic thicknesses (and low loading fractions). However, given that two of the four lowest points have RMS values very close to the cutoff value of 0.4, we do not view this result as significant. Crater densities were calculated using craters >20 km (Head et al., 2010) in regions of our spherical cap (θ=25°). There are no obvious correlations with either crustal thickness (Figs 2.7d, 2.7e) or density (Figs 2.7f, 2.7g), values from Wieczorek et al. (2013).

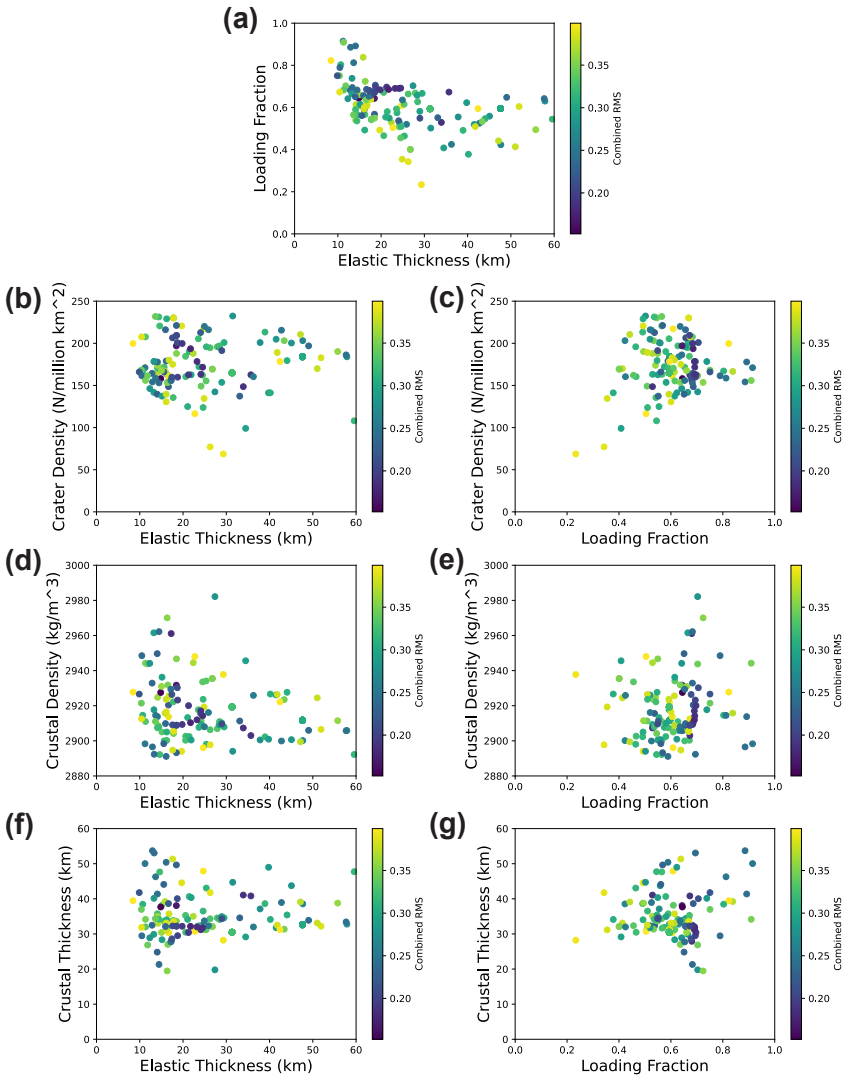

Figure 2.7: Scatter plots of elastic thickness and loading fraction versus crater density (b-c), crustal density (d-e), and crustal thickness (f-g). Results are color-coded by their Combined RMS values. Crater densities are calculated using craters >20 km (Head et al., 2010) in each localized area. Crustal density and crustal thickness values are from Wiecorek et al. (2013), averaged over each localized area.

4.4 Implied Heat Flux

The elastic thicknesses reported here are the elastic thicknesses at the time of load emplacement. We can therefore make a crude estimate of the heat flux associated with these time periods using the heat flux equation $F = k\,\Delta T/T_e$ where F is the heat flux, k the

thermal conductivity, and ΔT the temperature contrast between the surface and the base of the elastic layer. On Earth, the elastic thickness of oceanic lithosphere is defined by the depth to the 300 – 600 °C isotherms, based on a cooling plate model (Watts et al., 2012). The mean surface temperature of the Moon is approximately 250 K, but 4 Gyr ago when the Sun was 30% fainter it would have closer to 230 K. If we use the latter value and a thermal conductivity of 2 W m^{-1} K^{-1} (as in Maurice et al., 2020), then a 20 km elastic thickness implies a heat flux of 34-64 mW m^{-2} and a 40 km elastic thickness implies a heat flux of 17-32 mW m^{-2}.

For the farside equatorial and SPA regions where T_e<20 km, the implied heat flux of >34 mW m^{-2} is quite high. In the preferred model of Laneuville et al. (2013), such a high farside heat flux would only arise during the first 200 Myr after lunar magma ocean (LMO) solidification. Likewise, Kamata et al. (2015) have shown that a high inferred heat flux (T_e = 20 km) would have only persisted for <200 Myr after the LMO solidified. Conversely, the northern polar regions with $T_e \approx$ 40 km could be recording events as late as 3.5 Ga. Large areas of the farside thus experienced the last loading event early (<200 Myr) in after LMO solidification, but elsewhere geological activity may have been more prolonged.

5 Conclusions

We find that elastic thickness (at the time of loading) varies across the Moon between 9 km and 60 km with a mean elastic thickness of about 30 km. The highest reliable elastic thicknesses can be found north of 60°N while the lowest elastic

thicknesses can be found in the equatorial farside and within SPA. Our results can be split into four broad categories: 1) the low elastic thickness values in the equatorial farside, 2) the low elastic thickness values in and around SPA, 3) the moderate elastic thickness values to the east and west of SPA, and 4) the moderate to high elastic thickness values in the northern farside. We find no correlation between elastic thickness and crater density, crustal density, or crustal thickness in areas where reliable estimates of elastic thickness can be made.

The low elastic thickness values that we find (<20 km) imply heat fluxes in excess of 34 mWm^{-2}. These values suggest that much of the loading on the Moon must have taken place within the first ~200 Myr after LMO solidification, though some areas (T_e>40 km) may be recording events as late at 3.5 Ga.

We also demonstrate that smaller localization windows can lead to lower elastic thickness estimates (Appendix Figure B2), which may explain some of the differences between this work and previous work. We caution future workers that utilizing windows that do not fully capture longer wavelength information may bias their elastic thickness estimates.

Chapter 3: Martian Paleopole Locations from Crustal Magnetic Anomaly Analysis

Abstract

We analyze 10 martian crustal magnetic anomalies to determine the magnetic paleopole locations at the time the anomalies were magnetized using Parker's method (Parker, 1991). We use an updated method of estimating paleopole location uncertainty and perform this analysis on multiple datasets to ensure accurate results. We use the Maximum Angle of Dispersion (MAD) developed by Kirschvink (1980) to state the dispersion of our paleopole results. Our results imply at least one cluster of paleopole locations (at approximately 45°N, 0°E), suggesting either the dipolar axis was stable for an extended period or that some of the anomalies we analyze were magnetized contemporaneously. This cluster of paleopole locations correlates with the paleo-spin axis calculated by Perron et al. (2007) using the paleo-shorelines of the Arabia shoreline. This supports the true polar wander history put forth by Perron et al. but does not necessarily rule out other true polar wander histories, as we cannot confirm the timing of the polar wander. We rule out multipolar fields and a hemispherical dynamo as explanations for the wide spread of paleopole locations, though the numerous paleopoles that do not correspond to the current or ancient spin-axes are still unexplained.

1 Introduction

Though Mars currently lacks a global, dynamo-generated magnetic field, spacecraft measurements (e.g., Acuña et al., 1999) have found evidence of widespread crustal magnetism. These crustal magnetic anomalies contain information about the ancient fields that existed at the time of magnetization. Careful analysis of these anomalies can elucidate the thermal evolution of Mars, such as when the dynamo was active and how strong it was. Crustal magnetic analyses can also be used to constrain the path of true polar wander, given that in most dynamos we see, the dipolar magnetic field axis is generally aligned with a planet's spin axis (e.g., Mercury, Earth, Jupiter, and Saturn).

True polar wander on Mars has been studied extensively through analysis of the fossil bulge (Matsuyama and Manga, 2010; Bouley et al., 2016) and analysis of paleo-shorlines (Perron et al., 2007; Chan et al., 2018). However, these analyses provide conflicting results. Fossil bulge analyses (Matsuyama and Manga, 2010; Bouley et al., 2016) find a paleopole of 71°N, 259.5°E. This implies a small amount of true polar wander (<20°) as a result of the formation of the Tharsis volcanic complex near the equator.

Analyses of paleo-shorelines find a wider range of possible paleopoles, with paleopoles at 40°N, 334°E; 79°N, 337°E (Perron et al., 2007); and 75°N, 327°E (Chan et al., 2018). These paleopole locations lie on a great circle 90° away from the paleopole found by fossil bulge analyses, which imply that these true polar wander events occurred after the formation of Tharsis and consistent with the requirement that Tharsis remain at the equator.

The analysis of crustal magnetic anomalies offers an alternative method of determining the ancient spin axis of Mars and could distinguish between the proposed polar wander histories. Many authors have previously performed analyses on crustal magnetic anomalies in order to determine their magnetization directions and paleopole locations (Sprenke and Baker, 2000; Arkani-Hamed, 2001; Hood and Zakaraian, 2001; Richmond and Hood, 2003; Frawley and Taylor, 2004; Arkani-Hamed and Boutin, 2004; Hood et al., 2005; Boutin and Arkani-Hamed, 2006; Hood et al., 2007; Langlais and Purucker, 2007; Quesnel et al., 2007; Hood et al., 2010; Milbury et al., 2012; Plattner and Simons, 2015; and Thomas et al., 2018). As shown in Figure 3.1, despite good agreement between many analyses of individual anomalies, there is very little consensus on the location of any ancient magnetic poles, suggesting a complex magnetic history.

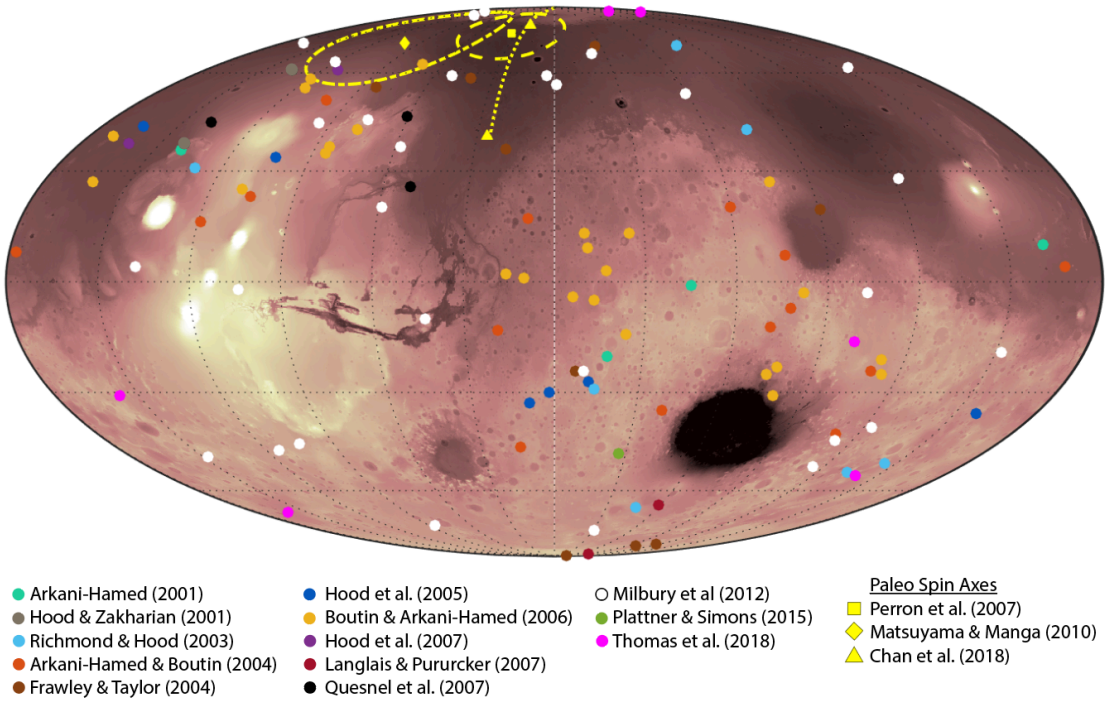

Figure 3.1: Compilation of published paleomagnetic pole locations plotted over Mars Orbiter Laser Altimeter (MOLA) data (Smith et al., 2001) in a mollweide projection

centered on 0°N 0°E. All paleopoles have been converted to south poles. Paleo-spin axes from Perron et al. (2007), Matsuyama and Manga (2010), and Chan et al. (2016) have been included in yellow: the dotted line corresponds to the axis of rotation described in Perron et al. (2007), the dash-dotted ellipse corresponds to the uncertainty from Matsuyama and Manga (2010), and the dashed ellipse corresponds to the uncertainty from Chan et al. (2018).

Several authors claim to have found evidence for true polar wander based on paleopoles that are not aligned with the current spin axis (Arkani-Hamed, 2001; Hood and Zakharian, 2001; Arkani-Hamed and Boutin, 2004; Frawley and Taylor, 2004; Hood et al., 2005; Boutin and Arkani-Hamed, 2006; Langlais and Purucker, 2006; Hood et al., 2007; Quesnel et al., 2007; Milbury et al., 2012; Thomas et al., 2018). Many authors (Arkani-Hamed, 2001; Arkani-Hamed and Boutin, 2004; Frawley and Taylor, 2004; Boutin and Arkani-Hamed, 2006; Milbury et al., 2012; Thomas et al., 2018) also argue for at least one polar reversal event to account for antipodal paleopoles. However, a majority of the paleopoles found from magnetic analyses do not correlate with the paleo-spin poles found from analyses of the fossil bulge (Matsuama and Manga, 2010; Bouley et al., 2016) and paleo-shorelines (Perron et al., 2007; Chan et al., 2018), nor has there been an attempt to state the statistical significance of any of the common paleopoles found from magnetic analyses.

The number of anomalies available for study is limited, given that most martian crustal magnetic anomalies are not perfectly isolated (i.e., there are other, potentially unrelated crustal magnetic anomalies in the vicinity). To determine the paleopole from crustal magnetic anomalies, one must assume the anomaly is unidirectionally magnetized (i.e., has only one magnetization direction). Inclusion of unrelated anomalies could break

the assumption of undirectionality and could make any recovered magnetization directions meaningless.

Some work has been done to quantify both how isolated an anomaly needs to be and how much "noise" (uncorrelated anomalies) may be in the system. Thomas et al. (2018) show that anomalies ought to be separated from other anomalies by at least twice the radius of the anomaly of interest. Maxwell and Garrick-Bethell (2020) show that Signal-to-Noise Ratios (SNR) greater than 5 are required to determine the magnetization direction of an anomaly within reasonable uncertainties. They also show it is possible to obtain accurate magnetization directions of anomalies with SNRs <5, albeit with increased uncertainty. To mitigate the negative effects of low SNR values and validate our results, we perform analyses on each component (east, north, and radial) of multiple datasets, including recent MAVEN magnetometer data (Connerney et al., 2015).

This paper improves upon previous work in several ways. It follows Thomas et al. (2018) in using Parker's method (Parker, 1991), a state-of-the-art inversion method capable of determining the magnetization direction of an anomaly without making assumptions about the anomaly's source geometry. We also use an updated method of estimating directional uncertainty from Maxwell and Garrick-Bethell (2020), which allows for more robust determinations of paleopole locations. We perform these inversions on multiple datasets: the Morschhauser et al. (2014) spherical harmonic model (also analyzed in Thomas et al., 2018), the Langlais et al. (2019) spherical harmonic model, and the MAVEN-MAG dataset (Connerney et al., 2015). In this paper, we make extensive use of MAVEN data to confirm the topology of magnetic fields from the

spherical harmonic models and to verify the paleopole locations recovered using spherical harmonic models (e.g., Morschhauser et al., 2014; Langlais et al., 2019).

This work also improves upon previous work by explicitly quantifying the degree of clustering of paleopoles with error ellipses. We use the Maximum Angle Dispersion (MAD) method (Kirschvink, 1980) to determine how tightly clustered paleopoles are and we compare our results to what would be expected from random locations of uncertainty ellipses. Our results imply a complex history of the martian dynamo.

2 Data

This analysis makes use of three datasets: two spherical harmonic models of the crustal field by Morschhauser et al. (2014) and Langlais et al. (2019), and calibrated tracks of MAVEN magnetometer data (Connerney et al., 2015). Here we describe each dataset in detail. When performing our uncertainty analyses (described in the Section 3), we use only the Langlais dataset, as it is the most recent spherical harmonic model. Given the varying altitude of MAVEN tracks, as well as daily and seasonal variations in field strengths, we are unable to calculate a constant SNR for MAVEN data, which is required for estimating uncertainty with the method proposed by Maxwell and Garrick-Bethell (2020).

The Morschhauser et al. (2014) dataset is a spherical harmonic model of the crustal field to degree and order 110 based on an L1 normalization fit to Mars Global Surveyor (MGS) magnetometer data from the beginning to the end of its operation (1997 – 2006). From here on, we will refer to this model as SH-M14. We expand the model

onto a regular grid with data points every 1.33° at 120 km altitude. This resolution is lower than the model's resolution (~0.8° spacing), but we have found that higher resolution maps do not produce better fit results (Appendix Figure C1) and are sometimes detrimental to efforts to determine the magnetization direction because of the inclusion of small scale "noise" (i.e., smaller, uncorrelated anomalies). Our choice of data resolution corresponds to half the resolution of the Langlais et al. (2019) dataset.

The Langlais et al. (2019) dataset is a spherical harmonic model of the crustal field to degree and order 134, where they model the data with an Equivalent Source Dipole approach using MGS magnetometer and Electron Reflectometer data from 1997 to 2006 and MAVEN magnetometer data from 2014 (beginning of operation) to 2019. From here on, we will refer to this model as SH-L19. As with the SH-M14 model, we expand the model onto a regular grid with data points every 1.33° at 120 km altitude. While this resolution is lower than the model's resolution (0.66° spacing), we show in Appendix C that our expansion is appropriate.

The MAVEN dataset consists of calibrated MAVEN-MAG tracks from the beginning of the mission (2014) to today. These data are available from the NASA PDS (Connerney et al., 2015). We limit the tracks we use to only data that were taken between 7 p.m. and 5 a.m. local time (e.g., on the opposite side of Mars from the sun) in order to avoid effects from the interplanetary magnetic field. We also only use tracks below 200 km altitude to better ensure variations in field strength are from the crustal fields rather than the interplanetary magnetic field. For some anomalies we analyze, coverage is good enough that we are able to use only data below 150 km or 170 km. No effort is put into

averaging or down sampling the available data, though we do manually remove a few spurious data tracks when it is clear the tracks do not match the majority of the data. These spurious tracks within our chosen range for each anomaly are listed in the Appendix (Appendix Table C1). We accept variations between tracks, given that our inversions that fit these data will necessarily average out any daily or seasonal variations.

3 Methods

To model the crustal magnetic fields, we use a common inversion method developed by Parker (1991), hereafter referred to as Parker's method. Though initially used to analyze magnetized seamounts on Earth (Parker, 1991), this method has also been used on the Moon (Oliveira and Wieczorek, 2017; Lee et al. 2019; Maxwell and Garrick-Bethell, 2020), Mercury (Oliveira and Wieczorek, 2019), and Mars (Thomas et al., 2018).

Parker's method places model dipoles on a regular grid, within a specified area on a surface above the source body, to obtain the best-fitting magnetization distribution for a particular magnetization direction. It makes no assumption about the geometry of the magnetic source body but does follow the unidirectional assumption that all model dipoles have the same magnetization direction, while allowing for variable magnetization strength across an anomaly. Each possible direction is tested (a unit sphere equally spaced by ~2°) and the lowest root mean square (RMS) between the observations and the model is taken to be the best-fit direction. We will describe the uncertainty later in this section. Formally, this method models magnetization within some volume V as a

unidirectional magnetic field whose magnetization strength is an arbitrary function of position within the body, modeled on the surface of V. The magnetization is written as

$$\boldsymbol{M}(\boldsymbol{s}) = \widehat{\boldsymbol{m}}\, m(\boldsymbol{s}), m(\boldsymbol{s}) \geq 0.$$

where $\widehat{\boldsymbol{m}}$ is the direction of magnetization and $m(\boldsymbol{s})$ is the strength of the model dipole at location $\boldsymbol{s}$. Observations taken outside of V are approximated as the field component along $\widehat{\boldsymbol{B}}_0$, the direction of the main magnetic field in the vicinity. In this work, we test each component of the magnetic field (east, north, and radial) separately as a method of validating the results.

From Parker et al. (1987), N_o observations d_j made at positions $\boldsymbol{r}_j$ can be calculated as the sum of contributions from N_d dipoles located at $\boldsymbol{s}_i$

$$d_j = \sum_{i=1}^{N_d} g_j(\boldsymbol{s}_i) m(\boldsymbol{s}_i)\,, j = 1, \ldots, N_o$$

where the contribution from a single dipole at location i is given as

$$g_j(\boldsymbol{s}) = \frac{\mu_0}{4\pi}\left[\frac{3\widehat{\boldsymbol{m}} \cdot (\boldsymbol{r_j} - \boldsymbol{s})\widehat{\boldsymbol{B}}_0 \cdot (\boldsymbol{r_j} - \boldsymbol{s})}{|\boldsymbol{r_j} - \boldsymbol{s}|^5} - \frac{\widehat{\boldsymbol{m}} \cdot \widehat{\boldsymbol{B}}_0}{|\boldsymbol{r_j} - \boldsymbol{s}|^3}\right]$$

From this, we can use the matrix G, which depends on the dipole locations $i = 1, \ldots, N_d$ and observation locations $j = 1, \ldots, N_o$, to find the magnetization strength of the source dipoles by solving the non-negative least squares technique as developed by (Lawson and Hanson, 1974)

$$\min_{m \geq 0} \|\boldsymbol{d} - G\boldsymbol{m}\|^2$$

Note that the user must choose a model dipole spacing resolution and their spatial coverage. For this work, we choose a dipole spacing of 1°, which allows for more dipoles

than observations (data spacing is 1.33°). The dipoles are equally spaced using the polar coordinate subdivision method (Katanforoush and Shahshahani, 2003). Choosing a finer spacing of model dipoles does not improve the best-fit direction from Parker's method (Appendix Figure C1b).

We choose the extent of data to encompass a spherical cap (e.g., a circular dataset), with the radius of the observations (r_o) set larger than the radius of model dipoles (r_d) to avoid unwanted edge effects. The extents vary for each location we test (Table 3.1). We make an effort to improve the Signal-to-Noise Ratio (SNR) of the data by choosing observation and model dipole radii to exclude nearby magnetic anomalies from the inversion. SNR is calculated as the maximum field strength within the observation extent divided by the mean of the absolute value of the data between the observation radius and the model dipole radius.

These inversions are performed on all components (east, north, radial) for the SH-M14, SH-L19, and MAVEN datasets for a total of nine inversions per anomaly. For each component, if the inversions from the three datasets do not match, we discontinue the anomaly. This is better quantified by our uncertainty estimation method, and we expand upon our choice of anomalies later in this section.

There are two accepted methods of citing uncertainty for a recovered magnetization direction. The first, from Parker (1991), is to calculate the RMS of the difference between the model and the observations for each direction tested and accept all directions with an RMS lower than the mean background field strength (i.e., the mean of the field interior to r_o and exterior to r_d). This method has two major risks, as discussed

by Oliveira and Wieczorek (2017) and Maxwell and Garrick-Bethell (2020). The first is that the mean background field might be smaller than the RMS of the difference between the model and observed fields, resulting in an uncertainty of exactly zero. The second risk is that the anomaly's field strength might be comparable to the background field strength (i.e., a low SNR), resulting in a wide range of acceptable directions, sometimes on the order of a hemisphere, as in Oliveira et al. (2019). Maxwell and Garrick-Bethell (2020) show that such large uncertainties are overly conservative and unfairly biased against high inclinations. They demonstrate an alternative method of estimating uncertainty that both produces a more robust estimate and removes this inclination bias.

The second method of estimating the directional uncertainty, and the one used herein, is to use a Monte Carlo method of simulating the background field, as proposed by Maxwell and Garrick-Bethell (2020). They create twenty realizations of synthetic "noise" on the order of the observed background field (with in ± 0.5 SNR units) and add the best-fit model of the anomaly to these realizations of noise. They then perform Parker's method inversions on each of these synthetic datasets and determine the standard deviation *s* of the recovered directions. This standard deviation is then taken to be the uncertainty as it describes how easily perturbed the best-fit direction is in the presence of a background field. They use this standard deviation to calculate an uncertainty ellipse (Butler, 1992), and note that their ellipses indicate one standard deviation rather than a 95% confidence interval. The axes of such an ellipse are calculated as

$$dp = s\left(\frac{1 + 3cos^2 p}{2}\right)$$

$$dm = s\left(\frac{\sin p}{\cos I}\right)$$

where *dp* is the axis along the site-to-pole great circle, *dm* is the axis perpendicular to *dp*, *I* is inclination, and *p* is calculated as

$$p = \cot^{-1}\frac{\tan I}{2}$$

This uncertainty can also be quantified using the precision parameter *k*, calculated as

$$k = \frac{N-1}{N-R}$$

where *N* is the number of iterations (here, 20) and *R* is the length of the sum of all best-fit magnetization direction unit vectors. High *k* values imply high precision estimates.

Maxwell and Garrick-Bethell (2020) do this for only the best component (i.e., the component with the lowest SNR) given that results should not vary between components. However, we have found that a few of the anomalies we analyzed look reasonable (i.e., well isolated with low noise) in one component, but not in the other components. Alternatively, sometimes the SNR in two components are equal to each other, yet the recovered magnetization directions are slightly different. To ensure a fair analysis of each anomaly, we perform the uncertainty estimation method on all components of the SH-L19 dataset. If the results completely disagree across components (i.e., none of the uncertainty ellipses overlap), we discontinue analysis of that anomaly. Additionally, if neither of the inversion results using SH-M14 and MAVEN do not agree with SH-L19 within the calculated uncertainty for a given component, we discontinue the anomaly.

In Figure 3.2, we show two examples of this method of removing anomalies from analysis. One anomaly (A1) appears to be well-suited for analysis as it is isolated and has a high SNR, but the results across components and datasets do not agree. The other anomaly (A3) is less well-isolated and has a lower SNR, but its paleopole locations agree in each component and dataset. A1 is an anomaly we analyzed but do not keep in this work, given that its results do not agree within the calculated uncertainties, and we are unable to determine which component and dataset is most accurate. A3 provides an example where all inversions agree within the uncertainty ellipse of the corresponding component (east, north, or radial), except for the north component of MAVEN. There are several cases (A2, A3, P2, Claritas Rupes, and Bosphoros Planum) where one component of the MAVEN data does not agree within the uncertainty ellipse, but this is always limited to only one component, which we find acceptable. Paleopole results for each component and analysis of acceptable anomalies can be found in Appendix C (Appendix Table C2-C4 and Appendix Figure C2).

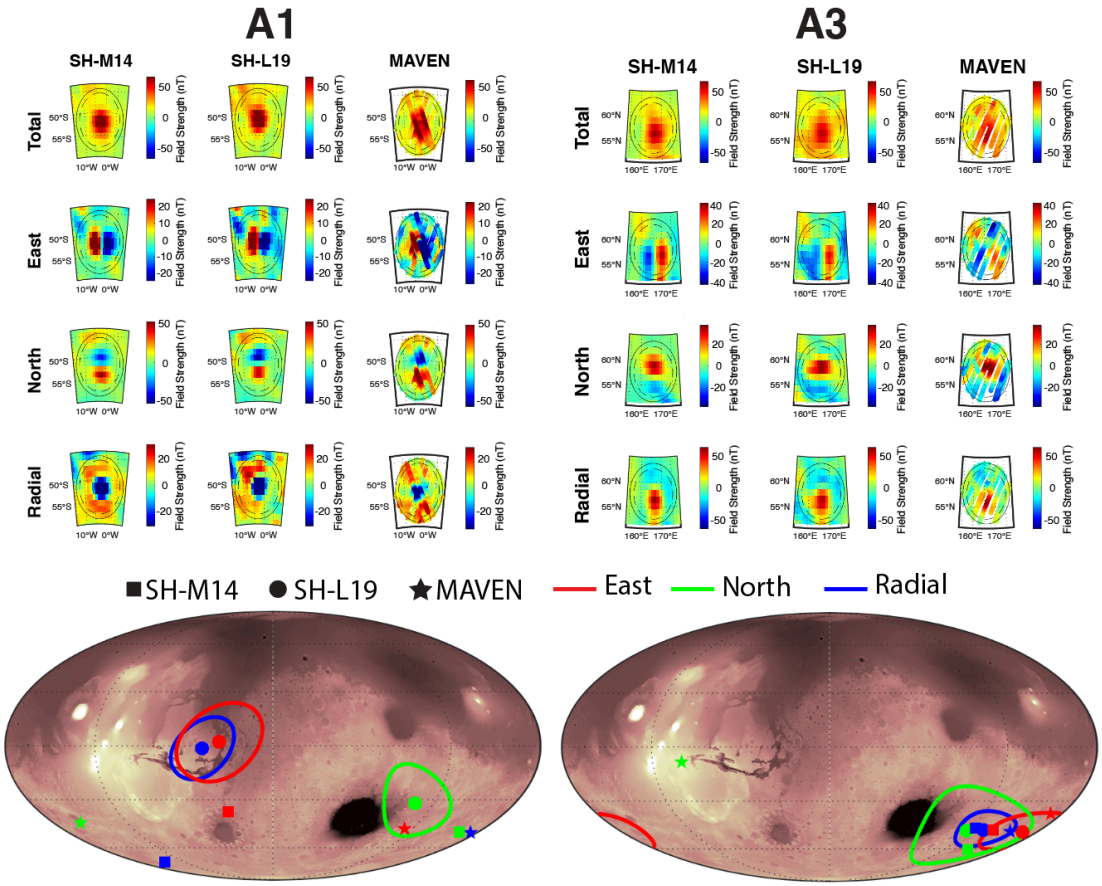

Figure 3.2: (top) Field components of A1 (left) and A3 (right). (below) Best-fit paleopole locations for each component and dataset plotted over MOLA data (Smith et al., 2001) in a mollweide projection centered on 0°N 0°E.

4 Results

We apply the methods from Section 3 to ten crustal magnetic anomalies. We perform Parker's method on each component (east, north, radial) of each dataset (SH-M14, SH-L19, and MAVEN) individually. We report the results using the radial component of SH-L19 in Table 1, as the radial component produces the best SNR in all cases. Note that all paleopole locations listed in this paper are south paleopoles. Figure 3 shows the radial field observations, best-fit model field, the residual field (i.e., the

difference between the observations and the model field), and the model dipole placement for each anomaly. The results using the east and north components of SH-L19, all components of SH-M14 and all components of MAVEN datasets can be found in the Supporting Information (Appendix Figure C2 and Appendix Tables C2-C4).

Table 3.1. Summary of crustal magnetic anomalies analyzed. Location of the anomaly in latitude (λ_s) and longitude (φ_s), radii of observations (r_o) and model dipoles (r_d), the SNR (radial component) value associated with each observational extent, the inclination (Inc) and declination (Dec) resulting from Parker's method, south paleopole latitude (λ_p) and longitude (φ_p), the precision parameter (*k),* and angular standard deviation (*s*) from the 20 Monte Carlo simulations to estimate uncertainty, and the paleopole ellipse semi-axes, *dm* and *dp,* derived from *s*. All are in units of degrees, except for SNR and *k* which are unitless. CR = Claritas Rupes, AM = Amazonis Mensa, TS = Terra Sirenum, MT = Margaritifer Terra, and BP = Bosphoros Planum. Note that r_d is always 1° smaller than r_o, except for Claritas Rupes and Terra Sirenum, which are 1.5° smaller than r_o.

Anomaly	A2	A3	A3b	P1	P2	CR	AM	TS	MT	BP
λ_s (°N)	-64.5	57.5	48.5	-16.5	35	-27	-5.5	-32.5	-1	-33
φ_s (°E)	28.5	166	169	30	213.5	254	216	190	342	297.5
r_o (°)	6	6	5	7.5	5.5	7.5	8	7	8	7
r_d (°)	5	5	4	6.5	4.5	6	7	5.5	7	6
SNR	13.1	6.0	4.1	7.1	7.8	6.2	10.2	6.4	7.1	7.4
Inc (°)	-78	-34	0	-58	-30	-50	-58	-76	-26	-30
Dec (°)	44	203	304	167	279	67	231	51	53	255
λ_p (°N)	72.2	-47.3	22.3	-33.7	-2.4	32	-25.2	46.1	35.9	-3.4
φ_p (°E)	144.5	132.3	52.4	197.9	105.6	4.7	78.6	339.5	88	185.9
k	68.5	27.2	38.6	18.2	28.3	33.7	48.3	16.2	127.9	91.2
s (°)	9.8	15.6	13.1	19.2	15.3	14.0	11.7	20.3	7.2	8.5
dm (°)	18.4	17.8	13.1	28.2	17.0	18.7	17.2	37.3	7.7	9.4
dp (°)	17.3	10.2	6.6	20.7	9.4	12.4	12.7	34.4	4.2	5.2

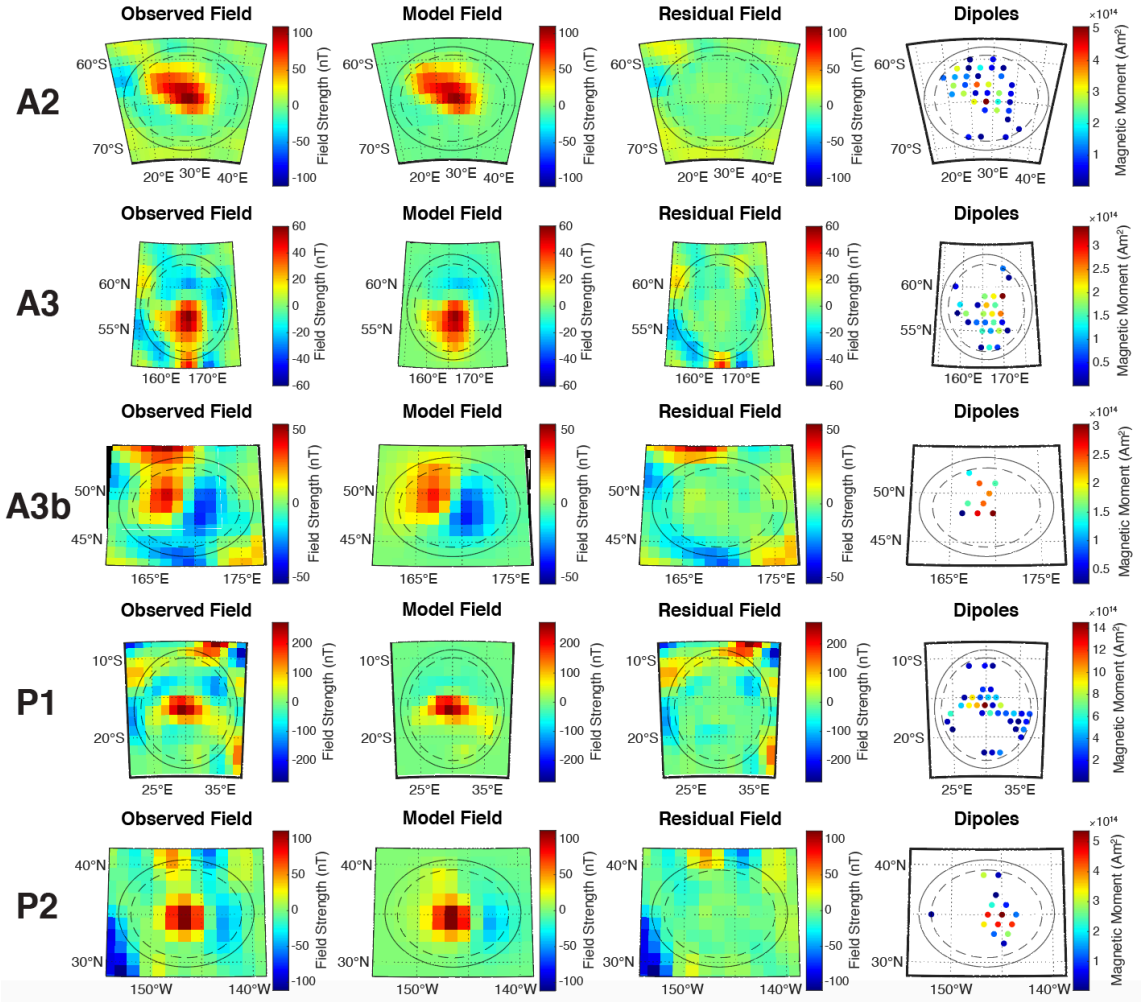
A2
A3
A3b
P1
P2
Observed Field
Model Field
Residual Field
Dipoles
Field Strength (nT)
Magnetic Moment (Am²)
60°S
70°S
20°E 30°E 40°E
60°N
55°N
160°E 170°E
50°N
45°N
165°E 175°E
10°S
20°S
25°E 35°E
40°N
30°N
150°W 140°W

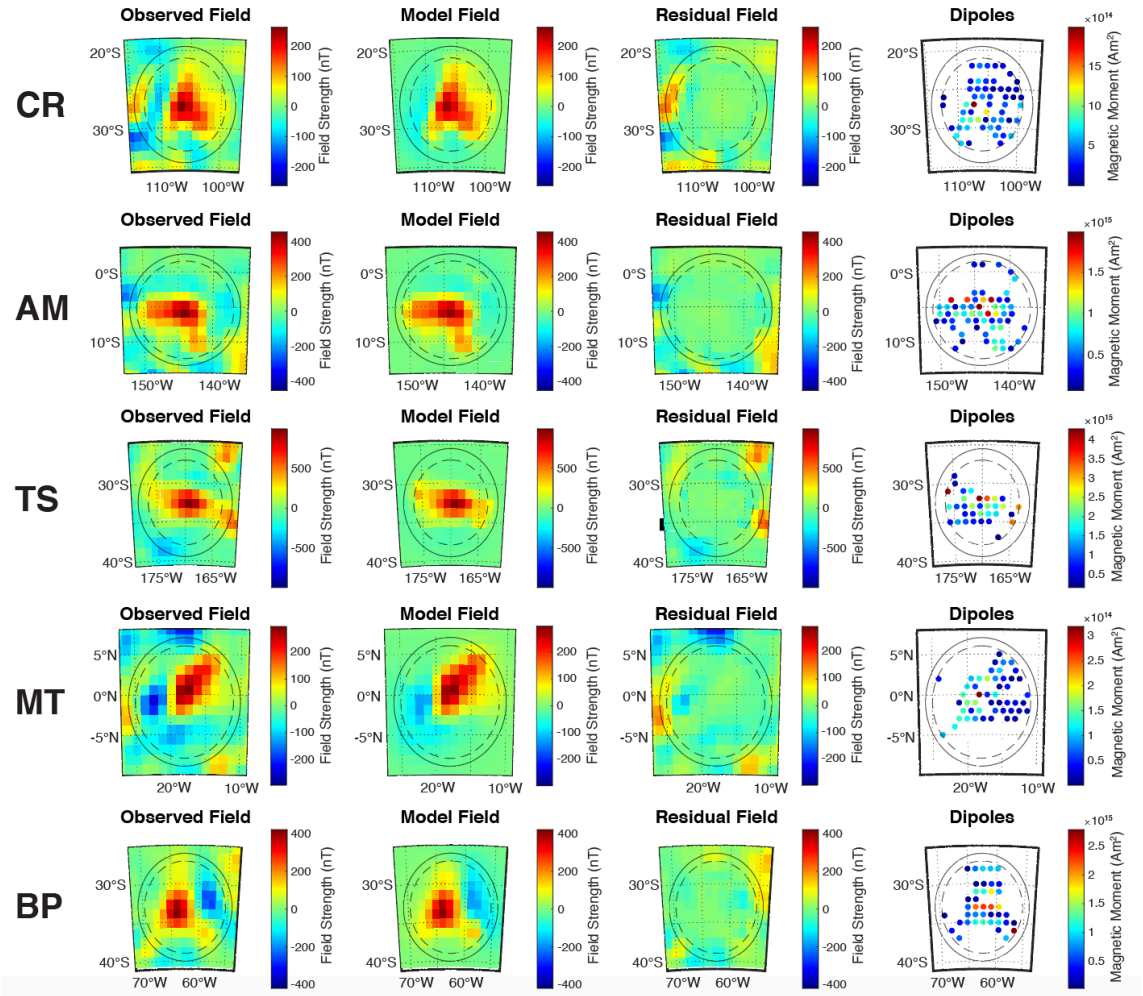

Figure 3.3: Visual summary of Parker's method for each anomaly. (first column) Observed radial field component of SH-L19. (second column) Model radial fields based on best-fit from Parker's method. (third column) Residual fields (i.e., the difference between observations and the model). (fourth column) Best-fit dipole arrangement. Solid lines indicate the extent of data used in the inversion (r_o) and dashed lines indicate the extent of dipoles (r_d). Figures are in the Lambert projection.

All anomalies discussed here have been previously analyzed by various authors, except A3b. Anomalies A2, A3, P1, and P2 use the naming convention from Thomas et al. (2018). Thomas et al. also analyzed anomaly A1 (Figure 3.2a), but our analyses suggest that, while well isolated, this anomaly is not well-suited to an inversion Parker's method, as described in Section 3. We do not include the Australes Montes anomaly, also

analyzed by Thomas et al. (2018) because the anomaly location is not consistent between the SH-M14 and SH-L19 datasets, and the SNR is quite low (<4). Though five anomalies in this study are labeled after the most distinct geologic feature in the region, in general, the geologic explanation for the existence of martian magnetic anomalies is not known.

For all anomalies, the magnetic field components (east, north, radial) are consistent for all three datasets, as required by the methods described in Section 3. The SH-M14 fields for P2 are approximately 5 times stronger than in SH-L19 or MAVEN, though inversion results using Parker's method indicate that this strength difference does not impact the recovered magnetization direction, as the results from SH-M14 are in proximity to those from SH-L19 and MAVEN. We compare our results to those reported in the literature (Appendix Figure C2).

Anomaly A2 was identified by Morschhauser et al. (2014) and analyzed by Thomas et al. (2018) to determine its paleopole location. Our results are consistent with the results from Thomas et al. (2018).

A3 was identified by Morschhauser et al. (2014) and analyzed by Thomas et al. (2018) to determine its paleopole location. This anomaly is moderately well isolated, with a significant secondary anomaly to the south, termed A3b. Our results are consistent with the results from Thomas et al. (2018).

A3b was not analyzed by Thomas et al. (2018), but we include it here given its proximity to A3 and that it appears to be a separate anomaly. A3b is associated with the northern tip of Phlegra Montes. It is moderately well isolated, with anomaly A3 to its

north. The paleopole location for this anomaly is distinctly different from the paleopole for A3, confirming that these are in fact separate anomalies.

Anomaly P1 was identified by Thomas et al. (2018), who also found the associated paleopole location. There are significant crustal fields to the north and northeast, however our choice of observational extent excludes these (presumably) unrelated crustal fields. Our results are consistent with the results from Thomas et al. (2018).

Anomaly P2 was identified by Thomas et al. (2018), who also found the associated paleopole location. There are significant crustal fields to the southwest, however our choice of observational extent excludes these (presumably) unrelated crustal fields. Our results are consistent with the results from Thomas et al. (2018).

The Claritas Rupes (CR) magnetic anomaly has been analyzed by several authors (Frawley and Taylor, 2004; Arkani-Hamed and Boutin, 2004; Hood et al., 2005; Boutin and Arkani-Hamed, 2006). There are significant crustal fields to the southwest, though our choice of observational extent excludes these (presumably) unrelated crustal fields. Our results are near results from Frawley and Taylor (2004), Arkani-Hamed and Boutin (2004), and Boutin and Arkani-Hamed (2006), though the reported literature values are outside our uncertainty ellipse. Our results using the east component of SH-L19 (the second highest SNR for this anomaly) is consistent with the reported value from Hood et al. (2005).

The anomaly in south Amazonis Mensa (AM) has been analyzed by several authors (Arkani-Hamed, 2001; Richmond and Hood, 2003; Frawley and Taylor, 2004;

Arkani-Hamed and Boutin, 2004; Hood et al., 2005; Boutin and Arkani-Hamed, 2006). This anomaly is the strongest in its immediate vicinity (within an arc distance of 10 degrees). There are significant crustal fields to the east, south, and west, however our choice of observational extent excludes these (presumably) unrelated crustal fields. Our results are consistent with the reported locations from Boutin and Arkani-Hamed (2006). Our results using the east component of SH-L19 (the second highest SNR) is consistent with the reported locations from Arkani-Hamed (2001), Richmond and Hood (2003), Arkani-Hamed and Boutin (2004), Hood et al. (2005), and Boutin and Arkani-Hamed (2006). The reported location from Frawley and Taylor is at much higher latitudes, though it is consistent with our results using the north component of SH-L19 (the lowest SNR).

An anomaly in Terra Sirenum (TS) has been studied by three authors (Frawley and Taylor, 2004; Hood et al., 2007; Quesnel et al., 2007). Though it is surrounded by (presumably) unrelated crustal fields on all sides, it is distinct from the surrounding fields as a separate crustal magnetic anomaly. Our results are consistent with the results from Quesnel et al. (2007). Our result for the north component of SH-L19 is consistent with Quesnel et al. (2007) and Hood et al. (2007). Our results are not consistent with Frawley and Taylor (2004).

The Margaritifer Terra (MT) anomaly has been studied by two authors (Arkani-Hamed, 2001; Richmond and Hood, 2004). Though it is surrounded by (presumably) unrelated crustal fields to the west, north, and east, it is distinct from the surrounding fields as a separate crustal magnetic anomaly. Our results are not consistent with the

previously reported results. Our results for the north component of SH-L19 produce an uncertainty ellipse that is just outside of the reported location of Richmond and Hood (2003).

Bosporpos Planum (BP) anomaly has been studied by several authors (Frawley and Taylor, 2004; Arkani-Hamed and Boutin, 2004; Hood et al., 2005; Boutin and Arkani-Hamed, 2006). It is in Bosporos Planum, to the south of Thaumasia Planum and to the northwest of Argyre basin. There are significant crustal fields to the northeast, however our choice of observational extent excludes these (presumably) unrelated crustal fields. Our results are near the reported location from Arkani-Hamed and Boutin (2004), though their value is outside of our uncertainty ellipse. Curiously, the reported locations from Boutin and Arkani-Hamed (2006) are antipodal to our results, which may be an error in reporting, given that the same group finds a paleopole opposite of this value (Arkani-Hamed and Boutin, 2004). Our results are not consistent with the reported locations from Frawley and Taylor (2004) or Hood et al. (2005).

4.1 Dispersion of Anomalies

A collection of paleopole uncertainties for each anomaly is shown in Figure 3.4 (left column). We assume magnetic reversals occurred, and we therefore show a combination of north and south paleopoles to indicate the best clustering of anomalies. The right column of Figure 3.4 condenses the information from the left column into a heat map of uncertainty ellipses to better show clustering of paleopoles. Heat maps are calculated by determining the latitudes and longitudes within the uncertainty ellipses and assigning each location a value equal to the number of ellipses present at that point. We

show results from the best component only (Figure 3.4, top row), from only the best two components (Figure 3.4, middle row), and from all components (Figure 3.4, bottom row). Note that the SNRs of the second best and worst components for several anomalies are <4 (Appendix C Table C2-C3), which should be considered unacceptable, but we show the results here for completeness.

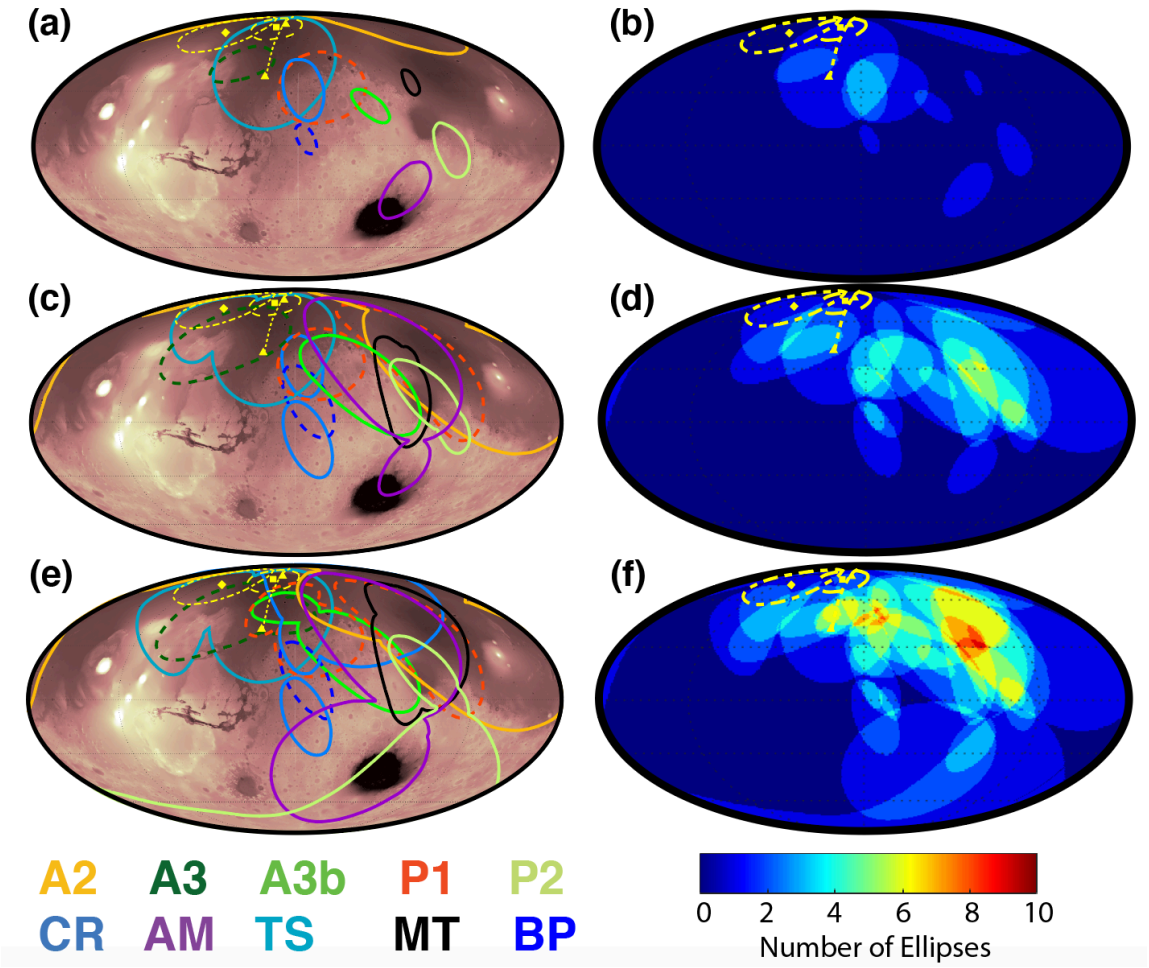

Figure 3.4: Paleopole results for the ten crustal magnetic anomalies analyzed. Shown are paleopole uncertainty ellipses plotted over MOLA data (Smith et al., 2001) (left column) and heat maps of ellipses (right column) for the best component only (a-b, total of ten), the best two components (c-d, total of twenty) and all three components (e-f, total of thirty). For (c) and (e) only the furthest extent of ellipses from each anomaly are shown. Heat maps indicate the number of ellipses in a particular location. Shown here is a mix of north and south paleopoles: north paleopoles have dashed ellipses and south paleopoles

have solid ellipses. Mollweide projection is used, centered on 0°N 0°E. CR = Claritas Rupes, AM = Amazonis Mensa, TS = Terra Sirenum, MT = Margaritifer Terra, and BP = Bosphoros Planum. Paleo-spin axes from Perron et al. (2007), Matsuyama and Manga (2010), and Chan et al. (2016) have been included in yellow: the dotted line corresponds to the axis of rotation described in Perron et al. (2007), the dash-dotted ellipse corresponds to the uncertainty from Matsuyama and Manga (2010), and the dashed ellipse corresponds to the uncertainty from Chan et al. (2018).

To quantify the clustering from our results, we make use of the Maximum Angle of Dispersion (MAD) as described in Kirschvink (1980), which uses principal component analysis to describe the angular dispersion of a set of points on a sphere. The latitudes and longitudes (equally spaced to ensure no oversampling at the poles) contained within each ellipse are converted to cartesian coordinates, which are then used to create matrix H, whose center is forced through the origin. The eigenvalues and eigenvectors of matrix H determine the principal components. The eigenvector with the largest corresponding eigenvalue indicates the "center of mass" of the points, i.e., the axis around which the uncertainty ellipses cluster. We then calculate the MAD as in Kirschvink et al.:

$$MAD = \tan^{-1}\sqrt{\frac{\lambda_{int} + \lambda_{min}}{\lambda_{max}}}$$

where λ_{max} is the maximum eigenvalue, λ_{int} is the intermediate eigenvalue, and λ_{min} is the minimum eigenvalue. This method of citing dispersion is not dependent on magnetic reversals as paleopoles that are antipodal to one another will have the same angular distance from the "center of mass" axis, and thus using only south paleopoles or a combination of north or south paleopoles will have the same result.

We use a Monte Carlo method to determine the expected MAD for a random assortment of uncertainty ellipses. To ensure a fair comparison between our results and

the randomly generated ellipses, we use the calculated *dp* and *dm* from our uncertainty analysis of SH-L19 data to create random ellipses of the same size as our uncertainty ellipses. We allow the location of these ellipses to be random within a Fisher distribution and then calculate the MAD for the randomly placed ellipses. We repeat this 1,000 times to determine the distribution of expected MAD.

For the best component of each anomaly (total of ten ellipses), the MAD is 37.3°, which we show in Figure 3.5 is below 1-σ of what would be expected of randomly placed uncertainty ellipses of the same sizes. For the two best components (total of twenty ellipses), the MAD is 47.0°, and for all three components (total of thirty ellipses), the MAD is 48.1°. The sharp increase in MAD from the best component only to including multiple components is due to the increase in size of the uncertainty ellipse – uncertainty is expected to increase as SNR decreases – as it increases the number and spread of points used in the MAD calculation. These MADs for the best two components and for all components are within 1-σ of what would be expected of randomly placed uncertainty ellipses of the same sizes, though both are still below the expected mean.

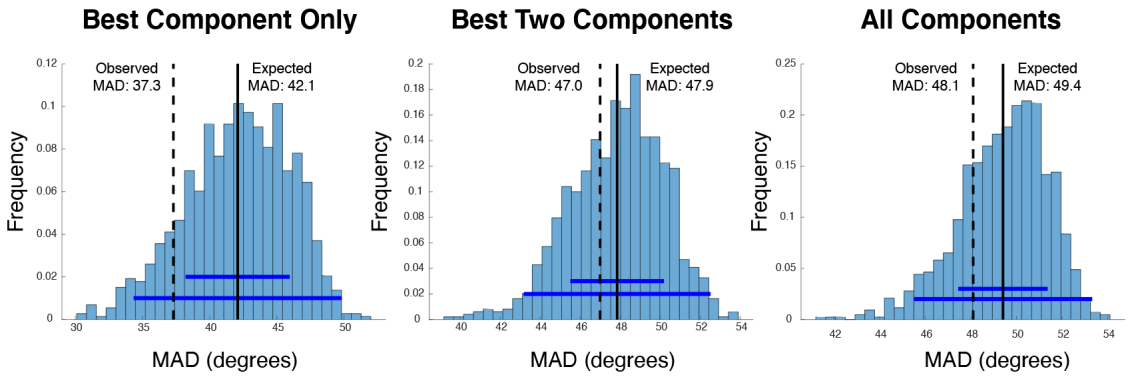

Figure 3.5: Histograms of Maximum Angle of Dispersion (MAD) for random arrangements of (left) the best components only (ten uncertainty ellipses), (b) the best two components (twenty uncertainty ellipses), and (c) all components of SH-L19 (thirty

uncertainty ellipses). Dashed black lines indicate the MAD of the uncertainty ellipses, solid black lines indicate the expected (mean) MAD, calculated from 1000 iterations of random ellipse placements. Solid blue lines indicate 1-σ (top) and 2-σ (bottom). Note that the ellipses generated in these random tests are of the same size as the uncertainty ellipses in our results for accurate comparison.

5 Discussion

5.1 Clustering

Using the MAD as a proxy for how well clustered a set of anomalies are, we have shown (Figure 3.5) that that the MAD of the uncertainty ellipses from this analysis is lower than the expected MAD at the 1σ level from an assortment of randomly located ellipses of a similar size, suggesting a clustering of paleopoles. This can be seen visually in Figure 3.4, where the heat maps of uncertainty ellipses overlap in several areas, with at least one clustering area if we assume the results from the best component are the true paleopole locations. If we accept the second or third best components as truth, we find clusters in two locations (approximately 45°N, 0°E and 30°N, 90°E).

The cluster seen in Figure 3.4b correlates with the paleo-spin axis found by Perron et al. (2007). This cluster consists of four uncertainty ellipses (Figure 3.6), which are exceedingly well clustered with a MAD of 26.3° – more than 2-σ from the expected MAD for randomly placed ellipses of the same size. We discuss this further in Section 5.2.

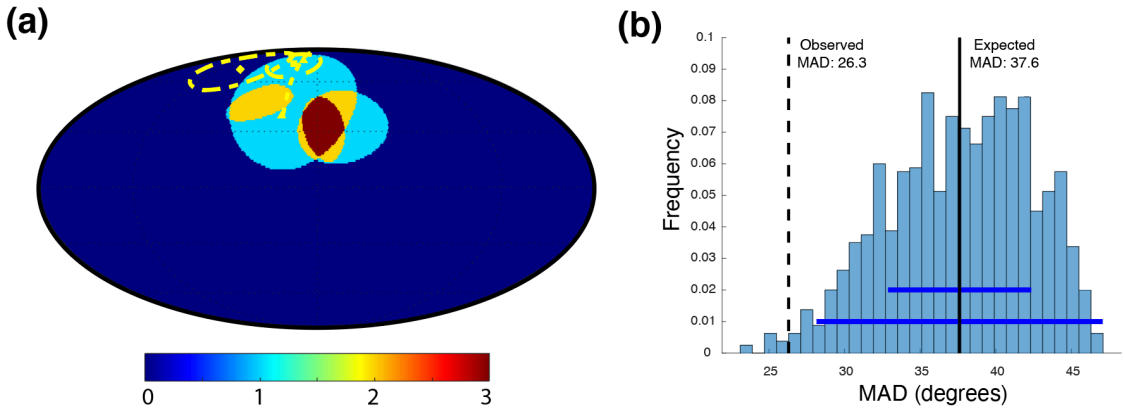

Figure 3.6: (a) Heat map of the four best clustered anomalies. Paleo-spin axes from Perron et al. (2007), Matsuyama and Manga (2010), and Chan et al. (2016) have been included in yellow: the dotted line corresponds to the axis of rotation described in Perron et al. (2007), the dash-dotted ellipse corresponds to the uncertainty from Matsuyama and Manga (2010), and the dashed ellipse corresponds to the uncertainty from Chan et al. (2018). (b) Histogram of MAD for randomly arranged uncertainty ellipses of the six best clustered anomalies. Anomalies included in this clustering: A3, P1, Claritas Rupes, and Terra Sirenum. Dashed black lines indicate the MAD of the uncertainty ellipses, solid black lines indicate the expected (mean) MAD, calculated from 1000 iterations of random ellipse placements. Solid blue lines indicate 1-σ (top) and 2-σ (bottom). Note that the ellipses generated in these random tests are of the same size as the uncertainty ellipses in our results for accurate comparison.

Clusters of paleopoles suggest that either the dipolar axis was stable for an extended period or that some of the anomalies we analyze were magnetized contemporaneously. Without knowledge of the age of the crustal magnetic anomalies, we cannot distinguish between these possibilities, though locations where there are overlapping north and south poles provide evidence for at least one pole reversal event in the time the dipolar axis was stable.

5.2 True Polar Wander

A few of the individual anomalies we analyze appear to be consistent with the current or past spin axes. A2 is consistent with a dipolar axis aligned with the current spin axis. A3 and Terra Sirenum are consistent with a dipolar axis aligned with the paleo-spin

axes calculated by Perron et al. (2007), Matsuyama and Manga (2010), Bouley et al. (2016), and Chan et al. (2018), though the uncertainty ellipses are too large to distinguish between the different axes.

The cluster of six anomalies (Figure 3.6) appear to correlate with the paleo-spin axis calculated by Perron et al. (2007). This implies a large amount of true polar wander, given the low latitude of the paleopoles (~45°N), which is in conflict with the relatively smaller amount of true polar wander expected from the creation of Tharsis Rise (e.g., Matsuyama and Manga, 2010). However, given that the cluster is statistically significant (outside of the 2-σ MAD expected for randomly placed paleopoles), we find it important to emphasize this correlation.

5.3 Alternative Scenarios

5.3.1 Multipolar Fields

One possible explanation for the lack of agreement in all magnetic paleopole locations is that the ancient magnetic field of Mars was multipolar. Paleopole calculations inherently assume a dipolar magnetic field axis so if the field were multipolar, the calculated paleopole locations would be incorrect. We show here that this is unlikely to be able to explain the wide spread of paleopole locations by calculating the amount a dipolar field would be perturbed by a quadrupolar component.

Dynamo-generated magnetic fields are produced at the core-mantle boundary (CMB) of planet. These fields are attenuated as the distance from the CMB increases, and this attenuation is different for each order term (e.g., dipolar and quadrupolar). The attenuation of a field at the surface of a planet can be written as

$$A_l = \left(\frac{R_{CMB}}{R_{surface}}\right)^{-(l+2)}$$

where l indicates the order of the field. For a dipolar term, $l = 1$, and for a quadrupolar term, $l = 2$.

As we can see in the equation above, higher order terms are attenuated away much faster than lower order terms. Therefore, quadrupolar fields will be fractionally weaker than dipolar terms at the same distance from the CMB. This fraction f can be written as

$$f = \frac{A_1}{A_2}$$

In addition to having higher attenuation, the quadrupole term is also weaker than the dipolar term at the CMB. We label this fractional strength α. We estimate α to be approximately 0.2 for the Earth (Stacey, 1985), and assume the martian dynamo behaved similarly to Earth's current dynamo field. We can now compute the strength of quadrupolar field B_q (with respect to the strength of the dipolar field B_d) as

$$B_q = B_d * f * \alpha$$

Finally, determining the amount a dipolar field would be perturbed by a quadrupolar component depends on the angle of the quadrupolar term with respect to the dipolar axis, which we label as ϕ. The quadrupolar field can be split into two components: parallel to the dipolar term and perpendicular to the dipolar term.

$$B_{q,\parallel} = B_q \cos\phi$$

$$B_{q,\perp} = B_q \sin\phi$$

We can now determine the angle θ by which the dipolar field is perturbed by a quadrupolar term (i.e., the amount a magnetization direction would be perturbed by a quadrupolar field).

$$\theta = \tan^{-1} \frac{B_{q,\perp}}{B_d + B_{q,\parallel}}$$

The maximum angle of perturbation (ϕ = 90°) is 6.2° while the mean angle of perturbation (ϕ = 0° to 90°) is 3.7°. These angles are quite small, and indeed much smaller than our angular standard deviations (Table 1).

We therefore rule out multipolar fields as an explanation for the wide spread of paleopole locations based on the assumption that the martian dynamo field behaved similarly to the Earth's field. However, some work has been done to suggest that the martian dynamo did not behave as the Earth's does, which we discuss in the next section.

5.3.2 A Hemispherical Dynamo

To explain the dichotomy of crustal magnetism on Mars, one paper suggests that Mars may have had a hemispherical dynamo (Stanley et al., 2008). This could be achieved by a degree-1 pattern of mantle circulation resulting from mantle convection or radial viscosity variations (Zhong and Zuber, 2001; Roberts and Zhong, 2006), early magma ocean crystallization resulting in overturn (Elkins-Tanton et al., 2003; Elkins-Tanton et al., 2005), superplumes resulting from destabilization of the mantle lower thermal boundary layer (Ke and Solomatov, 2006), or a giant impact (Wilhelms and Squyres, 1984) that could produce a degree-1 temperature anomaly in the mantle or at the CMB (Watters et al., 2009). Their numerical simulations show that a stable one-

hemisphere dynamo could be produced for sufficiently long enough to cause significant magnetization in the southern hemisphere and weaker magnetization in the northern hemisphere. Such a magnetic field would render paleopole analyses useless given that paleopole calculations rely on the assumption of a dipolar magnetic field.

Our results do not support such a dynamo. Although paleopole locations may be useless under this scheme, such a dynamo would require the magnetization direction of anomalies near one another to be in approximately the same direction. Anomalies A3 and A3b are located 9° apart but their magnetization directions are different by 99°. Such a large difference in magnetization direction could not be explained by a stable hemispherical dynamo.

6 Conclusions

We analyze 10 martian crustal magnetic anomalies to determine the magnetic paleopole locations at the time the anomalies were magnetized using Parker's method (Parker, 1991). We use an updated method of estimating paleopole location uncertainty and perform this analysis on multiple datasets to ensure accurate results. We use the Maximum Angle of Dispersion (MAD) developed by Kirschvink (1980) to state the dispersion of our paleopole results.

Our results imply at least one cluster of paleopole locations, suggesting either the dipolar axis was stable for an extended period or that some of the anomalies we analyze were magnetized contemporaneously. The largest cluster of paleopole locations correlates with the paleo-spin axis calculated by Perron et al. (2007) using the paleo-shorelines of

the Arabia shoreline. This supports the true polar wander history put forth by Perron et al. but does not necessarily rule out the histories posited by Matsuyama and Manga (2010), Bouley et al. (2016), or Chan et al. (2018). However, we cannot confirm the timing of the polar wander from our magnetic analyses, as the age of the crustal magnetic anomalies in this study is not known.

We rule out multipolar fields and a hemispherical dynamo as explanations for the wide spread of paleopole locations, though the numerous paleopoles that do not correspond to the current or ancient spin-axes are still unexplained.

Appendix A: Supplementary Information for Chapter 1

Text A1:
In order to calculate paleopole locations, follow Irving (1964) and Butler (1992). We first find *p*, the magnetic colatitude by

$$p = \tan^{-1}\frac{2}{\tan I}$$

where *I* is inclination. We then find the paleopole latitude, λ_p, using

$$\lambda_p = \sin^{-1}(\sin\lambda_s \cos p + \cos\lambda_s \sin p \cos D)$$

where λ_s is the latitude of the anomaly and *D* is the declination. To find the paleopole longitude, ϕ_p, we calculate the longitudinal difference between the paleopole and anomaly location, β which is calculated as

$$\beta = \sin^{-1}\left(\frac{\sin p \sin D}{\cos\lambda_p}\right)$$

If

$$\cos p \geq \sin\lambda_s \sin\lambda_p$$

Then

$$\varphi_p = \varphi_s + \beta$$

where ϕ_s is the longitude of the anomaly. But if

$$\cos p < \sin\lambda_s \sin\lambda_p$$

Then

$$\varphi_p = \varphi_s + 180 - \beta$$

We can calculate the angular standard deviation, *s*, and angular variance, s^2, of the 20 magnetization directions from the noise-added Monte Carlo simulations at each anomaly:

$$s^2 = \frac{1}{N-1}\sum_{i=1}^{N}\Delta_i^2$$

where N is the number of unit vectors and Δ_i is the angle between the i-th direction and the calculated mean direction. Note that here, the angular standard deviation is for 63% of all values, as opposed to the 68% in traditional statistics. We can also calculate the precision parameter, k (Butler, 1992):

$$k = \frac{N-1}{N-R}$$

Where R is the resultant vector. Higher values of k mean lower uncertainty.

The paleopole error ellipse derived from s is characterized by the semi-axes dp and dm, such that dp is along the great circle that connects the anomaly location with the paleopole location and dm is perpendicular to that great circle. We can then calculate dm and dp, which describe the uncertainty ellipse for a given uncertainty:

$$dp = s\left(\frac{1+3\cos^2 p}{2}\right)$$

$$dm = s\left(\frac{\sin p}{\cos I}\right)$$

Typically, in the paleomagnetism community the 95% confidence interval is used in place of s. Since we are unable to calculate a confidence interval at this time, we use s that we obtain from our Monte Carlo simulations, as described above.

Text A2:

Our uncertainty estimation method relies on a Monte Carlo method wherein we use Parker's method on a number of synthetic cases based on an original Parker's method inversion on spacecraft data. As described in the text, we test synthetic models with added synthetic background fields that have a similar Signal to Background Ratio (SBR) to the real-world case. As seen in Appendix Figure A5, this variance in synthetic background fields creates a spread in best-estimate magnetization directions. This spread centers around the true direction (the direction known before adding a synthetic background field). One can imagine that the initial Parker's method inversion would be one of the blue dots seen in Figure S5, which is not necessarily the true direction. Applying a Monte Carlo style of inversions based around this initial finding would then

not only encompass this direction, but also the true direction that we sought in the first inversion. This is the key to our method. The result from Parker's Method might not necessarily be accurate, but the accurate direction does lie within the precision of the uncertainty estimation method we describe (Appendix Figure A6).

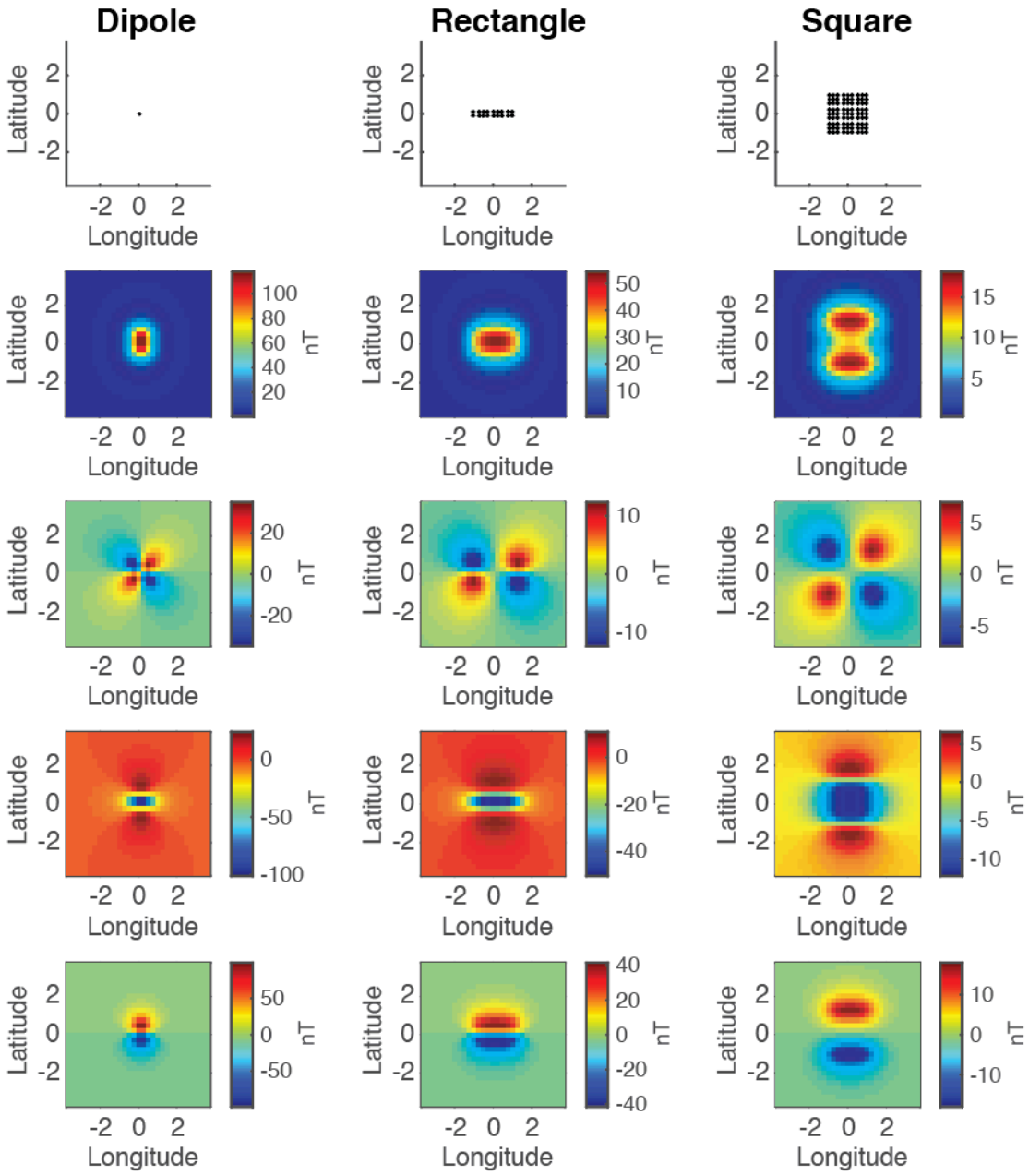
Dipole
Rectangle
Square
Latitude
Longitude
nT
-2 0 2
100 80 60 40 20
50 40 30 20 10
15 10 5
20 0 -20
10 0 -10
5 0 -5
0 -50 -100
0 -20 -40
5 0 -5 -10
50 0 -50
40 20 0 -20 -40
10 0 -10

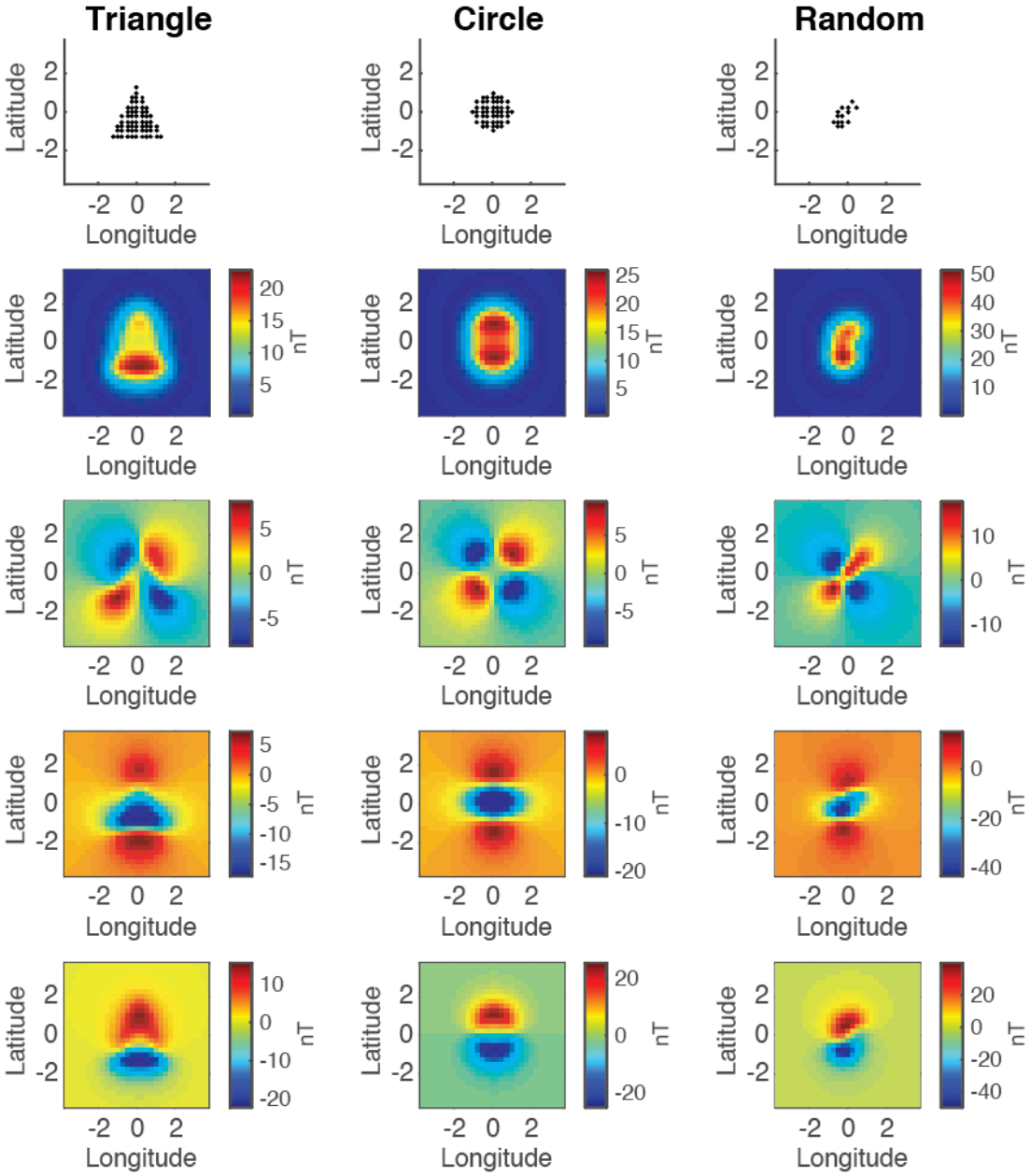

Figure A1. Test cases with varying shapes as described in Table 1.1. Shown are 0° inclination and 0° declination cases. These fields are calculated at 20 km altitude. Points within the dataset are on a 0.25° x 0.25° grid.

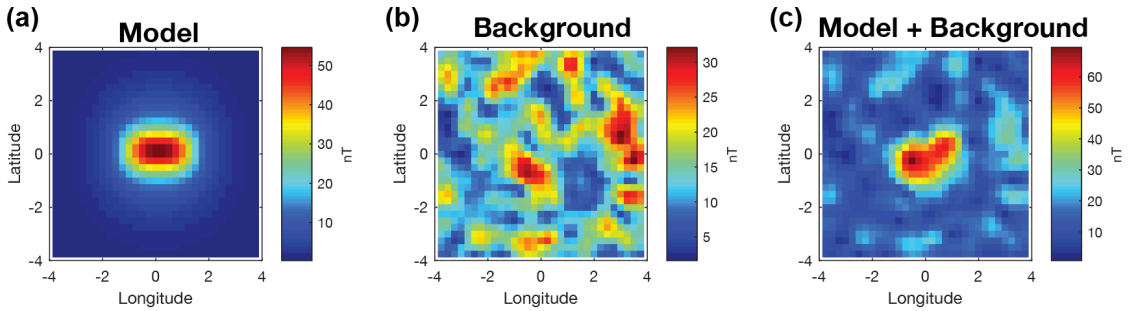

Figure A2. Example of how background field oscillations are added to synthetic anomalies. (a) A synthetic dataset with a rectangular shape is added to (b) a background field map generated from a grid of dipoles with random directions and magnetization strengths to create (c) a synthetic dataset with the background field added. See the Methods section for further details.

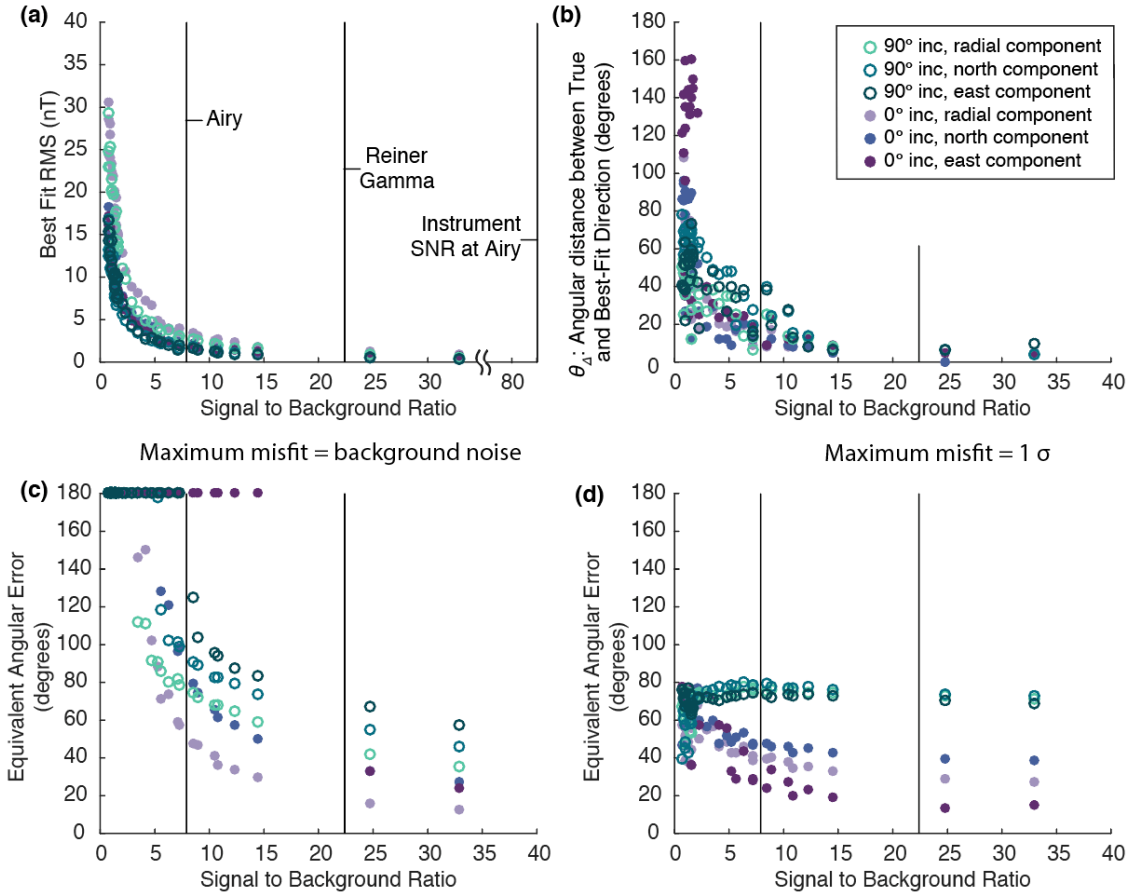

Figure A3. Inclination bias across SBR values for a rectangular source. Same as Figure 1.8 but using different synthetic background field datasets to generate SBR values. Synthetic background field datasets were generated with the same grid of dipoles but with different magnetization directions and magnitudes. (a) The best-fit RMS value for

differing SBR values, (b) the angular difference between the true and best-fit directions, θ_Δ, (c) the equivalent angular error for a maximum misfit equal to the mean background field, (d) the equivalent angular error for a maximum misfit equal to 1 σ. The SBR values associated with the Reiner Gamma and Airy magnetic anomalies are denoted by vertical black lines at 23 and 8, respectively. All test cases had a declination of 0°.

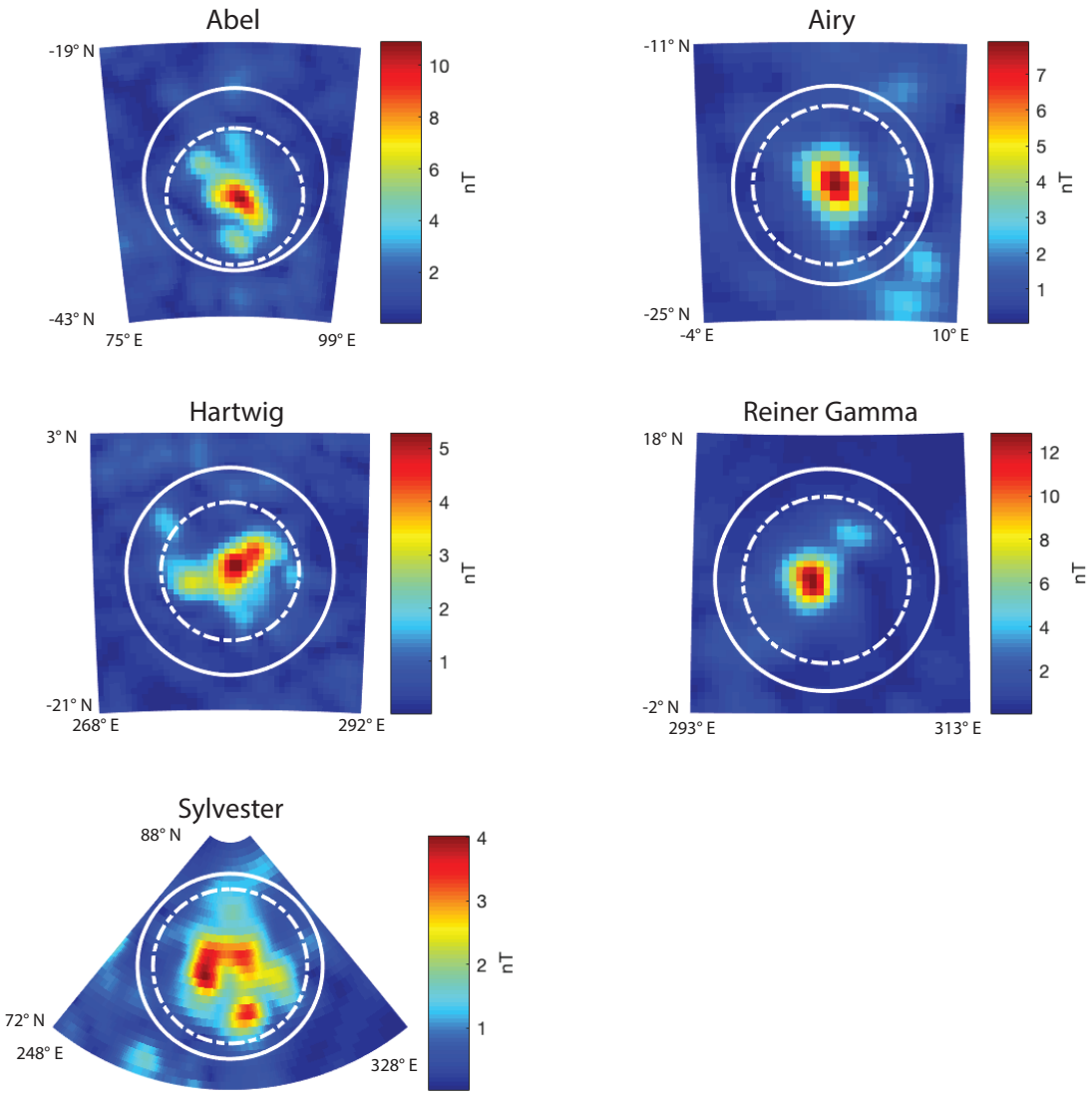

Figure A4. Boundaries of data used for inversions at Abel, Airy, Hartwig, Reiner Gamma, and Sylvester. Dashed lines represent the smaller data extent while solid lines show the larger extent (Table 1.2). Shown is the total magnetic field in stereographic projection centered on the anomaly. Note that the data radii for Abel are centered on two different locations (see main text).

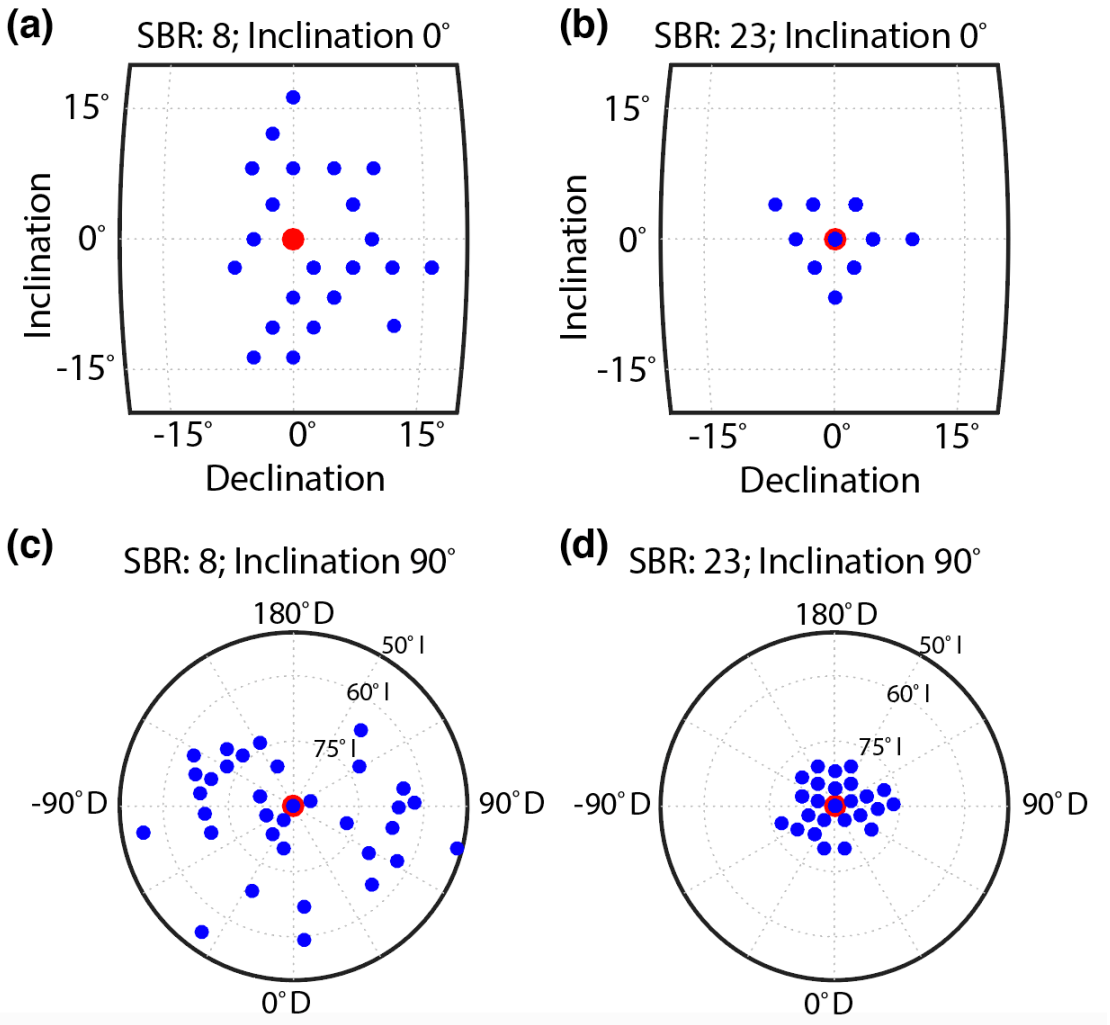

Figure A5. Best-estimate directions from inversions for the magnetization direction of a synthetic rectangular anomaly to assess the accuracy of Parker's Method (in contrast to its precision). Red points shows the rectangle's true direction and blue dots show the result of an inversion with background fields added. (a) SBR of 8 and inclination of 0°; (b) SBR of 23 and inclination of 0°; (c) SBR of 8 and inclination of 90°; and (d) SBR of 23 and inclination of 90°. All declinations are 0°. Each case was tested 40 times (blue points); some blue points overlap. Note that (c) and (d) are polar projections, centered on 90° inclination, extending to 50° inclination.

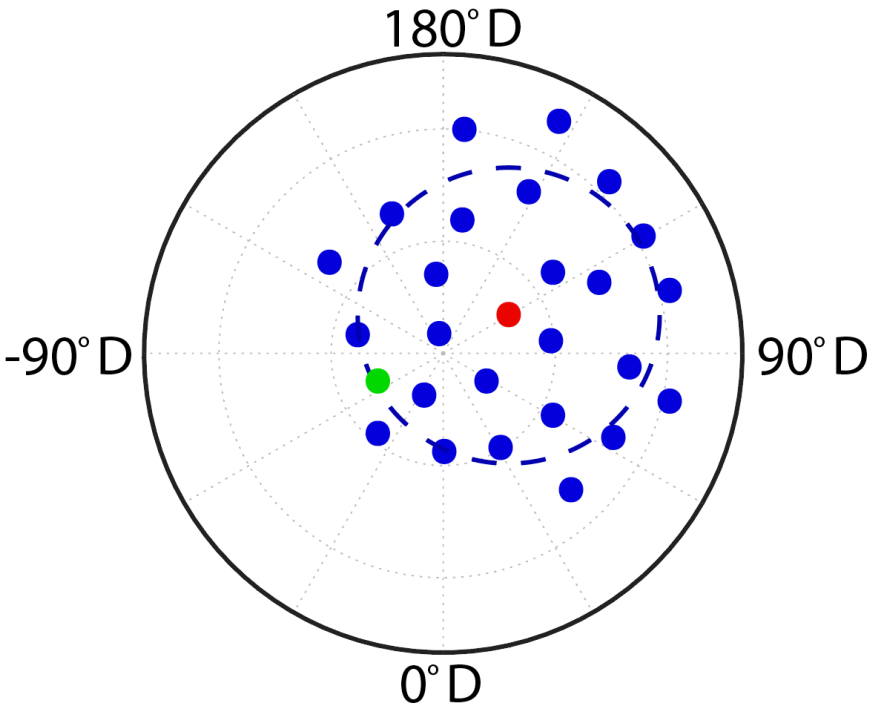

Figure A6. Cartoon showing how hypothetical Monte Carlo simulations described in Section 2.5 are, on average, expected to encompass the true direction for relatively high SBR values. The green dot is the true direction, the red dot is the "best-fit" direction from an inversion with Parker's Method, and the blue dots are the "perturbed directions" after adding background fields to the best-fit model. Blue dashed line represents the uncertainty estimation, which on average expected to include the true direction.

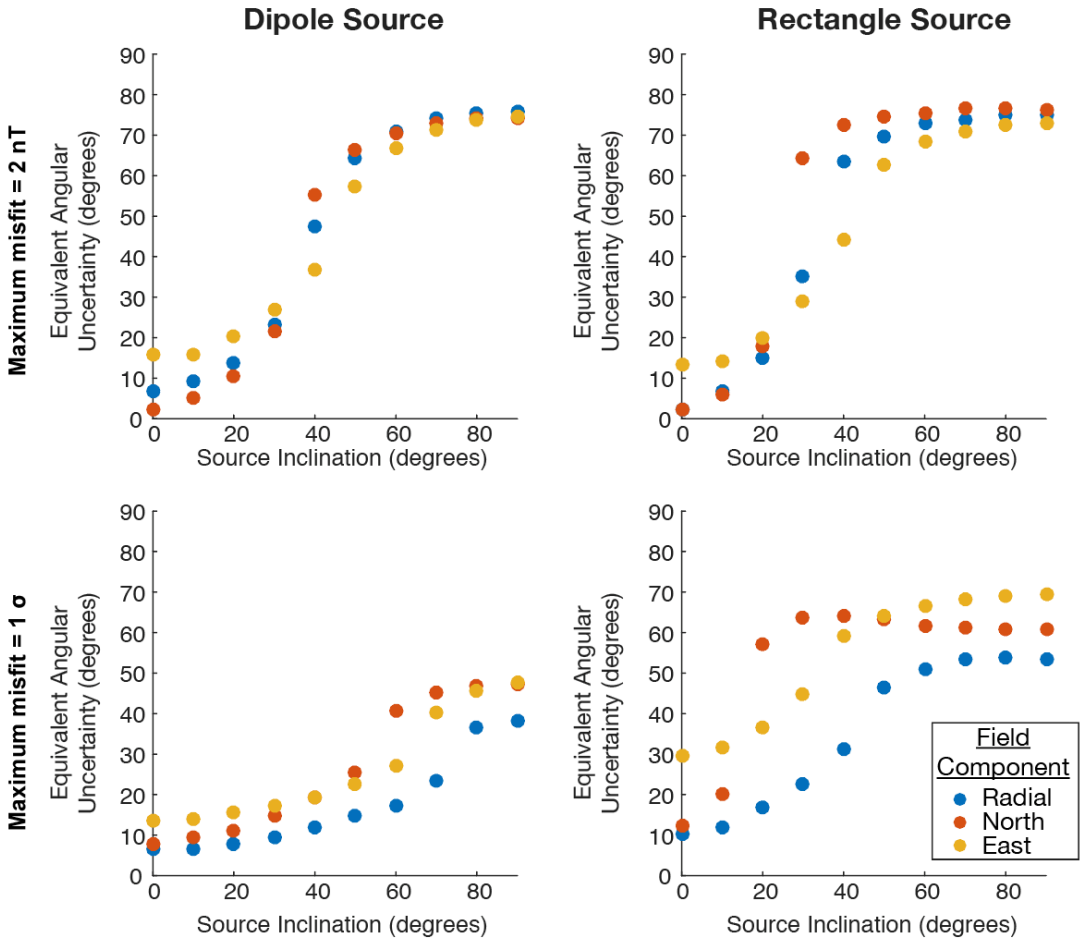

Figure A7. Similar to Figure 1.6. Higher inclinations give systematically higher uncertainties, regardless of the declination. Results shown here are for Parker's Method applied to the dipole and rectangle anomalies (with a constant 90° declination for all tests) using a maximum misfit of 2 nT (top rows) and 1σ (bottom rows). Negative inclinations are not shown, as the results are identical to those for positive inclinations.

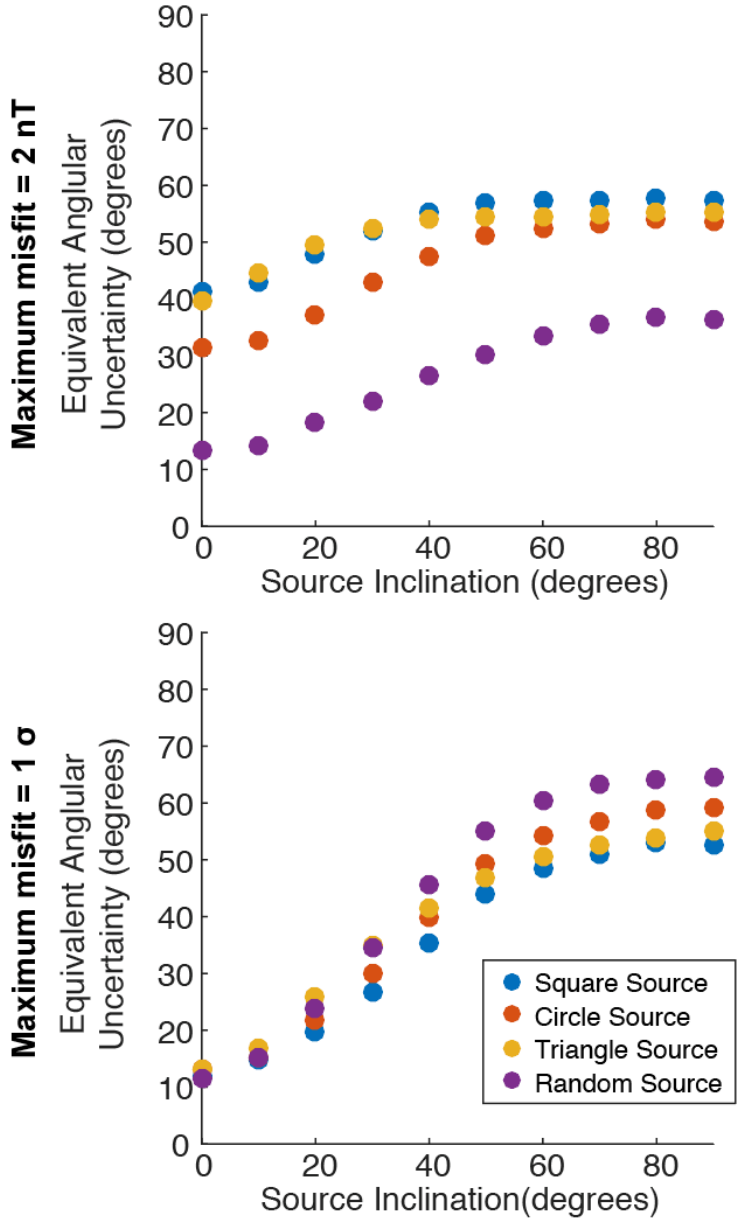

Figure A8. Higher inclinations give systematically higher uncertainties, regardless of the shape of the anomaly. Results shown here are for Parker's Method applied to square, circle, triangle, and randomly shaped anomalies (with a constant 90° declination for all tests) using a maximum misfit of 2 nT (top row) and 1σ (bottom row). Only the radial field component is used. The magnetic fields of the source shapes can be seen in the Figure A1. Negative inclinations are not shown, as the results are identical to those for positive inclinations.

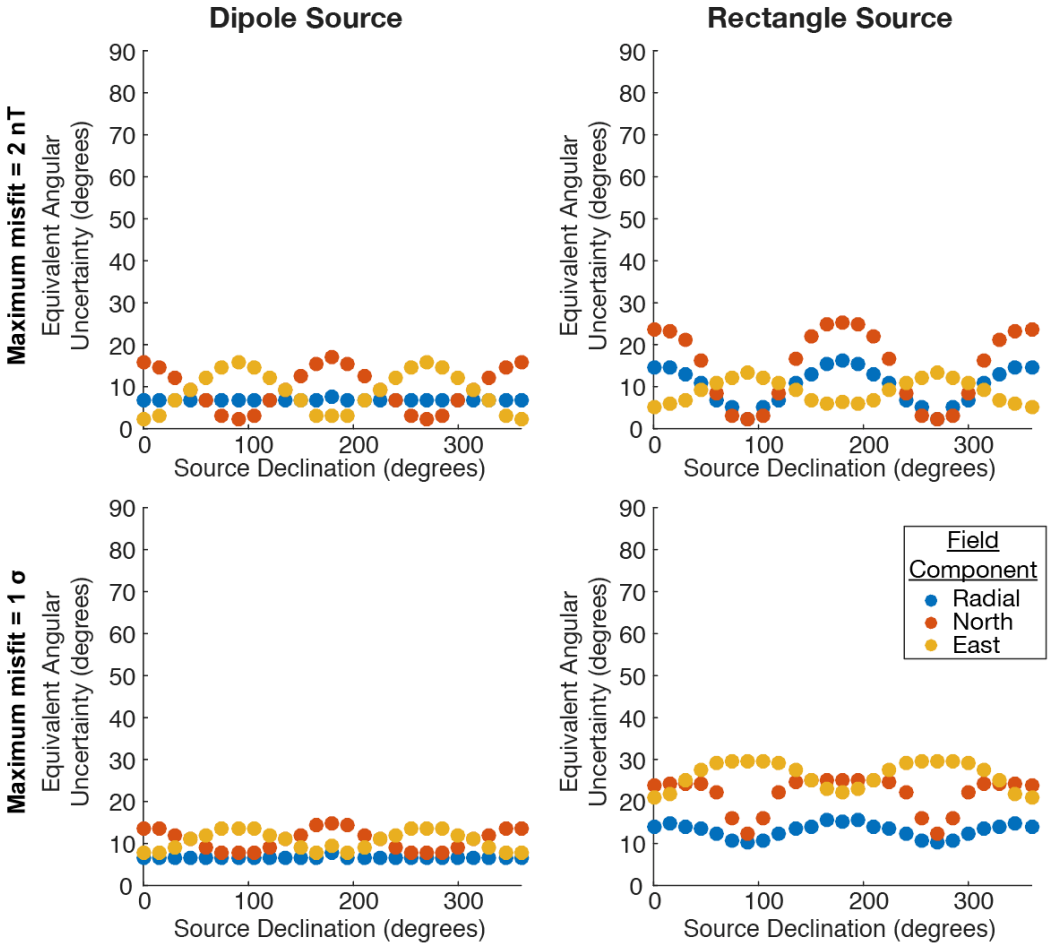

Figure A9. Uncertainties also vary with declination, though on a smaller order of magnitude. Results shown here are for Parker's Method applied to the dipole and rectangle anomalies (with a constant 0° inclination for all tests) using a maximum misfit of 2 nT (top rows) and 1σ (bottom rows). Negative inclinations are not shown, as the results are identical to those for positive inclinations. Compare with Figure A6.

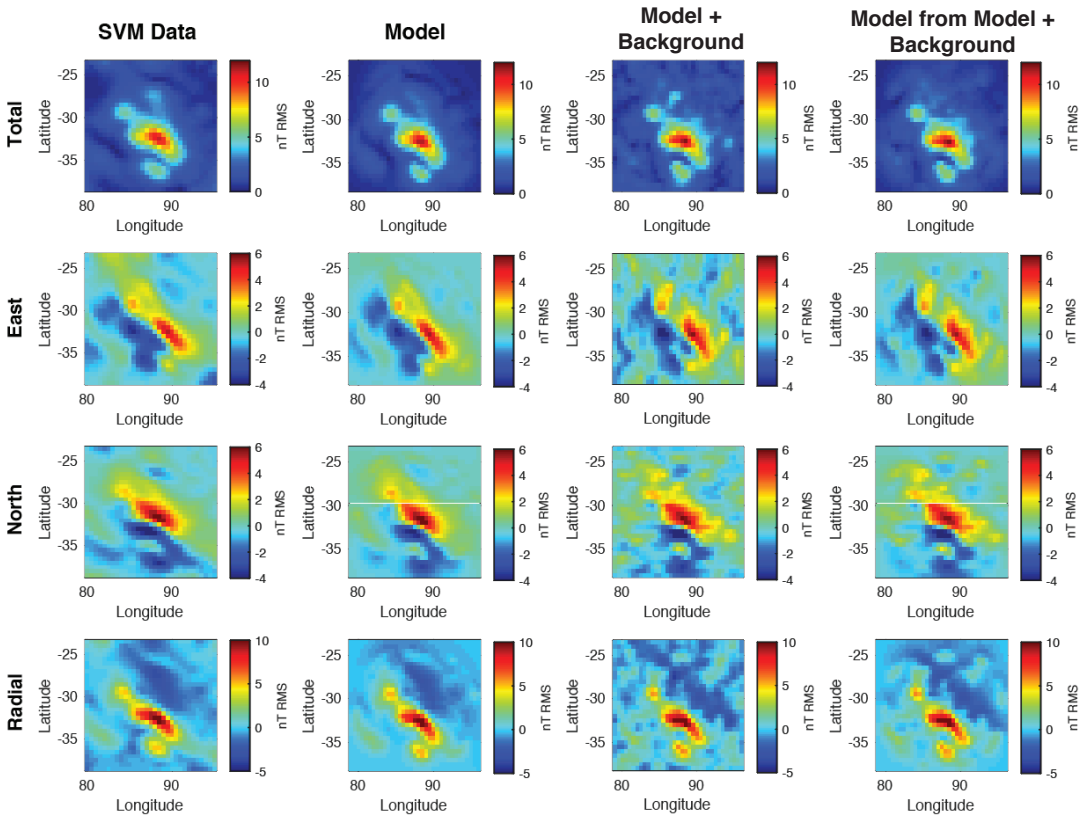

Figure A10. Magnetic field map of the Abel magnetic anomaly at 30 km altitude using the SVM dataset (Tsunakawa et al., 2015), the best-estimate model of Abel from Parker's Method, the best-estimate model plus noise appropriate for Abel, and the best-estimate model from Parker's Method applied to the model plus noise. All datasets are at a 0.5° x 0.5° grid resolution.

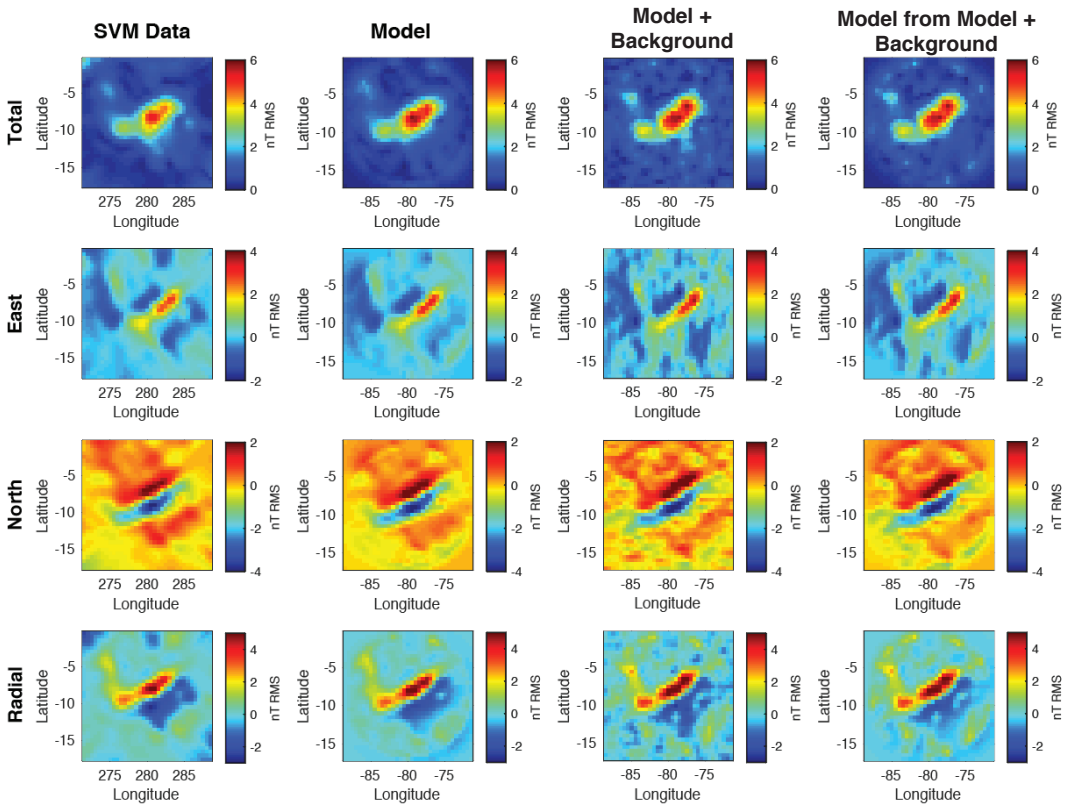

Figure A11. Magnetic field map of the Hartwig magnetic anomaly at 30 km altitude using the SVM dataset (Tsunakawa et al., 2015), the best-estimate model of Hartwig from Parker's Method, the best-estimate model plus noise appropriate for Hartwig, and the best-estimate model from Parker's Method applied to the model plus noise. All datasets are at a 0.5° x 0.5° grid resolution.

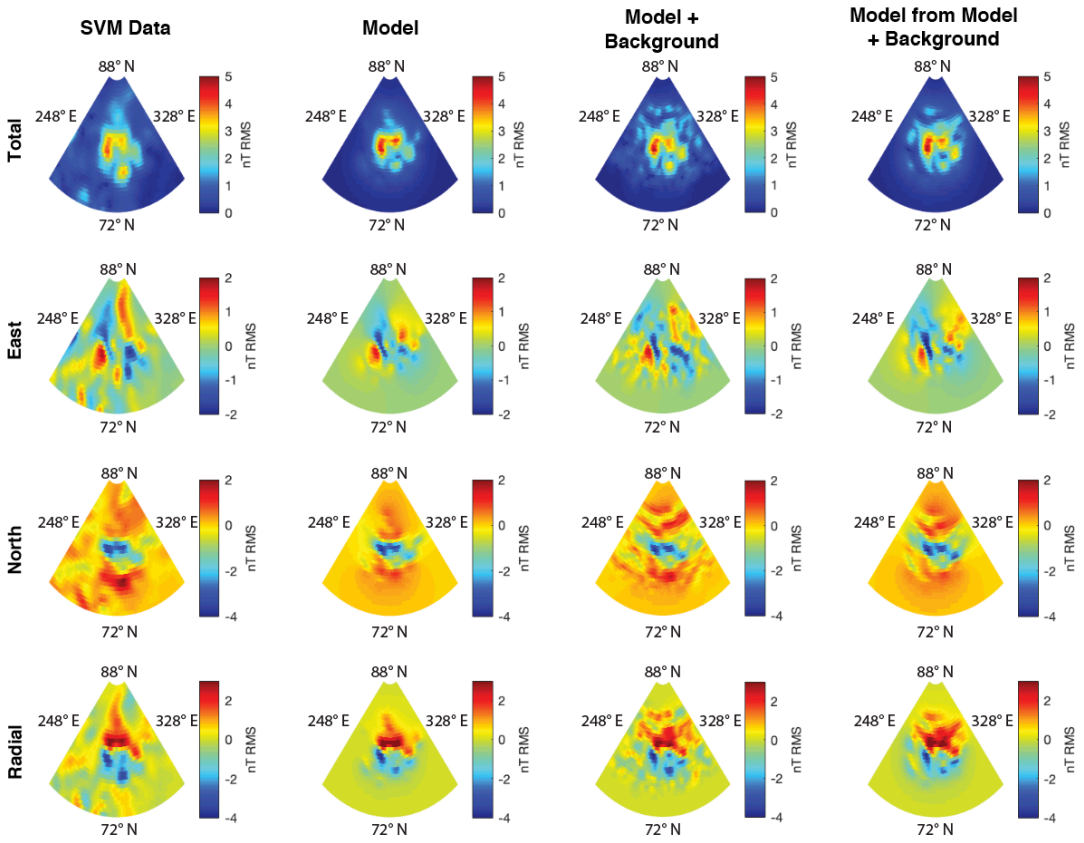

Figure A12. Magnetic field map of the Sylvester magnetic anomaly at 30 km altitude using the SVM dataset (Tsunakawa et al., 2015), the best-estimate model of Sylvester from Parker's Method, the best-estimate model plus noise appropriate for Sylvester, and the best-estimate model from Parker's Method applied to the model plus noise. All datasets are at a 0.5° x 0.5° grid resolution. Stereographic projection centered on the anomaly.

Appendix B: Supplementary Information for Chapter 2

Text B1: Best-Fit Elastic Thickness and Loading Fraction

Latitude	Longitude	T_e (km)	σ T_e (km)	F1	σ F1	Combined RMS
90	0	47.6	0.653	0.596	0.003	0.301
75	15	24.87	0.221	0.355	0.002	0.383
75	75	24.18	0.579	0.508	0.004	0.341
75	90	24.22	0.559	0.529	0.004	0.303
75	105	23.68	0.555	0.575	0.005	0.31
75	120	51.9	1.609	0.604	0.005	0.384
75	135	57.88	1.597	0.63	0.005	0.275
75	150	57.7	1.58	0.642	0.005	0.245
75	165	49.03	1.591	0.648	0.004	0.239
75	180	26.27	1.162	0.664	0.004	0.329
75	195	27.91	1.137	0.669	0.004	0.333
75	210	29.49	0.899	0.667	0.004	0.306
75	225	28.35	1.028	0.657	0.004	0.292
75	240	28.44	1.253	0.627	0.005	0.322
60	105	20.62	0.234	0.466	0.003	0.323
60	120	16.24	0.447	0.566	0.005	0.326
60	135	15.64	0.446	0.653	0.006	0.323
60	150	20.58	0.844	0.671	0.006	0.327
60	165	37.82	0.809	0.555	0.004	0.276
60	180	47.68	0.206	0.423	0.001	0.263
60	195	47.14	0.201	0.442	0.001	0.374
60	210	42.75	0.409	0.525	0.002	0.249
60	225	38.94	0.396	0.491	0.003	0.315
60	345	29.31	0.484	0.234	0.003	0.394
45	105	16.65	0.618	0.605	0.007	0.391
45	120	14.2	0.371	0.614	0.007	0.374
45	135	14.09	0.25	0.59	0.007	0.323
45	150	15.12	0.402	0.609	0.006	0.336
45	165	21.42	0.791	0.58	0.006	0.313
45	180	25.38	0.613	0.465	0.004	0.312
45	195	19.68	0.555	0.493	0.005	0.387
45	210	31.48	0.838	0.502	0.005	0.28

45	270	51.02	1.301	0.413	0.005	0.378
30	75	34.48	0.277	0.408	0.001	0.293
30	120	14.13	0.366	0.54	0.007	0.362
30	195	14.61	0.329	0.565	0.005	0.322
30	210	18.47	0.48	0.568	0.005	0.229
30	225	24.68	0.705	0.608	0.005	0.398
30	240	45.06	0.885	0.559	0.004	0.281
30	255	55.75	1.079	0.495	0.004	0.359
15	105	18.49	0.498	0.549	0.005	0.352
15	120	18.45	0.453	0.643	0.006	0.17
15	135	15.85	0.539	0.838	0.01	0.373
15	195	16.1	0.307	0.589	0.005	0.242
15	210	13.33	0.213	0.694	0.007	0.24
15	225	17.6	0.284	0.638	0.01	0.383
15	255	33.93	1.117	0.529	0.006	0.189
0	105	22.36	0.735	0.529	0.006	0.369
0	120	18.67	0.862	0.706	0.006	0.211
0	135	14.08	0.389	0.892	0.006	0.242
0	150	35.69	1.913	0.673	0.007	0.189
0	165	21.88	0.541	0.55	0.005	0.294
0	180	15.55	0.28	0.561	0.006	0.23
0	195	11.22	0.163	0.915	0.004	0.249
0	210	12.93	0.243	0.886	0.005	0.241
-15	60	22.73	0.258	0.504	0.003	0.398
-15	120	8.43	0.274	0.823	0.009	0.398
-15	135	13.28	0.45	0.738	0.008	0.284
-15	150	10.68	0.271	0.803	0.007	0.31
-15	165	10.37	0.318	0.751	0.008	0.342
-15	180	14.84	0.377	0.644	0.007	0.152
-15	195	9.88	0.223	0.751	0.012	0.219
-15	210	13.66	0.399	0.812	0.008	0.249
-15	225	39.78	1.807	0.623	0.01	0.286
-15	240	59.57	2.073	0.545	0.009	0.317
-30	0	26.77	0.277	0.401	0.003	0.351
-30	15	24.53	0.667	0.456	0.005	0.335
-30	60	25.34	0.597	0.615	0.004	0.335
-30	120	44.04	1.079	0.547	0.005	0.308

-30	135	16.76	0.41	0.613	0.006	0.381
-30	150	12.86	0.321	0.683	0.008	0.237
-30	165	10.47	0.255	0.789	0.008	0.239
-30	180	17.26	0.37	0.68	0.006	0.187
-30	195	13.24	0.227	0.665	0.008	0.29
-30	210	11.32	0.182	0.909	0.004	0.347
-30	225	16.64	0.491	0.686	0.007	0.224
-30	255	26.27	0.174	0.343	0.002	0.389
-45	15	24.06	0.594	0.537	0.004	0.225
-45	30	25.88	0.586	0.52	0.004	0.252
-45	45	23.55	0.634	0.593	0.005	0.321
-45	75	43.39	2.368	0.533	0.006	0.348
-45	90	41.52	0.557	0.519	0.003	0.283
-45	105	41.78	0.415	0.509	0.003	0.382
-45	135	15.02	0.88	0.66	0.013	0.36
-45	150	11.82	0.325	0.703	0.008	0.343
-45	180	27.37	0.831	0.703	0.007	0.279
-45	225	12.32	0.234	0.642	0.006	0.281
-45	240	17.73	0.358	0.542	0.004	0.325
-45	300	24.64	0.692	0.51	0.006	0.317
-45	315	40.19	0.847	0.378	0.005	0.307
-45	330	36.27	0.389	0.425	0.004	0.254
-45	345	42.41	0.455	0.595	0.003	0.399
-60	0	17.83	0.329	0.668	0.005	0.386
-60	15	17.79	0.25	0.545	0.005	0.344
-60	30	16.22	0.276	0.493	0.005	0.306
-60	45	14.4	0.315	0.536	0.006	0.32
-60	60	13.62	0.341	0.565	0.006	0.342
-60	195	16.33	0.329	0.724	0.008	0.354
-60	210	14.45	0.304	0.683	0.006	0.238
-60	225	14.03	0.286	0.651	0.006	0.23
-60	240	15.15	0.269	0.615	0.005	0.293
-60	255	16.1	0.269	0.592	0.004	0.379
-60	270	16.11	0.38	0.6	0.005	0.385
-60	285	21.06	0.687	0.554	0.005	0.308
-60	300	33.1	0.885	0.552	0.006	0.231
-60	315	28.95	0.835	0.582	0.007	0.295

-60	330	28.97	0.768	0.549	0.006	0.208
-60	345	24.94	0.807	0.636	0.005	0.249
-75	0	18.49	0.58	0.672	0.008	0.207
-75	15	17.57	0.58	0.657	0.008	0.21
-75	30	15.94	0.687	0.656	0.009	0.237
-75	45	11.33	0.372	0.683	0.008	0.333
-75	60	10.42	0.233	0.673	0.007	0.388
-75	210	16.48	0.528	0.636	0.006	0.348
-75	225	17.19	0.422	0.653	0.006	0.243
-75	240	17.42	0.404	0.678	0.006	0.214
-75	255	18.75	0.414	0.694	0.006	0.201
-75	270	21.27	0.463	0.697	0.006	0.192
-75	285	24.12	0.573	0.69	0.006	0.19
-75	300	24.54	0.624	0.692	0.006	0.186
-75	315	23.23	0.597	0.691	0.007	0.183
-75	330	21.73	0.614	0.686	0.007	0.176
-75	345	19.8	0.612	0.684	0.007	0.191
-90	0	31.34	0.835	0.594	0.007	0.325

Table B1. Results with a combined RMS value less than 0.4. Shown are Latitude (°N), Longitude (°E), elastic thickness (km), standard deviation in elastic thickness (km), loading fraction, standard deviation in loading fraction, and combined RMS (equation 20).

Text B2. Synthetic testing

We find that the standard deviations in our best-fit values from synthetic testing fall into two categories. In areas with a combined RMS of <0.4 (from MCMC inversion of observed spectra), the synthetic-derived standard deviations agree reasonably well with the MCMC-derived standard deviations in both elastic thickness (Appendix Figure B1a) and loading fraction (Appendix Figure B1b). Areas with a combined RMS >0.4 produce much higher standard deviations in both elastic thickness and loading fraction. Figure 2.4 in the main text shows that areas with RMS > 0.4 do not yield reliable results.

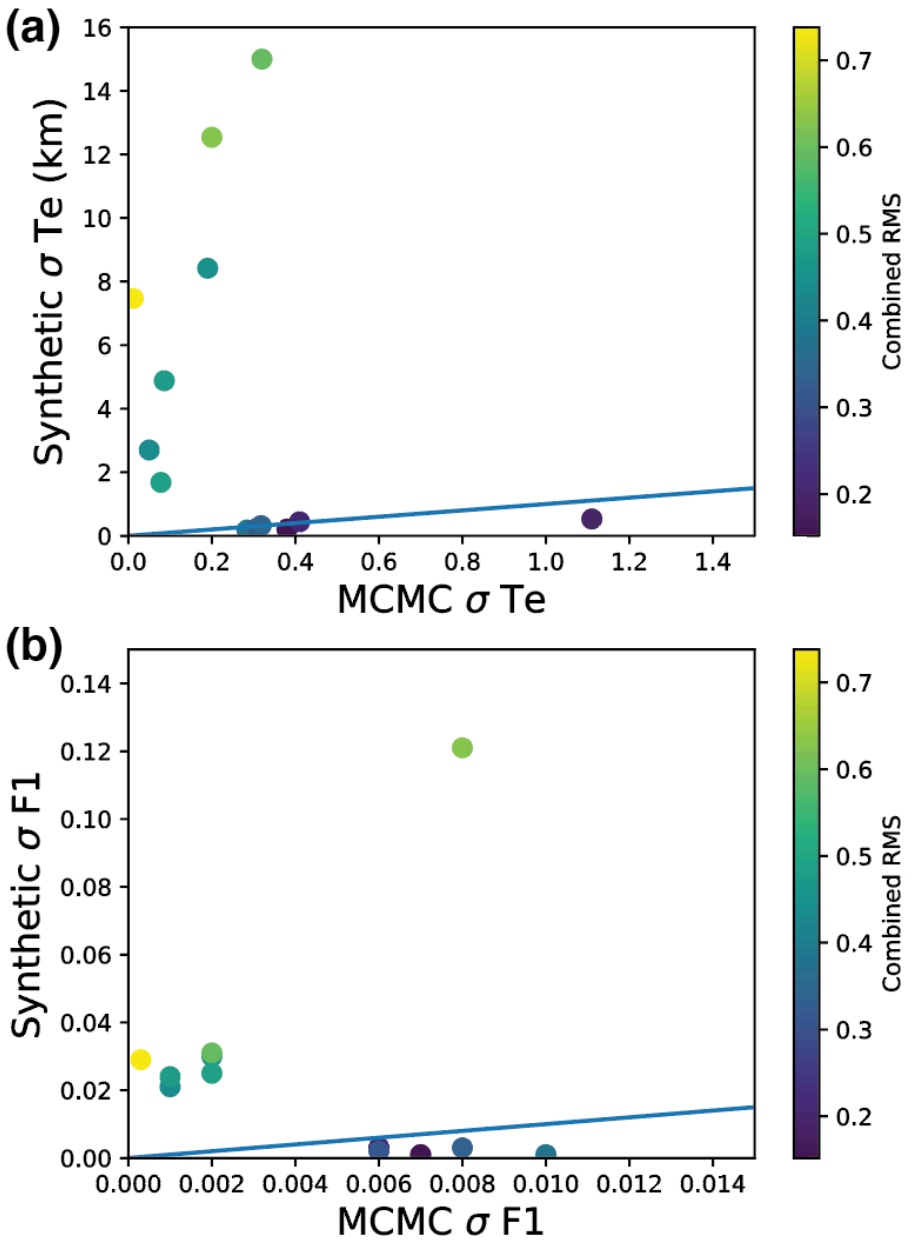

Figure B1: MCMC-derived standard deviations versus synthetic test-derived standard deviations for (a) elastic thickness and (b) loading fraction. Results are color-coded by their combined RMS values from best fits to observed spectra; values of RMS above 0.4 are not considered reliable (see text). Blue lines indicate a slope of one. Values below the blue line are locations where the MCMC-derived standard deviations were larger than the synthetic test-derived standard deviations.

Text B3. Window Testing

We test a variety of window sizes at six locations. We calculate the observed spectra for each window size (using the largest bandwidth that produces a single taper of concentration >99%) and create synthetic spectra using the method described in Section 2.4 (where we add noise until the synthetic coherence matches the observed coherence). We then perform MCMC inversion on each pair of synthetic admittance and coherence. For window radii >20° (Appendix Figure B2a-c), the best-fit elastic thickness matches the input elastic thickness. Below a radius of 20°, the error in the best-fit elastic thickness values increases markedly and is biased towards lower values. We perform all inversions in the main text using a window radius of 25°, given that it is slightly better than the window radius of 20°.

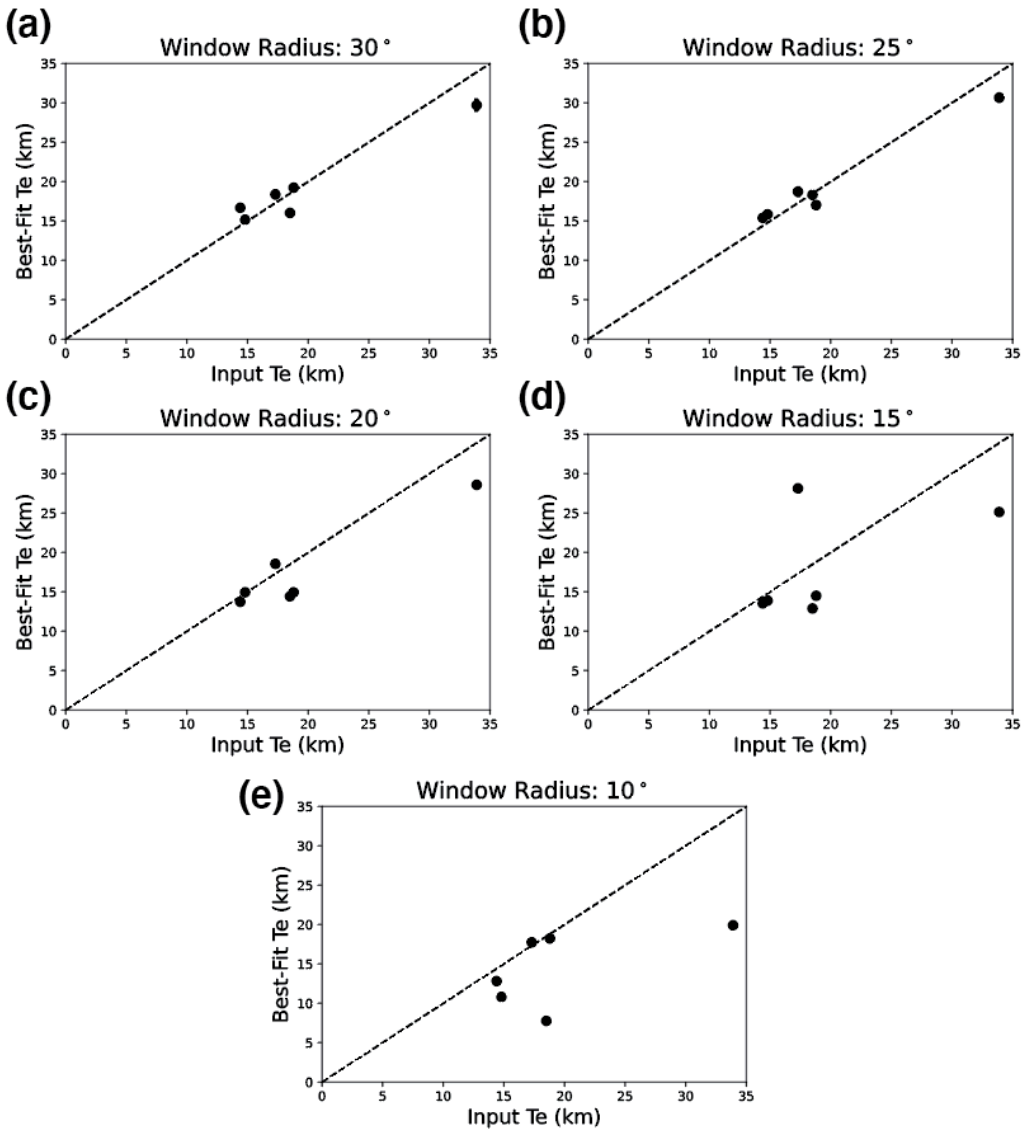

Figure B2: Input (synthetic) T_e value plotted against recovered best-fit T_e value for selected regions, shown for windows of different radii. Window radius dictates the smallest degree l_{min} that can be fit. Dashed lines indicate a slope of one. Note that for window radii < 20° the error in the best-fit T_e values increases markedly and is biased towards lower values.

Appendix C: Supplementary Information for Chapter 3

Text C1: Data and Dipole Spacing Tests

We tested the effect of data and dipole resolution on synthetic data in order to compare the best-fit direction with the known true direction. We tested five different cases with synthetic noise added to determine trends.

While increasing data resolution (decreasing data spacing) does improve the best-fit direction from Parker's method, the improvements stop around a data spacing of 1.33°, regardless of dipole spacing. An example where dipole spacing is kept constant at 1° is shown in SI Figure 1a. We therefore choose our data spacing of SH-M14 and SH-L19 to be 1.33°, even though the spherical harmonic models can be expanded to 0.8° and 0.66°, respectively.

Counterintuitively, increasing dipole resolution (decreasing spacing) does not necessarily improve the best-fit direction. In cases with low noise (green and cyan in SI Fig 1b), there is no advantage to using finer dipole spacing. In cases with high noise (blue, black, and red in SI Fig 1b), finer dipole spacing can negatively impact the best-fit direction. With more dipoles available to model the field, Parker's method attempts to model the small variations in the data. If there is higher noise in the system, these uncorrelated fields can heavily influence the field and force Parker's method away from the true direction. We choose a dipole spacing of 1° for this paper as it maintains a good resolution while avoiding the worst effects of high noise.

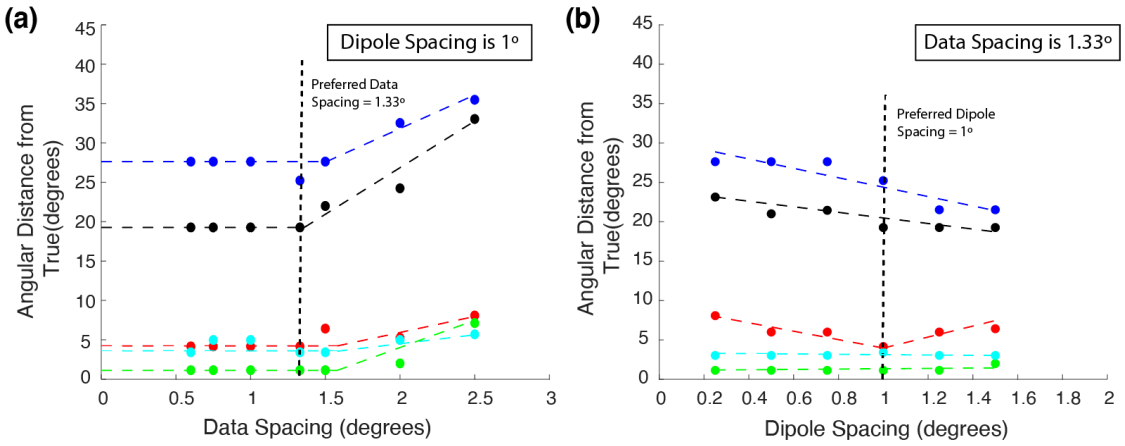

Figure C1. (a) Effects of data spacing on recovered best-fit direction. Each color represents a different noise case. Our preferred data spacing is 1.33°. (b) Same as in (a) but for dipole spacing. Our preferred dipole spacing is 1°.

Text C2. Spurious MAVEN data tracks

In our use of MAVEN magnetometer data, we found a few spurious tracks of data. Here we refer to spurious tracks as data that do not match the surrounding data. Listed here are the tracks of data we removed from our analysis.

Anomaly	r_o	**Tracks removed (yyyyddd)**
A2	6°	2016287, 2016288, 2016312, 2016314, 2016325, 2016365, 2015366, 2020081
A3	6°	2016290, 2019266, 2019312
A3b	5°	2016260, 2015059
P1	7.5°	None
P2	5.5°	2014291, 2015056, 2019256
CR	7.5°	None
AM	8°	None
TS	7°	None
MT	8°	2017293, 2017304
BP	7°	None

Table C1. MAVEN tracks removed from analysis. Tracks are listed according to their year and day of year (format: yyyyddd).

Text C3. Results from other components and datasets

We also use each component (east, north, and radial) of each dataset (SH-M14, SH-L19, MAVEN) determine the paleopole locations, though the main text only reports the results for the radial component of SH-L19. Table S2 displays the results for the remaining SH-L19 results, Table S3 displays the results for SH-14, and Table S4 displays the results for MAVEN. We also compare these results with the reported literature values for each anomaly (Figure S2).

Anomaly	E/N/R	SNR	Inc (°)	Dec (°)	λ_p (°N)	φ_p (°E)	k	s (°)	dm (°)	dp (°)
A2	East	3.7	-54	27	55.8	70.4	11.8	24.9	34.9	24.4
	North	5.1	-50	88	28	131.2	3.7	43.9	58.4	38.9
A3	East	2.6	-30	179	-48.2	167.9	18.8	18.9	21.0	11.6
	North	4.8	-40	213	-47.8	118	8.1	29.6	35.5	21.3
A3b	East	2.8	-2	308	23	48.4	4.0	41.8	41.8	20.9
	North	2.7	22	358	52.9	353	21.1	17.9	18.9	10.0
P1	East	2.9	-20	156	-54.3	166.3	14.5	22.2	23.1	12.1
	North	3.3	-14	233	-32.6	280.1	4.1	44.4	45.4	23.2
P2	East	3.5	-56	221	-57.4	108.8	5.1	36.8	52.8	37.9
	North	6.3	-30	302	15.2	90.9	14.0	22.6	25.1	13.9
CR	East	4.2	-30	110	-10	7.8	14.6	21.4	23.8	13.2
	North	3.8	-72	18	57.7	55	11.1	24.7	43.4	38.1
AM	East	5.6	-64	316	34.9	72.2	7.6	29.9	47.6	37.8
	North	4.4	-64	188	-38.5	42.9	7.8	29.5	46.9	37.3
TS	East	2.5	-22	44	44.2	262.3	6.6	32.5	34.3	18.0
	North	3.6	-40	34	58.2	270.4	14.5	21.5	25.8	15.5
MT	East	4.9	-8	72	17.8	75.9	7.4	31.2	31.4	15.8
	North	3.2	-40	55	32.4	98.3	6.3	32.9	39.5	23.7
BP	East	4.1	-18	250	-11.7	188.5	12.8	22.9	23.7	12.3
	North	3.4	-18	266	1.9	198	65.1	10.1	10.4	5.4

Table C2. Compilation of results for the East and North components of SH-L19. Anomaly latitude, longitude, observational extent (r_o) and model dipole extent (r_d) are the

same as in Table 3.1 and not repeated here. Listed here are the component used (east or north), the SNR, inclination (Inc) and declination (Dec) resulting from Parker's method, south paleopole latitude (λ_p) and longitude (φ_p), the precision parameter (*k),* and angular standard deviation (*s*) from the 20 Monte Carlo simulations to estimate uncertainty, and the paleopole ellipse semi-axes, *dm* and *dp,* derived from *s*. All are in units of degrees, except for SNR and *k* which are unitless. CR = Claritas Rupes, AM = Amazonis Mensa, TS = Terra Sirenum, MT = Margaritifer Terra, and BP = Bosphoros Planum.

Anomaly	Component	SNR	Inc (°)	Dec (°)	λ_p (°N)	φ_p (°E)
A2	East	6.9	-52	16.5	56.4	54.2
	North	6.4	-52	90	29	133.8
	Radial	16.3	-84	307.1	69.5	236.8
A3	East	4.5	-32	197.5	-47.5	140.9
	North	6.9	-48	191.9	-60.3	144.7
	Radial	6.9	-36	209.5	-46.2	123.8
A3b	East	2.8	8	292.4	18.1	64.9
	North	2.5	34	357.3	60.4	354.3
	Radial	4.0	14	296.5	23	63.6
P1	East	4.3	-18	156	-55.2	165.3
	North	4.7	-20	225.9	-37.4	273
	Radial	8.3	-64	156.9	-24.5	192.4
P2	East	3.3	-42	247.1	-31.6	114.8
	North	6.1	-52	284.7	-7.6	88.9
	Radial	5.1	-30	268	-10.7	111.4
CR	East	4.6	-34	118.2	-14.8	14.2
	North	4.7	-70	333.3	57	103.3
	Radial	6.6	-54	69.7	30.8	9.9
AM	East	4.3	-62	291.9	19.7	82.1
	North	4.0	-42	238	-26.3	95.8
	Radial	8.3	-54	240	-20.8	85.8
TS	East	2.4	-24	41.3	47.3	261.8
	North	3.7	-40	43.1	50.7	276.4
	Radial	6.0	-76	60	42.1	338
MT	East	4.8	-2	75.2	14.8	72.77
	North	3.1	-34	63.2	25.7	92.1
	Radial	6.3	-24	56.3	33.1	86.3
BP	East	5.1	-18	247.2	-13.6	187
	North	3.4	-20	264.6	0.9	196.2
	Radial	11.8	-28	253.3	-5.6	186.2

Table C3. Compilation of results for the individual components of SH-M14. Anomaly latitude, longitude, observational extent (r_o) and model dipole extent (r_d) are the same as

in Table 3.1 and not repeated here. Listed here are the component used (east or north), the SNR, inclination (Inc) and declination (Dec) resulting from Parker's method, south paleopole latitude (λ_p) and longitude (φ_p). All are in units of degrees, except for SNR which is unitless. CR = Claritas Rupes, AM = Amazonis Mensa, TS = Terra Sirenum, MT = Margaritifer Terra, and BP = Bosphoros Planum. Note that *k*, s, *dm*, and *dp* are not listed here as no uncertainty estimation analysis was performed on the SH-M14 dataset.

Anomaly	Component	Inc (°)	Dec (°)	λ_p (°N)	φ_p (°E)
A2	East	-14	176.5	-18.5	204.8
	North	-54	92.9	29.6	137.4
	Radial	-82	343.6	79	232.4
A3	East	-10	175.4	-37.4	171.8
	North	-18	91.2	-8.2	259.9
	Radial	-30	186.6	-48.2	156.5
A3b	East	16	320.9	38.3	41.6
	North	10	346.2	45.4	8.8
	Radial	16	306.7	30.2	55.5
P1	East	-12	149.8	-52.6	154.6
	North	-8	232.7	-34	283.3
	Radial	-48	140.9	-30.9	170
P2	East	-28	163.3	-64.6	253.9
	North	-6	295.8	19	105.5
	Radial	-42	283.7	-3.2	96.2
CR	East	-26	109	-10.2	-95.1
	North	-68	165	-10.9	64.5
	Radial	-36	88.6	9.9	0.9
AM	East	-68	339	41.2	53.5
	North	-52	134.1	-32.2	350.3
	Radial	-60	207.3	-37.6	62.2
TS	East	-12	38.3	45.6	251.8
	North	-38	49	45.2	277.8
	Radial	-62	34.1	61.3	311.4
MT	East	-8	72.2	17.8	75.9
	North	-26	91	-1	85.5
	Radial	-30	57.8	31.1	90.2
BP	East	-28	189	-41.7	129.2
	North	-24	231.3	-23.2	173.5
	Radial	-38	239	-12	172.4

Table C4. Compilation of results for the individual components of MAVEN. Anomaly latitude, longitude, observational extent (r_o) and model dipole extent (r_d) are the same as

in Table 3.1 and not repeated here. Listed here are the component used (east or north), inclination (Inc) and declination (Dec) resulting from Parker's method, south paleopole latitude (λ_p) and longitude (φ_p). All are in units of degrees, except for SNR which is unitless. CR = Claritas Rupes, AM = Amazonis Mensa, TS = Terra Sirenum, MT = Margaritifer Terra, and BP = Bosphoros Planum. Note that SNR is not listed as it cannot be computed for MAVEN data, and *k*, s, *dm*, and *dp* are not listed here as no uncertainty estimation analysis was performed on the MAVEN dataset.

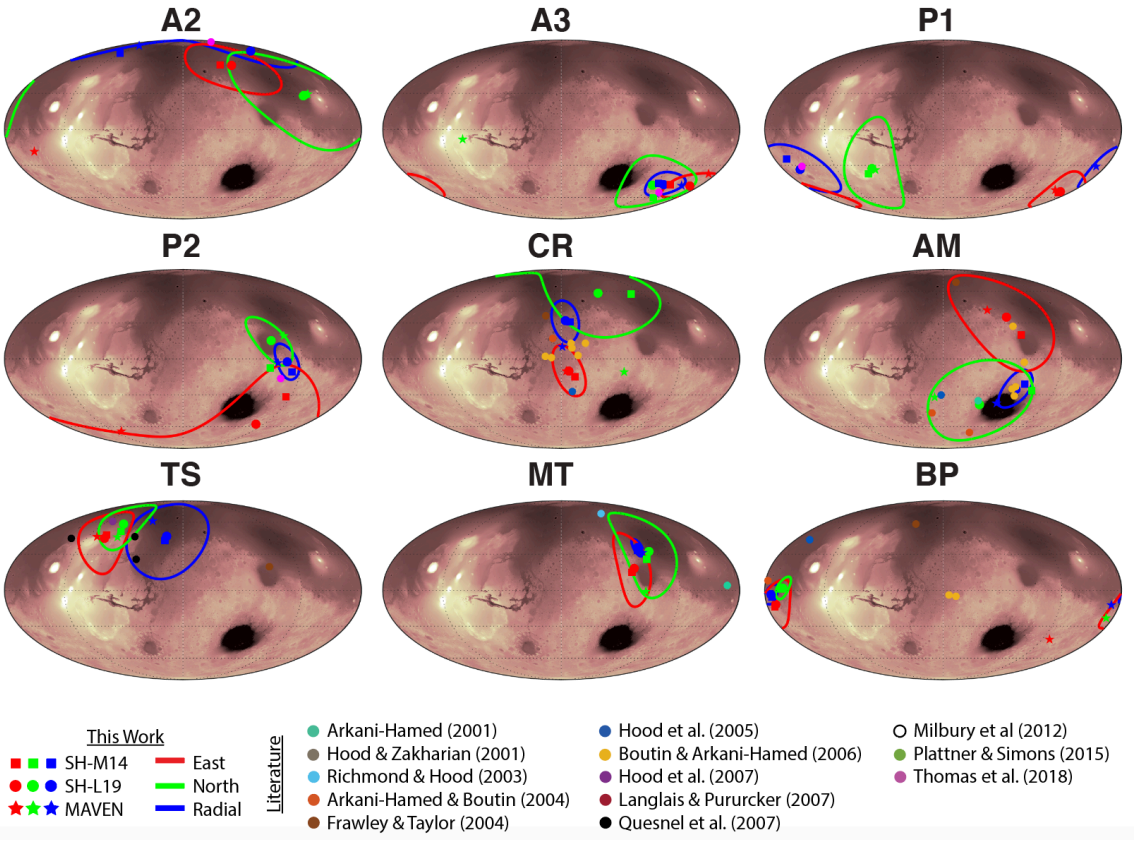

Figure C2. Paleopole locations for each component of the M14 (square), L19 (circle), and MAVEN (star) datasets compared with literature values (smaller circles), plotted over MOLA topography data (Smith et al., 2001). Mollweide projection is used, centered on 0°N 0°E.

Bibliography

Acuna, M.H., Connerney, J.E.P., Ness, N.F., Lin, R.P., Mitchell, D., Carlson, C.W., McFadden, J., Anderson, K.A., Reme, H., Mazelle, C., Vignes, D., Wasilewski, P., Cloutier, P., 1999. Global Distribution of Crustal Magnetization Discovered by the Mars Global Surveyor MAG/ER Experiment. Science 284, 790–793. https://doi.org/10.1126/science.284.5415.790

Araki, H., Tazawa, S., Noda, H., Ishihara, Y., Goossens, S., Sasaki, S., Kawano, N., Kamiya, I., Otake, H., Oberst, J., Shum, C., 2009. Lunar Global Shape and Polar Topography Derived from Kaguya-LALT Laser Altimetry. Science 323, 897–900. https://doi.org/10.1126/science.1164146

Arkani-Hamed, J., 2001. Paleomagnetic pole positions and pole reversals of Mars. Geophysical Research Letters 28, 3409–3412. https://doi.org/10.1029/2001GL012928

Arkani-Hamed, J., 1998. The lunar mascons revisited. Journal of Geophysical Research: Planets 103, 3709–3739. https://doi.org/10.1029/97JE02815

Arkani-Hamed, J., Boutin, D., 2014. Analysis of isolated magnetic anomalies and magnetic signatures of impact craters: Evidence for a core dynamo in the early history of the Moon. Icarus 237, 262–277. https://doi.org/10.1016/j.icarus.2014.04.046

Arkani-Hamed, J., Boutin, D., 2004. Paleomagnetic poles of Mars: Revisited. Journal of Geophysical Research: Planets 109. https://doi.org/10.1029/2003JE002229

Audet, P., 2014. Toward mapping the effective elastic thickness of planetary lithospheres from a spherical wavelet analysis of gravity and topography. Physics of the Earth and Planetary Interiors 226, 48–82. https://doi.org/10.1016/j.pepi.2013.09.011

Baek, S.-M., Kim, K.-H., Garrick-Bethell, I., Jin, H., 2019. Magnetic Anomalies Within the Crisium Basin: Magnetization Directions, Source Depths, and Ages. Journal of Geophysical Research: Planets. https://doi.org/10.1029/2018JE005678

Baek, S.-M., Kim, K.-H., Garrick-Bethell, I., Jin, H., Lee, H.-J., Lee, J.-K., 2017. Detailed study of the Mare Crisium northern magnetic anomaly: CRISIUM NORTHERN MAGNETIC ANOMALY. Journal of Geophysical Research: Planets 122, 411–430. https://doi.org/10.1002/2016JE005138

Bendat, J.S., Piersol, A.G., 2011. Random data: analysis and measurement procedures. John Wiley & Sons.

Bouley, S., Baratoux, D., Matsuyama, I., Forget, F., Séjourné, A., Turbet, M., Costard, F., 2016. Late Tharsis formation and implications for early Mars. Nature 531, 344–347. https://doi.org/10.1038/nature17171

Boutin, D., Arkani-Hamed, J., 2006. Pole wandering of Mars: Evidence from paleomagnetic poles. Icarus 181, 13–25. https://doi.org/10.1016/j.icarus.2005.10.025

Butler, R.F., 1992. Paleomagnetism: Magnetic domains to geologic terranes. Blackwell Scientific Publications, Boston, MA.

Chan, N.-H., Perron, J.T., Mitrovica, J.X., Gomez, N.A., 2018. New Evidence of an Ancient Martian Ocean From the Global Distribution of Valley Networks. Journal of Geophysical Research: Planets 123, 2138–2150. https://doi.org/10.1029/2018JE005536

Connerney, J.E.P., Espley, J., Lawton, P., Murphy, S., Odom, J., Oliversen, R., Sheppard, D., 2015. The MAVEN Magnetic Field Investigation. Space Sci Rev 195, 257–291. https://doi.org/10.1007/s11214-015-0169-4

Crosby, A., McKenzie, D., 2005. Measurements of the elastic thickness under ancient lunar terrain. Icarus 173, 100–107. https://doi.org/10.1016/j.icarus.2004.07.017

Deca, J., Hemingway, D.J., Divin, A., Lue, C., Poppe, A.R., Garrick-Bethell, I., Lembège, B., Horányi, M., 2020. Simulating the Reiner Gamma Swirl: The Long-Term Effect of Solar Wind Standoff. Journal of Geophysical Research: Planets 125, e2019JE006219. https://doi.org/10.1029/2019JE006219

Ding, M., Lin, J., Gu, C., Huang, Q., Zuber, M.T., 2019. Variations in Martian Lithospheric Strength Based on Gravity/Topography Analysis. Journal of Geophysical Research: Planets 124, 3095–3118. https://doi.org/10.1029/2019JE005937

Elkins-Tanton, L.T., Parmentier, E.M., Hess, P.C., 2003. Magma ocean fractional crystallization and cumulate overturn in terrestrial planets: Implications for Mars. Meteoritics & Planetary Science 38, 1753–1771. https://doi.org/10.1111/j.1945-5100.2003.tb00013.x

Elkins-Tanton, L.T., Zaranek, S.E., Parmentier, E.M., Hess, P.C., 2005. Early magnetic field and magmatic activity on Mars from magma ocean cumulate overturn. Earth and Planetary Science Letters 236, 1–12. https://doi.org/10.1016/j.epsl.2005.04.044

Foreman-Mackey, D., Hogg, D.W., Lang, D., Goodman, J., 2013. emcee: The MCMC Hammer. Publications of the Astronomical Society of the Pacific 125, 306–312. https://doi.org/10.1086/670067

Frawley, J.J., Taylor, P.T., 2004. Paleo-pole positions from martian magnetic anomaly data. Icarus 172, 316–327. https://doi.org/10.1016/j.icarus.2004.07.025

Garrick-Bethell, I., Kelley, M.R., 2019. Reiner Gamma: A Magnetized Elliptical Disk on the Moon. Geophysical Research Letters 46, 5065–5074. https://doi.org/10.1029/2019GL082427

Garrick-Bethell, I., Perera, V., Nimmo, F., Zuber, M.T., 2014. The tidal–rotational shape of the Moon and evidence for polar wander. Nature 512, 181–184. https://doi.org/10.1038/nature13639

Garrick-Bethell, I., Poppe, A.R., Fatemi, S., 2019. The Lunar Paleo-Magnetosphere: Implications for the Accumulation of Polar Volatile Deposits. Geophysical Research Letters 46, 5778–5787. https://doi.org/10.1029/2019GL082548

Gerhards, C., 2016. On the unique reconstruction of induced spherical magnetizations. Inverse Problems 32, 015002. https://doi.org/10.1088/0266-5611/32/1/015002

Glenn, D.R., Fu, R.R., Kehayias, P., Le Sage, D., Lima, E.A., Weiss, B.P., Walsworth, R.L., 2017. Micrometer-scale magnetic imaging of geological samples using a quantum diamond microscope. Geochem. Geophys. Geosyst. 18, 3254–3267. https://doi.org/10.1002/2017GC006946

Goossens, S., Matsumoto, K., Liu, Q., Kikuchi, F., Sato, K., Hanada, H., Ishihara, Y., Noda, H., Kawano, N., Namiki, N., Iwata, T., Lemoine, F.G., Rowlands, D.D., Harada, Y., Chen, M., 2011. Lunar gravity field determination using SELENE same-beam differential VLBI tracking data. J Geod 85, 205–228. https://doi.org/10.1007/s00190-010-0430-2

Halls, H.C., Lovette, A., Hamilton, M., Söderlund, U., 2015. A paleomagnetic and U–Pb geochronology study of the western end of the Grenville dyke swarm: Rapid changes in paleomagnetic field direction at ca. 585Ma related to polarity reversals? Precambrian Research 257, 137–166. https://doi.org/10.1016/j.precamres.2014.11.029

Head, J.W., Fassett, C.I., Kadish, S.J., Smith, D.E., Zuber, M.T., Neumann, G.A., Mazarico, E., 2010. Global Distribution of Large Lunar Craters: Implications for Resurfacing and Impactor Populations. Science 329, 1504–1507. https://doi.org/10.1126/science.1195050

Hemingway, D., Garrick-Bethell, I., 2012. Magnetic field direction and lunar swirl morphology: Insights from Airy and Reiner Gamma: MAGNETIC FIELD DIRECTION AT LUNAR SWIRLS. Journal of Geophysical Research: Planets 117. https://doi.org/10.1029/2012JE004165

Hemingway, D.J., Tikoo, S.M., 2018. Lunar Swirl Morphology Constrains the Geometry, Magnetization, and Origins of Lunar Magnetic Anomalies: LUNAR MAGNETIC SOURCES CONSTRAINED BY SWIRLS. J. Geophys. Res. Planets 123, 2223–2241. https://doi.org/10.1029/2018JE005604

Hood, L., Richmond, N., Harrison, K., Lillis, R., 2007. East–west trending magnetic anomalies in the Southern Hemisphere of Mars: Modeling analysis and interpretation. Icarus 191, 113–131. https://doi.org/10.1016/j.icarus.2007.04.025

Hood, L.L., 1981. Sources of lunar magnetic anomalies and their bulk directions of magnetization: Additional evidence from Apollo orbital data. LPSC 37.

Hood, L.L., Harrison, K.P., Langlais, B., Lillis, R.J., Poulet, F., Williams, D.A., 2010. Magnetic anomalies near Apollinaris Patera and the Medusae Fossae Formation in Lucus Planum, Mars. Icarus 208, 118–131. https://doi.org/10.1016/j.icarus.2010.01.009

Hood, L.L., Young, C.N., Richmond, N.C., Harrison, K.P., 2005. Modeling of major martian magnetic anomalies: Further evidence for polar reorientations during the Noachian. Icarus 177, 144–173. https://doi.org/10.1016/j.icarus.2005.02.008

Hood, L.L., Zakharian, A., 2001. Mapping and modeling of magnetic anomalies in the northern polar region of Mars. Journal of Geophysical Research: Planets 106, 14601–14619. https://doi.org/10.1029/2000JE001304

Hood, L.L., Zakharian, A., Halekas, J., Mitchell, D.L., Lin, R.P., Acuña, M.H., Binder, A.B., 2001. Initial mapping and interpretation of lunar crustal magnetic anomalies using Lunar Prospector magnetometer data. Journal of Geophysical Research: Planets 106, 27825–27839. https://doi.org/10.1029/2000JE001366

Huang, Q., Wieczorek, M.A., 2012. Density and porosity of the lunar crust from gravity and topography. Journal of Geophysical Research: Planets 117. https://doi.org/10.1029/2012JE004062

Irving, E., 1964. Paleomagnetism and its application to geological and geophysical problems. Wiley, New York.

Kamata, S., Sugita, S., Abe, Y., Ishihara, Y., Harada, Y., Morota, T., Namiki, N., Iwata, T., Hanada, H., Araki, H., Matsumoto, K., Tajika, E., Kuramoto, K., Nimmo, F.,

2015. The relative timing of Lunar Magma Ocean solidification and the Late Heavy Bombardment inferred from highly degraded impact basin structures. Icarus 250, 492–503. https://doi.org/10.1016/j.icarus.2014.12.025

Katanforoush, A., Shahshahani, M., 2003. Distributing Points on the Sphere, I. Experimental Mathematics 12, 199–209. https://doi.org/10.1080/10586458.2003.10504492

Ke, Y., Solomatov, V.S., 2006. Early transient superplumes and the origin of the Martian crustal dichotomy. Journal of Geophysical Research: Planets 111. https://doi.org/10.1029/2005JE002631

Keane, J.T., Matsuyama, I., 2014. Evidence for lunar true polar wander and a past low-eccentricity, synchronous lunar orbit. Geophysical Research Letters 41, 6610–6619. https://doi.org/10.1002/2014GL061195

Kelley, M.R., Garrick-Bethell, I., 2020. Gravity constraints on the age and formation of the Moon's Reiner Gamma magnetic anomaly. Icarus 338, 113465. https://doi.org/10.1016/j.icarus.2019.113465

Kirby, J.F., Swain, C.J., 2009. A reassessment of spectral T_e estimation in continental interiors: The case of North America. J. Geophys. Res. 114, B08401. https://doi.org/10.1029/2009JB006356

Kirschvink, J.L., 1980. The least-squares line and plane and the analysis of palaeomagnetic data. Geophys J Int 62, 699–718. https://doi.org/10.1111/j.1365-246X.1980.tb02601.x

Konopliv, A.S., Park, R.S., Yuan, D.-N., Asmar, S.W., Watkins, M.M., Williams, J.G., Fahnestock, E., Kruizinga, G., Paik, M., Strekalov, D., Harvey, N., Smith, D.E., Zuber, M.T., 2014. High-resolution lunar gravity fields from the GRAIL Primary and Extended Missions. Geophysical Research Letters 41, 1452–1458. https://doi.org/10.1002/2013GL059066

Laneuville, M., Wieczorek, M.A., Breuer, D., Tosi, N., 2013. Asymmetric thermal evolution of the Moon. Journal of Geophysical Research: Planets 118, 1435–1452. https://doi.org/10.1002/jgre.20103

Langlais, B., Purucker, M., 2007. A polar magnetic paleopole associated with Apollinaris Patera, Mars. Planetary and Space Science 55, 270–279. https://doi.org/10.1016/j.pss.2006.03.008

Langlais, B., Thébault, E., Houliez, A., Purucker, M.E., Lillis, R.J., 2019. A New Model of the Crustal Magnetic Field of Mars Using MGS and MAVEN. Journal of

Geophysical Research: Planets 124, 1542–1569. https://doi.org/10.1029/2018JE005854

Lawson, C.L., Hanson, R.J., 1974. Solving Least Squares Problems. Prentice-Hall, Englewood Cliffs, N.J.

Lee, J.-K., Maxwell, R., Jin, H., Baek, S.-M., Ghassemi, O., Kelley, M., Lee, H., Kim, K.-H., Lee, S., Garrick-Bethell, I., 2019. A small lunar swirl and its implications for the formation of the Reiner Gamma magnetic anomaly. Icarus 319, 869–884. https://doi.org/10.1016/j.icarus.2018.09.015

Lemoine, F.G., Goossens, S., Sabaka, T.J., Nicholas, J.B., Mazarico, E., Rowlands, D.D., Loomis, B.D., Chinn, D.S., Neumann, G.A., Smith, D.E., Zuber, M.T., 2014. GRGM900C: A degree 900 lunar gravity model from GRAIL primary and extended mission data. Geophysical Research Letters 41, 3382–3389. https://doi.org/10.1002/2014GL060027

Li, S., Garrick-Bethell, I., 2019. Surface Water at Lunar Magnetic Anomalies. Geophysical Research Letters 46, 14318–14327. https://doi.org/10.1029/2019GL084890

Lima, E.A., Weiss, B.P., 2016. Ultra-high sensitivity moment magnetometry of geological samples using magnetic microscopy. Geochemistry, Geophysics, Geosystems 17, 3754–3774. https://doi.org/10.1002/2016GC006487

Lin, R.P., Anderson, K.A., Hood, L.L., 1988. Lunar surface magnetic field concentrations antipodal to young large impact basins. Icarus 74, 529–541. https://doi.org/10.1016/0019-1035(88)90119-4

Maia, J.S., Wieczorek, M.A., 2022. Lithospheric Structure of Venusian Crustal Plateaus. Journal of Geophysical Research: Planets 127, e2021JE007004. https://doi.org/10.1029/2021JE007004

Matsumoto, K., Goossens, S., Ishihara, Y., Liu, Q., Kikuchi, F., Iwata, T., Namiki, N., Noda, H., Hanada, H., Kawano, N., Lemoine, F.G., Rowlands, D.D., 2010. An improved lunar gravity field model from SELENE and historical tracking data: Revealing the farside gravity features. Journal of Geophysical Research: Planets 115. https://doi.org/10.1029/2009JE003499

Matsuyama, I., Manga, M., 2010. Mars without the equilibrium rotational figure, Tharsis, and the remnant rotational figure. Journal of Geophysical Research: Planets 115. https://doi.org/10.1029/2010JE003686

Maxwell, R.E., Garrick-Bethell, I., 2020. Evidence for an Ancient Near-Equatorial Lunar Dipole From Higher Precision Inversions of Crustal Magnetization. Journal of Geophysical Research: Planets 125, e2020JE006567. https://doi.org/10.1029/2020JE006567

Maxwell, R.E., Garrick-Bethell, I., Oliveira, J.S., Wieczorek, M.A., Hemingway, D., 2017. How Well Can We Estimate the Magnetization Direction of Planetary Magnetic Anomalies? Lunar and Planetary Science Conference 2486.

McGovern, P.J., Solomon, S.C., Smith, D.E., Zuber, M.T., Simons, M., Wieczorek, M.A., Phillips, R.J., Neumann, G.A., Aharonson, O., Head, J.W., 2002. Localized gravity/topography admittance and correlation spectra on Mars: Implications for regional and global evolution. Journal of Geophysical Research: Planets 107, 19-1-19–25. https://doi.org/10.1029/2002JE001854

McKenzie, D., 2003. Estimating Te in the presence of internal loads. Journal of Geophysical Research: Solid Earth 108. https://doi.org/10.1029/2002JB001766

Meert, J.G., Voo, R.V. der, Payne, T.W., 1994. Paleomagnetism of the Catoctin volcanic province: A new Vendian-Cambrian apparent polar wander path for North America. Journal of Geophysical Research: Solid Earth 99, 4625–4641. https://doi.org/10.1029/93JB01723

Milbury, C., Schubert, G., Raymond, C.A., Smrekar, S.E., Langlais, B., 2012. The history of Mars' dynamo as revealed by modeling magnetic anomalies near Tyrrhenus Mons and Syrtis Major. Journal of Geophysical Research: Planets 117. https://doi.org/10.1029/2012JE004099

Mitchell, R.N., Kilian, T.M., Raub, T.D., Evans, D.A.D., Bleeker, W., Maloof, A.C., 2011. Sutton hotspot: Resolving Ediacaran-Cambrian Tectonics and true polar wander for Laurentia. American Journal of Science 311, 651–663. https://doi.org/10.2475/08.2011.01

Morschhauser, A., Lesur, V., Grott, M., 2014. A spherical harmonic model of the lithospheric magnetic field of Mars. Journal of Geophysical Research: Planets 119, 1162–1188. https://doi.org/10.1002/2013JE004555

Munk, W.H., Cartwright, D.E., 1966. Tidal Spectroscopy and Prediction. Phil. Trans. R. Soc. Lond. A 259, 533–581. https://doi.org/10.1098/rsta.1966.0024

Nayak, M., Hemingway, D., Garrick-Bethell, I., 2017. Magnetization in the South Pole-Aitken basin: Implications for the lunar dynamo and true polar wander. Icarus 286, 153–192. https://doi.org/10.1016/j.icarus.2016.09.038

Oliveira, J.S., Hood, L.L., Langlais, B., 2019. Constraining the Early History of Mercury and Its Core Dynamo by Studying the Crustal Magnetic Field. Journal of Geophysical Research: Planets 124, 2382–2396. https://doi.org/10.1029/2019JE005938

Oliveira, J.S., Wieczorek, M.A., 2017. Testing the axial dipole hypothesis for the Moon by modeling the direction of crustal magnetization: MODELING THE LUNAR CRUSTAL MAGNETIZATION. Journal of Geophysical Research: Planets 122, 383–399. https://doi.org/10.1002/2016JE005199

Park, R.S., Konopliv, A.S., Yuan, D.N., Asmar, S., Watkins, M.M., Williams, J., Smith, D.E., Zuber, M.T., 2015. A high-resolution spherical harmonic degree 1500 lunar gravity field from the GRAIL mission. AGU Fall Meeting Abstracts 2015 2015.

Parker, R.L., 1991. A theory of ideal bodies for seamount magnetism. Journal of Geophysical Research 96, 16101. https://doi.org/10.1029/91JB01497

Parker, R.L., Shure, L., Hildebrand, J.A., 1987. The application of inverse theory to seamount magnetism. Reviews of Geophysics 25, 17. https://doi.org/10.1029/RG025i001p00017

Perron, J.T., Mitrovica, J.X., Manga, M., Matsuyama, I., Richards, M.A., 2007. Evidence for an ancient martian ocean in the topography of deformed shorelines. Nature 447, 840–843. https://doi.org/10.1038/nature05873

Pieters, C.M., Goswami, J.N., Clark, R.N., Annadurai, M., Boardman, J., Buratti, B., Combe, J.-P., Dyar, M.D., Green, R., Head, J.W., Hibbitts, C., Hicks, M., Isaacson, P., Klima, R., Kramer, G., Kumar, S., Livo, E., Lundeen, S., Malaret, E., McCord, T., Mustard, J., Nettles, J., Petro, N., Runyon, C., Staid, M., Sunshine, J., Taylor, L.A., Tompkins, S., Varanasi, P., 2009. Character and Spatial Distribution of OH/H2O on the Surface of the Moon Seen by M3 on Chandrayaan-1. Science 326, 568–572. https://doi.org/10.1126/science.1178658

Plattner, A., Simons, F.J., 2015. High-resolution local magnetic field models for the Martian South Pole from Mars Global Surveyor data: CRUSTAL FIELD OF MARTIAN SOUTH POLE. J. Geophys. Res. Planets 120, 1543–1566. https://doi.org/10.1002/2015JE004869

Poppe, A.R., Fatemi, S., Garrick-Bethell, I., Hemingway, D., Holmström, M., 2016. Solar wind interaction with the Reiner Gamma crustal magnetic anomaly: Connecting source magnetization to surface weathering. Icarus 266, 261–266. https://doi.org/10.1016/j.icarus.2015.11.005

Purucker, M.E., Nicholas, J.B., 2010. Global spherical harmonic models of the internal magnetic field of the Moon based on sequential and coestimation approaches. Journal of Geophysical Research 115. https://doi.org/10.1029/2010JE003650

Quesnel, Y., Langlais, B., Sotin, C., 2007. Local inversion of magnetic anomalies: Implication for Mars' crustal evolution. Planetary and Space Science 55, 258–269. https://doi.org/10.1016/j.pss.2006.02.004

Ravat, D., Purucker, M.E., Olsen, N., 2020. Lunar Magnetic Field Models From Lunar Prospector and SELENE/Kaguya Along-Track Magnetic Field Gradients. Journal of Geophysical Research: Planets 125, e2019JE006187. https://doi.org/10.1029/2019JE006187

Richmond, N.C., Hood, L.L., 2003. Paleomagnetic pole positions of Mars. Lunar and Planetary Science Conference 34.

Roberts, J.H., Zhong, S., 2006. Degree-1 convection in the Martian mantle and the origin of the hemispheric dichotomy. Journal of Geophysical Research: Planets 111. https://doi.org/10.1029/2005JE002668

Runcorn, S.K., 1983. Lunar magnetism, polar displacements and primeval satellites in the Earth–Moon system. Nature 304, 589–596. https://doi.org/10.1038/304589a0

Satya Kumar, A.V., Rajasekhar, R.P., Tiwari, V.M., 2018. Gravity anomalies and crustal structure of the Lunar far side highlands. Planetary and Space Science 163, 106–113. https://doi.org/10.1016/j.pss.2018.04.009

Siegler, M.A., Miller, R.S., Keane, J.T., Laneuville, M., Paige, D.A., Matsuyama, I., Lawrence, D.J., Crotts, A., Poston, M.J., 2016. Lunar true polar wander inferred from polar hydrogen. Nature 531, 480–484. https://doi.org/10.1038/nature17166

Smith, D.E., Zuber, M.T., Frey, H.V., Garvin, J.B., Head, J.W., Muhleman, D.O., Pettengill, G.H., Phillips, R.J., Solomon, S.C., Zwally, H.J., Banerdt, W.B., Duxbury, T.C., Golombek, M.P., Lemoine, F.G., Neumann, G.A., Rowlands, D.D., Aharonson, O., Ford, P.G., Ivanov, A.B., Johnson, C.L., McGovern, P.J., Abshire, J.B., Afzal, R.S., Sun, X., 2001. Mars Orbiter Laser Altimeter: Experiment summary after the first year of global mapping of Mars. Journal of Geophysical Research: Planets 106, 23689–23722. https://doi.org/10.1029/2000JE001364

Smith, D.E., Zuber, M.T., Jackson, G.B., Cavanaugh, J.F., Neumann, G.A., Riris, H., Sun, X., Zellar, R.S., Coltharp, C., Connelly, J., Katz, R.B., Kleyner, I., Liiva, P., Matuszeski, A., Mazarico, E.M., McGarry, J.F., Novo-Gradac, A.-M., Ott, M.N., Peters, C., Ramos-Izquierdo, L.A., Ramsey, L., Rowlands, D.D., Schmidt, S., Scott, V.S., Shaw, G.B., Smith, J.C., Swinski, J.-P., Torrence, M.H., Unger, G., Yu, A.W.,

Zagwodzki, T.W., 2010. The Lunar Orbiter Laser Altimeter Investigation on the Lunar Reconnaissance Orbiter Mission. Space Sci Rev 150, 209–241. https://doi.org/10.1007/s11214-009-9512-y

Sori, M.M., James, P.B., Johnson, B.C., Soderblom, J.M., Solomon, S.C., Wieczorek, M.A., Zuber, M.T., 2018. Isostatic Compensation of the Lunar Highlands. Journal of Geophysical Research: Planets 123, 646–665. https://doi.org/10.1002/2017JE005362

Sprenke, K., Baker, L.L., 2000. Magnetization, Paleomagnetic Poles, and Polar Wander on Mars. Icarus 147, 26–34. https://doi.org/10.1006/icar.2000.6439

Stacey, F.D., 1985. Geomagnetism: The Earth's Magnetic Field. Academic Press, Orlando, FL.

Stanley, S., Elkins-Tanton, L., Zuber, M.T., Parmentier, E.M., 2008. Mars' Paleomagnetic Field as the Result of a Single-Hemisphere Dynamo. Science 321, 1822–1825. https://doi.org/10.1126/science.1161119

Sugano, T., Heki, K., 2004. Isostasy of the Moon from high-resolution gravity and topography data: Implication for its thermal history. Geophysical Research Letters 31. https://doi.org/10.1029/2004GL022059

Symons, D.T.A., Chiasson, A.D., 1991. Paleomagnetism of the Callander Complex and the Cambrian apparent polar wander path for North America. Can. J. Earth Sci. 28, 355–363. https://doi.org/10.1139/e91-032

Takahashi, F., Tsunakawa, H., 2009. Thermal core-mantle coupling in an early lunar dynamo: Implications for a global magnetic field and magnetosphere of the early Moon. Geophysical Research Letters 36, L24202. https://doi.org/10.1029/2009GL041221

Takahashi, F., Tsunakawa, H., Shimizu, H., Shibuya, H., Matsushima, M., 2014. Reorientation of the early lunar pole. Nature Geosci 7, 409–412. https://doi.org/10.1038/ngeo2150

Thomas, P., Grott, M., Morschhauser, A., Vervelidou, F., 2018. Paleopole Reconstruction of Martian Magnetic Field Anomalies. Journal of Geophysical Research: Planets 123, 1140–1155. https://doi.org/10.1002/2017JE005511

Tsunakawa, H., Shibuya, H., Takahashi, F., Shimizu, H., Matsushima, M., Matsuoka, A., Nakazawa, S., Otake, H., Iijima, Y., 2010. Lunar Magnetic Field Observation and Initial Global Mapping of Lunar Magnetic Anomalies by MAP-LMAG Onboard SELENE (Kaguya). Space Sci Rev 154, 219–251. https://doi.org/10.1007/s11214-010-9652-0

Tsunakawa, H., Takahashi, F., Shimizu, H., Shibuya, H., Matsushima, M., 2015. Surface vector mapping of magnetic anomalies over the Moon using Kaguya and Lunar Prospector observations: SVM OF MAGNETIC ANOMALIES OVER THE MOON. Journal of Geophysical Research: Planets 120, 1160–1185. https://doi.org/10.1002/2014JE004785

Vervelidou, F., Lesur, V., Morschhauser, A., Grott, M., Thomas, P., 2017. On the accuracy of palaeopole estimations from magnetic field measurements. Geophysical Journal International 211, 1669–1678. https://doi.org/10.1093/gji/ggx400

Wakita, S., Johnson, B.C., Garrick-Bethell, I., Kelley, M.R., Maxwell, R.E., Davison, T.M., 2021. Impactor material records the ancient lunar magnetic field in antipodal anomalies. Nat Commun 12, 6543. https://doi.org/10.1038/s41467-021-26860-1

Watters, W.A., Zuber, M.T., Hager, B.H., 2009. Thermal perturbations caused by large impacts and consequences for mantle convection. Journal of Geophysical Research: Planets 114. https://doi.org/10.1029/2007JE002964

Watts, A., Zhong, S.J., Hunter, J., 2012. The Behavior of the Lithosphere on Seismic to Geologic Timescales. Annual Review of Earth and Planetary Sciences. https://doi.org/10.1146/annurev-earth-042711-105457

Wieczorek, M.A., 2006. On estimating the elastic thickness from gravity and topography data: Spherical multitaper methods and partially correlated surface and subsurface loads. AGU Fall Meeting Abstracts 2006 T54B-03.

Wieczorek, M.A., Meschede, M., 2018. SHTools: Tools for Working with Spherical Harmonics. Geochemistry, Geophysics, Geosystems 19, 2574–2592. https://doi.org/10.1029/2018GC007529

Wieczorek, M.A., Neumann, G.A., Nimmo, F., Kiefer, W.S., Taylor, G.J., Melosh, H.J., Phillips, R.J., Solomon, S.C., Andrews-Hanna, J.C., Asmar, S.W., Konopliv, A.S., Lemoine, F.G., Smith, D.E., Watkins, M.M., Williams, J.G., Zuber, M.T., 2013. The Crust of the Moon as Seen by GRAIL. Science 339, 671–675. https://doi.org/10.1126/science.1231530

Wieczorek, M.A., Phillips, R.J., 1998. Potential anomalies on a sphere: Applications to the thickness of the lunar crust. J. Geophys. Res. 103, 1715–1724. https://doi.org/10.1029/97JE03136

Wieczorek, M.A., Simons, F.J., 2005. Localized spectral analysis on the sphere. Geophysical Journal International 162, 655–675. https://doi.org/10.1111/j.1365-246X.2005.02687.x

Wieczorek, M.A., Weiss, B.P., Stewart, S.T., 2012. An Impactor Origin for Lunar Magnetic Anomalies. Science 335, 1212–1215. https://doi.org/10.1126/science.1214773

Wilhelms, D.E., Squyres, S.W., 1984. The martian hemispheric dichotomy may be due to a giant impact. Nature 309, 138–140. https://doi.org/10.1038/309138a0

Yan, J., Goossens, S., Matsumoto, K., Ping, J., Harada, Y., Iwata, T., Namiki, N., Li, F., Tang, G., Cao, J., Hanada, H., Kawano, N., 2012. CEGM02: An improved lunar gravity model using Chang'E-1 orbital tracking data. Planetary and Space Science 62, 1–9. https://doi.org/10.1016/j.pss.2011.11.010

Zhong, S., Zuber, M.T., 2001. Degree-1 mantle convection and the crustal dichotomy on Mars. Earth and Planetary Science Letters 189, 75–84. https://doi.org/10.1016/S0012-821X(01)00345-4

Zhong, Z., Li, F., Yan, J., Yan, P., Dohm, J.M., 2014. Lunar geophysical parameters inversion based on gravity/topography admittance and particle swarm optimization. Advances in Space Research 54, 770–779. https://doi.org/10.1016/j.asr.2014.04.009

Zhong, Z., Yan, J.-G., Alexis, J., Rodriguez, P., 2019a. Ancient subsurface structure beneath crater Clavius: constraint by recent high-precision gravity and topography data. Res. Astron. Astrophys. 19, 009. https://doi.org/10.1088/1674-4527/19/1/9

Zhong, Z., Yan, J.-G., Zhang, T., Xiao, Z.-Y., Palmero Rodriguez, J.A., 2019b. Estimation of the elastic thickness over ancient Mare Moscoviense. Res. Astron. Astrophys. 19, 184. https://doi.org/10.1088/1674-4527/19/12/184

Zuber, M.T., Smith, D.E., Watkins, M.M., Asmar, S.W., Konopliv, A.S., Lemoine, F.G., Melosh, H.J., Neumann, G.A., Phillips, R.J., Solomon, S.C., Wieczorek, M.A., Williams, J.G., Goossens, S.J., Kruizinga, G., Mazarico, E., Park, R.S., Yuan, D.-N., 2013. Gravity Field of the Moon from the Gravity Recovery and Interior Laboratory (GRAIL) Mission. Science 339, 668–671. https://doi.org/10.1126/science.1231507